

Activity and Feeding of Nearby Low Luminosity Active Galactic Nuclei

INAUGURAL-DISSERTATION

zur

Erlangung des Doktorgrades
der Mathematisch-Naturwissenschaftlichen Fakultät
der Universität zu Köln



vorgelegt von

Marcus Bremer

aus Köln

Köln 2014

Berichterstatter:

Prof. Dr. Andreas Eckart

Prof. Dr. Lucas Labadie

Tag der letzten mündlichen Prüfung: 2. Juni 2014

Für meine Mutter.

Abstract

Throughout the last decades a number of correlations between the properties of the supermassive black holes (SMBH) in the center of galaxies and their hosting galaxies have been found. This suggests that these components influence each other in their evolution. Especially the SMBHs, which accrete matter and reveal themselves as Active Galactic Nuclei (AGN), are suspected to have a major impact on the host galaxy. The so-called ‘positive feedback’ of an AGN triggers star formation locally by outflows and jets. The ‘negative feedback’ manifests itself in the galaxy-wide quenching of star formation e.g. by the accretion of almost all the galaxy’s gas onto the SMBH. The ‘feeding’ of the SMBH is also considered to be responsible for the degree of activity of the nucleus. The transport of matter from large distances to the direct vicinity of the nucleus, where the SMBH can accrete it on its own, requires the removal of almost all the matter’s angular momentum ($\sim 99.9\%$). How is the energy taken away from the mass? On large scales (kpc-scale) bars, spirals and other asymmetries in density are invoked, leading to the dissipation of energy and forcing the gas to lower its orbit. At the order of 100 pc nested bars and nuclear spirals take over. Eventually, at ~ 10 pc, viscous processes are suspected to bridge the final gap to the SMBH. However, these mechanisms are poorly understood, particularly on very small scales. To improve the understanding of different feeding mechanisms more observations are necessary. The Nuclei-of-Galaxies (NuGA) survey targets nearby low-luminosity galaxies using ^{12}CO to pursue the topic of AGN feeding. In this thesis, complementary optical integral field spectroscopic (IFS) data for three NuGA galaxies (NGC 5850, NGC 3626 and NGC 3627) is analysed.

Though not selected for this property, they all show signs of interaction with other galaxies. Interactions provide a natural way to perturb the regular

motion of gas in galaxies in such a way that they create mechanisms capable of transporting gas to the center. Indeed two out of three galaxies I present here have at least one bar. The data focuses on the circumnuclear area, showing the diverse kinematics of the gas. NGC 5850 shows a smaller bar surrounded by a ring and nested in the large scale bar. Deviations from circular motion can be found also found in NGC 3626. NGC 3627 displays signs of oval gas orbits combined with the influence of a nuclear bar and shocks.

Additionally to the feeding topic, the special role of low-ionisation nuclear emission regions (LINERs) and their role in the AGN paradigm is studied exemplary with the observed galaxies. LINERs are often considered to be low-luminosity AGNs and have a characteristic spectrum. In this thesis I point out that other physical mechanisms exist which can produce a similar spectrum. Not every nucleus classed as a LINER is an AGN. With the here used observations, I emphasise the importance of carefully disentangling the dominant ionisation mechanisms and show how helpful spatially resolved spectroscopy (i.e. IFS) is. Indeed, at least in NGC 5850, but possibly also in NGC 3626, the influence of an AGN is likely to be negligible, although they are both considered as LINERs. There is a chance that these two galaxies are not active at all.

Zusammenfassung

Im Laufe der letzten Jahrzehnte wurde eine Anzahl Korrelationen gefunden, die die Eigenschaften supermassiver schwarzer Löcher (SMBH) in den Zentren von Galaxien in Beziehung zu den sie beherbergenden Galaxien setzen. Dies impliziert eine gegenseitige Beeinflussung ihrer jeweiligen Evolution. Insbesondere die SMBHs, die Materie akkretieren und sich als aktive Galaxienkerne (AGN) zeigen, werden verdächtigt grossen Einfluss auf ihre Galaxie zu nehmen.

Die sogenannte ‘positive Rückkopplung’ (‘positives Feedback’) von AGN initiiert lokale Sternentstehung durch Materieausflüsse und Jets. Die ‘negative Rückkopplung’ (‘negatives Feedback’) zeigt sich in Form einer galaxieweiten Beendigung der Sternentstehungsaktivität, beispielsweise durch die Akkretion beinahe allen Gases auf das SMBH. Das ‘Füttern’ (‘Feeding’) von SMBH wird auch als Ursache für den Grad der Aktivität des Kerns ausgemacht. Der Transport von Materie aus grossen Entfernungen in die direkte Umgebung des Kerns, wo das SMBH selbstständig akkretieren kann, setzt die Neutralisierung des beinahe gesamten Drehimpulses der Materie voraus ($\sim 99.9\%$). Wie wird die Energie der Materie genommen? Auf grossen räumlichen Skalen (kpc) werden Balken, Spiralen und andere Dichteasymmetrien zur Begründung herangezogen, die zur Dissipation von Energie führen und damit das Gas in eine engere Umlaufbahn zwingen. In Grössenordnungen von 100 pc können dies verschachtelte Balken und nukleare Balken bewirken. Zuletzt, in Abständen von ~ 10 pc, werden viskose Prozesse vermutet, um die letzte Kluft zum SMBH zu überbrücken. Diese Mechanismen sind jedoch kaum verstanden, insbesondere auf kleinen Skalen. Zur Verbesserung des Verständnisses der verschiedenen Feedingprozesse sind weitere Beobachtungen notwendig. Die Studie ‘Nuclei-of-Galaxies’ (NuGA) beobachtet ^{12}CO in nahen und schwachleuchtenden Galaxien um das Thema des AGN feeding zu verfolgen. In der vorliegenden Arbeit werden ergänzend optische und räumlich aufgelöste Spektroskopiedaten für drei NuGA Galaxien (NGC 5850, NGC 3626 und NGC 3627) analysiert.

Obwohl es kein Kriterium für ihre Auswahl war, zeigen alle drei Galaxien Zeichen von Interaktion mit anderen Galaxien. Solche Wechselwirkungen stellen eine natürliches Mittel zur Störung der regelmässigen Bewegung des Gases dar, so dass Mechanismen zum Transport des Gases zum galaktischen Zentrum entstehen können. Tatsächlich haben zwei der drei hier vorgestellten Galaxien mindestens einen Balken. Die Daten konzentrieren sich auf die Kernregion und zeigen die vielfältige Kinematik

des Gases. NGC 5850 besitzt einen kleineren Balken, der von einem Ring umgeben ist und in einen grossen Balken eingebettet ist. Abweichungen von der Kreisbewegung des Gases können auch in NGC 3626 gefunden werden. NGC 3627 zeigt Zeichen für ovale Umlaufbahnen des Gases in Kombination mit dem Einfluss eines nuklearen Balkens und mit Schocks.

Zusätzlich zum Thema Feeding wird die spezielle Rolle von Galaxien mit Regionen niedrig-ionisierter nuklearer Emission (LINER), und ihre Rolle im AGN-Bild studiert. Dies wird exemplarisch an den beobachteten Galaxien durchgeführt. LINER werden häufig zu den niedrigleuchtkräftigen AGN gezählt und besitzen ein charakteristisches Spektrum. In der vorliegenden Arbeit unterstreiche ich, dass weitere Prozesse existieren, die ein ähnliches Spektrum hervorrufen können. Nicht jeder Galaxienkern, der als LINER klassifiziert wurde, ist auch ein AGN. Mit den hier verwendeten Beobachtungsdaten unterstreiche ich die Wichtigkeit der sorgfältigen Trennung der dominanten Ionisationsmechanismen und ich zeige wie hilfreich räumlich aufgelöste Spektroskopie dabei ist. In der Tat, zumindest in NGC 5850, möglicherweise auch in NGC 3626, ist der Einfluss des AGN wahrscheinlich vernachlässigbar, obwohl beide als LINER klassifiziert wurden. Es besteht sogar die Möglichkeit, dass beide Galaxien überhaupt nicht aktiv sind.

Contents

List of Figures	v
List of Tables	ix
1 Introduction and Overview	1
1.1 Active galactic nuclei	3
1.1.1 Seyfert Galaxies	5
1.1.2 Radio Galaxies	7
1.1.3 Quasars and Quasi-Stellar Objects	7
1.1.4 Blazars, BL Lac objects, and OVV's	9
1.1.5 The Unification Theory of AGN	9
1.1.6 Low Luminosity AGN - LINERs	13
1.1.6.1 Frequency of Detection	13
1.1.6.2 The Spectral Energy Distribution	14
1.1.6.3 Energy Budget Considerations	19
1.2 Spectroscopy and Physical Quantities	20
1.2.1 The Components of Spectra	20
1.2.2 Photoionisation and Recombination	22
1.2.2.1 The Hydrogen Atom	22
1.2.2.2 Cloud of Hydrogen	26
1.2.2.3 Cloud of Hydrogen and Helium	27
1.2.2.4 Metals	28
1.2.3 Collisional Excitation	29
1.2.4 Optical Emission Lines as Indicators for Physical Conditions	30
1.2.4.1 Extinction within the Nebula	31

CONTENTS

1.2.4.2	Temperature	34
1.2.4.3	Electron Density	35
1.2.5	Diagnostic Diagrams	36
2	NGC 5850	41
2.1	Introduction	41
2.2	Observations, data reduction, and line measurements	44
2.2.1	Observations and data reduction	44
2.2.2	Continuum Subtraction and Emission Line Measurements	46
2.3	Results	49
2.3.1	Morphology	49
2.3.2	Kinematics	51
2.3.3	Excitation	57
2.4	Discussion	60
2.4.1	Composite emission	60
2.4.2	HII regions	62
2.4.3	Photoionization by AGN-contribution	66
2.4.4	Outflows	68
2.4.5	Photoionization by p-AGB stars	71
2.4.6	Kinematic scenarios	74
2.5	Summary	76
3	NGC 3626	79
3.1	Introduction	79
3.2	Observations and Data Reduction	84
3.3	Results	86
3.3.1	Morphology	86
3.3.2	Kinematics	90
3.3.3	Excitation	93
3.4	Discussion	96
3.4.1	Stellar and Gas Disks	96
3.4.2	The ‘Bad-Fit’ Region	99
3.4.3	LINER-like Emission	100
3.5	Conclusions	102

4	NGC 3627	105
4.1	Introduction	105
4.2	Observations and Data Reduction	108
4.3	Results	109
4.3.1	Morphology	109
4.3.2	Emission	109
4.3.3	Kinematics	111
4.3.4	Excitation	115
4.4	Discussion	116
4.4.1	Discussion and Interpretation	116
4.4.2	Outlook	118
5	Discussion and Conclusions	119
5.1	Ionisation	119
5.2	AGN-Feeding	120
	Bibliography	123

CONTENTS

List of Figures

1.1	SED of an AGN and its components	5
1.2	HST image of the grand design spiral galaxy M81	6
1.3	Typical optical spectra of Seyfert1 and Seyfert 2 galaxies.	7
1.4	HST image of the jet feature in M87.	8
1.5	Depiction of the unified model for galaxies with AGN	9
1.6	The logarithmic total $H\alpha$ luminosity vs. the logarithmic nonthermal continuum luminosity at λ 4800 Å.	10
1.7	An HST image of the sombrero galaxy (M104) as an example for a LINER 2 galaxy.	17
1.8	Grotian diagrams.	24
1.9	Absorption cross section vs. frequency.	25
1.10	Energy level diagrams for [O III]	34
1.11	The emission line intensity ratios of [O II] λ 3730/[O II] λ 3727 and [S II] λ 6717/[S II] λ 6732 as a function of electron density.	36
1.12	Diagnostic diagram	37
2.1	VIMOS flat image.	45
2.2	SDSS spectrum of NGC 5850.	47
2.3	Spectra of selected regions and stellar continuum fits.	48
2.4	SDSS r-band and stellar continuum image of NGC 5850.	50
2.5	Emission line maps of ionised gas. Image 1 of 2.	52
2.6	Emission line maps of ionised gas. Image 2 of 2.	53
2.7	Kinematic maps of the ionised gas.	54
2.8	$H\alpha$ line of sight-velocity map.	56
2.9	Stellar kinematic maps derived by STARLIGHT.	57

LIST OF FIGURES

2.10	Logarithmic line ratio maps.	58
2.11	Logarithmic line ratios with overplotted $H\alpha$ line of sight velocity contours.	59
2.12	Line ratio maps overplotted with classification contours.	60
2.13	Several diagnostic diagrams for NGC 5850.	61
2.14	$\log([N\ II]/H\alpha)$ map with ^{12}CO contours.	66
2.15	The spectra taken from 3×3 spaxels apertures centered on the regions described in Fig. 2.10.	72
2.16	Map of the equivalent width of the $H\alpha$ emission line.	73
2.17	Logarithmic line ratio maps.	74
2.18	Differential LOSV map ($LOS_{V\text{GAS}} - LOS_{V\text{STELLAR}}$).	77
3.1	Stellar continuum fits on spectra of selected regions of NGC 3626.	87
3.2	SDSS g-band image and VIMOS stellar continuum image of NGC 3626.	88
3.3	Emission line flux maps of the ionised gas. Image 1 of 2.	89
3.4	Emission line flux maps of the ionised gas. Image 2 of 2.	90
3.5	LOSV maps of the ionised gas. Image 1 of 2.	91
3.6	LOSV maps of the ionised gas. Image 2 of 2.	92
3.7	Stellar kinematic maps.	92
3.8	LOSV dispersion maps of the ionised gas. Image 1 of 2.	94
3.9	LOSV dispersion maps of the ionised gas. Image 2 of 2.	95
3.10	Diagnostic diagrams of NGC 3626.	96
3.11	Logarithmic emission line ratio maps overplotted with classification contours.	97
3.12	Stellar LOSV dispersion with superimposed contours of $H\alpha$ emission.	98
3.13	Maps of emission line ratios	100
3.14	The electron density map with the same superimposed continuum contours as in Fig. 3.3.	101
3.15	Equivalent width of $H\alpha$ (left).	102
4.1	Stellar continuum fits to selected regions of NGC 3627.	110
4.2	SDSS i-band image and VIMOS continuum image of NGC 3627.	111
4.3	Emission line maps of ionised gas. Image 1 of 2.	112
4.4	Emission line maps of ionised gas. Image 2 of 2.	113
4.5	The LOSV dispersion σ of $H\beta$ and $O\ III$	114

LIST OF FIGURES

4.6	Stellar kinematic maps.	114
4.7	Logarithmic emission line ratio map $\log(O\text{ III } \lambda 5008/H\beta)$ with stellar continuum contours.	115

LIST OF FIGURES

List of Tables

2.1	Double Gaussian emission line-fit attempts for regions with strong line asymmetry.	55
2.2	Star-formation rates and oxygen abundances (OA) in the H II-regions of NGC 5850.	63

LIST OF TABLES

1

Introduction and Overview

This work is motivated by the question of whether and how the activity of galactic nuclei is linked to the evolution of its host galaxy. A number of relations, connecting host properties with those of the central super-massive black hole (SMBH) in the galactic nucleus, suggest their co-evolution. Several mechanisms of interaction between the SMBH and the host galaxy have been identified (e.g. [Schawinski et al., 2014](#)). It is yet not clear whether their evolutionary impact is in general sufficiently strong, although in special cases it has been observed to be enough (see review by [Heckman & Best \(2014\)](#)).

Active galactic nuclei (AGN) are the very luminous and extremely compact central area of galaxies. Their energy output and their emission line strengths cannot be explained by thermal emission only, i.e. stars. One way to examine the putative mutual influence of AGN and host galaxy is to look as close as possible to the nucleus. There, immediate interaction between the active galactic nuclei and the host galaxy are expected. The NUClei of GALaxies (NUGA) survey pursues this approach by observing ^{12}CO gas emission and its kinematics in nearby low luminosity AGN (LLAGN) in the radio domain. The survey's immediate goal is to find and analyse the mechanisms of feeding and feedback of the central SMBH. The galaxies in this sample are chosen to be nearby ($z \leq 0.0067$ for the 'classical' sample, slightly more for the extended sample which comprises sources in the southern sky) to achieve high spatial resolution, and to be of low luminosity so that the central engine does not outshine its immediate surrounding. With the use of interferometric techniques, the spatial resolution is on scales of a few parsec to some tens of parsec, allowing a very detailed analysis of the gas.

1. INTRODUCTION AND OVERVIEW

However, the caveat of selecting low-luminosity galaxies is that it is not always clear whether an AGN is really present in the host. LLAGN, and in particular their subtypes with Low Ionisation Nuclear Emission Regions (LINERs), are sometimes elusive, as we will see in Sec. 1.1.6. To become clear about the presence of an AGN and whether we observe its feeding or feedback, the determination of the dominant ionisation mechanism as well as the analysis of the ionised gas and its kinematics are the aims of this work.

To achieve these goals, I analysed the observations of a subset of the NuGA sample. The data used in this work has been observed with an optical integral field unit (IFU) and targeted three galaxies of the extended NUGA sample located in the sky of the southern hemisphere (NUGA south). The spatial resolution of the IFU ‘VIMOS’ can compete with that of the Plateau de Bure radio interferometry (PdBI), and it provides a wealth of complementary information. Most of all, with optical spectra one can observe the ionised gas, in contrast to radio observations of the NuGA survey, which target mainly molecular gas (^{12}CO). The strong and relatively hard radiation of AGN ionises the gas in its vicinity and leaves a footprint of its properties. The analysis of the stellar and the gas kinematics will provide information on the most influential factors at distances of $\gtrsim 100$ pc to the nucleus. The approach of the gas toward the center must manifest itself as a deviation from circular rotation around a gravitational center, which in turn requires perturbations of the gas that can potentially remove angular momentum. A number of nuclear instabilities have been found and proposed to be able to accomplish this, e.g. lopsidedness in the gas distribution, nuclear spirals, rings, warps, nested bars, or stochastic instabilities (e.g. [García-Burillo et al., 2000a](#); [Pringle, 1996](#); [Schinnerer et al., 2000a,b](#); [Shlosman et al., 1989](#); [Shu et al., 1990](#)). Possibly in combination with these morphological features, decoupled dynamics, like counterrotation of the gas and/or the stars, can also contribute to the inflow of matter ([de Zeeuw et al., 2002](#); [Emsellem et al., 2001](#); [Garcia-Burillo et al., 1998](#)). These nuclear asymmetries are a key element because they govern the gas kinematics in the area between the gas transport on galaxy scales (by primary bars, spirals, and tidal interactions) and the accretion on the SMBH in the immediate vicinity of the BH.

1.1 Active galactic nuclei

It is commonly believed that a super-massive black hole is located in the center of most, if not of all galaxies. The closest example is Sagittarius A* (SgrA*), the central SMBH of our own galaxy, the Milky Way. SgrA* can be continuously detected in radio and X-ray wavelengths, but it is mostly invisible in other wavelength domains. It can only be noticed by the frequent flares originating from its putative short-lived accretion disk or, as an alternative scenario, from its low-energetic and small-scale jet, or from the orbits of the close-by stars (Baganoff et al., 2001, 2002, 2003; Bélanger et al., 2006; Bremer et al., 2011; Buchholz et al., 2011; Dodds-Eden et al., 2009; Eckart et al., 2004, 2009, 2006a, 2008a, 2012a,b, 2003, 2013b, 2008b, 2006b, 2011; Eisenhauer et al., 2005; García-Marín et al., 2011a,b; Genzel et al., 2003; Ghez et al., 2004a,b; Gillessen et al., 2012; Goldwurm et al., 2003; Hornstein et al., 2007; Marrone et al., 2008; Porquet et al., 2008, 2003; Sabha et al., 2010; Valencia-S et al., 2012; Witzel et al., 2012; Yusef-Zadeh et al., 2006a, 2009, 2006b, 2007, 2008). From these orbits the mass is calculated to be $\sim 10^6 M_{\odot}$ (Eckart & Genzel, 1996; Eckart et al., 2002; Eisenhauer et al., 2005, 2003; Genzel et al., 1997, 2000; Ghez et al., 2003, 2005, 1998, 2000, 2008; Gillessen et al., 2009; Schödel et al., 2009, 2003, 2002). Combination of its mass near-infrared brightness with its compactness lead to the confirmation that SgrA* is a SMBH. The Milky Way is a rather common galaxy and there is no reason to assume that it is special concerning its nucleus. Kinematical and modelling studies of nearby quiescent galaxies observed with Hubble (Kormendy & Ho, 2013) support the idea of black holes being in the centre of other galaxies.

SgrA* is very underluminous. Its radiation output is far below the value expected from its theoretical accretion rate and consequently it is assumed to be inactive or a (LLAGN) (Contini, 2011; Eckart et al., 2013a). But what makes a galactic nucleus 'active'?

Generally, active galactic nuclei are characterised by their high luminosity, i.e. in the visible wavelength domain up to $\sim 10^{13} L_{\odot}$, and are an energetic phenomenon (Peterson, 1997). Furthermore, they show strong emission lines of allowed (e.g. H I, He I He II) and forbidden lines (e.g. [O III]). Both, the luminosity and the strong forbidden emission lines, cannot be caused by the galaxy's stellar population. However, the source

1. INTRODUCTION AND OVERVIEW

of the strong radiation still cannot be resolved, but it is commonly assumed that the accretion disk surrounding the black hole (BH) is responsible for the radiation. The matter in the disk can reach temperatures of the order of 10^6 K and higher by friction and non-thermal effects (e.g. its corona. The frequency of occurrence of AGN is increasing with cosmological distance from the solar system, which adds to the difficulties in resolving this very compact area.

Despite the mostly thermal mechanisms in the accretion disk, the spectral energy distribution (SED, see figure 1.1) of the continuum emission of AGN deviates clearly from that of a modified black body, also indicating that stars cannot be the main contributors to the radiation. However, sometimes a weakly polarised black body contribution can be found together with a strongly polarised power-law spectrum, which manifests itself as the ‘big blue bump’ in the visible-ultraviolet part of the SED (Peterson, 1997). On the other hand, there are regions in the SED with a constant α . Commonly, α is called the spectral index defined as the exponent in the relation between flux and frequency: $F_\nu \propto \nu^{-\alpha}$. Be aware that in the literature the spectral index is often defined with the opposite sign. A constant spectral index or, alternatively expressed, a pure power-law spectrum can be produced by synchrotron radiation which is emitted by relativistic electrons in a magnetic field. Furthermore, synchrotron emission has a turnover point in the spectrum, where the emitting plasma becomes optically thick because it absorbs its own radiation (called synchrotron self-absorption). The turnover is usually in the radio domain but can also be seen in the X-ray domain due to scattering effects (synchrotron self-compton). Synchrotron emission is highly polarised, in contrast to black body emission.

The SED can change significantly, depending on the kind of AGN. Not only synchrotron emission and thermal emission from the accretion disk play a role. Also the presence of dust can make the picture more complicated, especially in the infrared (IR) domain.

AGNs show rapid variability in their luminosity. The increase of the luminosity takes typically 1 hour. Thus, from simple geometric considerations one can deduce an upper limit for the physical size of the source that powers an AGN. This source has a physical extend of a few A.U., smaller than our solar system (~ 30 A.U.. Compared with the typical AGN power output, which cannot be higher than the Eddington luminosity, the central AGN is an extremely compact object. A typical quasar with a

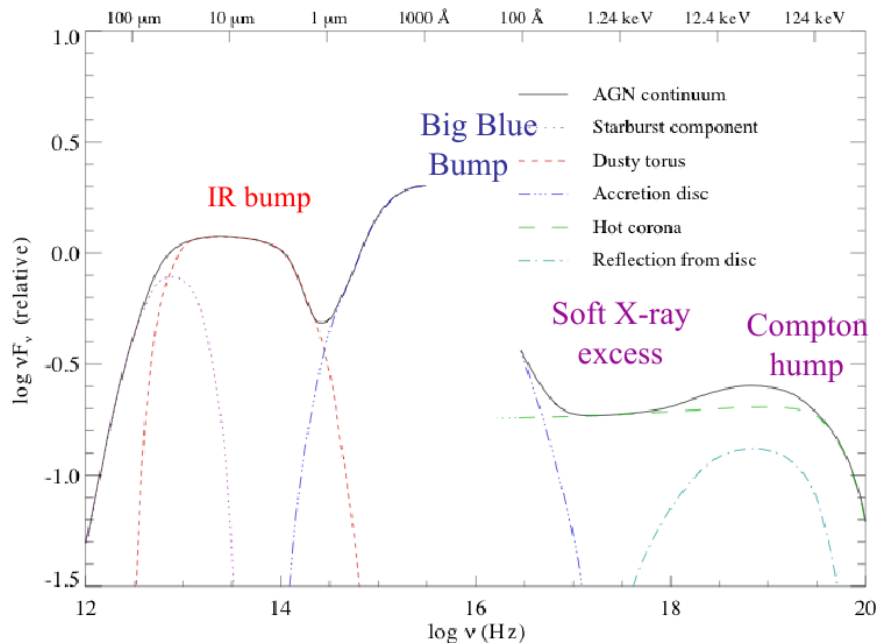


Figure 1.1: Schematic spectral energy distribution (SED) of the AGN continuum emission and their components. Taken from the lecture of Prof. Michael Crenshaw, Georgia State University, USA (http://www.chara.gsu.edu/~crenshaw/4.AGN_Components.pdf).

luminosity of $\sim 10^{46}$ ergs $^{-1}$ must have an Eddington mass of $M \gtrsim 10^8 M_{\odot}$. The fact that this amount of mass confined to such a small space is a strong support for the presence of a SMBH. Combining the upper limit for the size of AGN with an expression for the Schwarzschild radius yields masses of the same order of magnitude.

1.1.1 Seyfert Galaxies

Carl Seyfert found in 1943 a set of galaxies with those peculiar properties mentioned in Sect. 1.1 (Seyfert, 1943). Their spectra can be categorized as Seyfert 1 and Seyfert 2, named in honour of his achievements. Seyfert galaxies comprise only a small fraction of all galaxies but interestingly, they can be found mostly ($\gtrsim 90\%$) in spiral galaxies of type Sb or SBb (Carroll & Ostlie, 2006) with a point-like structure in the center. The class of Seyferts is defined to have an absolute B-band luminosity of $M_B > -21.5 + 5 \log h_0$ (Schmidt & Green, 1983), with h_0 denoting the Hubble constant in units of $100 \text{ km s}^{-1} \text{ Mpc}^{-1}$. The more modern criterion for a classification as a Seyfert galaxy requires strong emission lines originating from high-ionisation species, which will be specified in Sec. 1.2.5.

1. INTRODUCTION AND OVERVIEW



Figure 1.2: Hubble Space Telescope (HST) image of the grand design spiral galaxy M81 (also known as NGC 3031 or Bode’s Galaxy) as a beautiful example of a Seyfert 1.8 galaxy. It is located at a distance of $\approx 11.6 \times 10^6$ lightyears from earth. The image is a composite of blue, visible and infrared light. Image credits: Space Telescope Science Institute (STScI).

Seyfert 1 galaxies show emission lines that are composed of a broad base and a narrower top part (left panel of Fig. 1.3). The broad component has typically a width of $1000 - 5000 \text{ km s}^{-1}$ and can only be observed in permitted emission lines. Forbidden lines do not show a broad component (so-called narrow emission lines) and have widths of $\sim 500 \text{ km s}^{-1}$. These widths are due to Doppler broadening and therefore, they are related to the speed of the source components comprised in the spectrum. In Seyfert 2 galaxies all lines are narrow ($\sim 500 \text{ km s}^{-1}$). Both AGN classes have the so-called ‘featureless continuum’ in common. These are parts of the spectrum which do not show any emission lines and are dominated by the radiation of the central source. This continuum radiation is significantly stronger in Seyfert 1 than in Seyfert 2 and is often not observable in the latter. The continuum can even outshine the stellar contribution of the whole galaxy. Another distinction can be found in the X-ray luminosity, which is very strong for Seyfert 1 galaxies, while in Seyfert 2 galaxies the X-ray radiation appears to be absorbed by material in the line of sight (LOS) between object and observer. A more differentiated classification has been developed by [Osterbrock & Ferland \(2006\)](#). It defines subclasses like Seyfert 1.5, 1.8 and 1.9 depending solely on

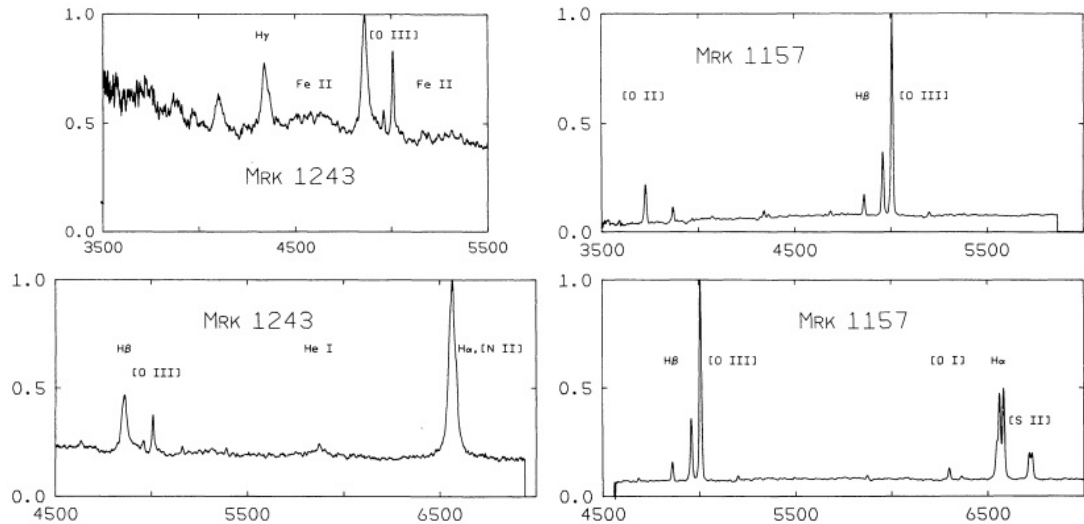


Figure 1.3: Typical optical spectra (intensity in arbitrary units vs. wavelength in \AA) of Seyfert 1 and Seyfert 2 galaxies. Left: Visual spectrum of Markarian Mrk 1243 as an example for a Seyfert 1 galaxy. Right: Visual spectrum of Mrk 1157 as an example for a Seyfert 2 galaxy. Taken from [Carroll & Ostlie \(2006\)](#)

the optical spectrum. In particular it takes into account the relative strength of the broad components of different Balmer emission lines.

1.1.2 Radio Galaxies

Like Seyfert galaxies, radiogalaxies can be divided into two classes according to the width of their emission lines. They are called broad-line radio galaxies (BLRG) and narrow-line radio galaxies (NLRG) and, in contrast to Seyfert galaxies, they are bright in the radio domain. Additionally, BLRG 'have a bright, starlike nucleus surrounded by a very faint, hazy envelope' ([Carroll & Ostlie, 2006](#)), while NLRG are mostly (giant) elliptical galaxies with and without a large halo of stars, and a central component dominating the emission (morphology types cD, D, and E). The source of the radio emission can be a compact core, the halo, radio lobes and/or jets, where the latter can connect the core with the lobes.

1.1.3 Quasars and Quasi-Stellar Objects

In the late 1950's the optical counterparts of 3C 48 and 3C 273, two important radio objects, were identified. In the optical they have a starlike appearance. Hence, they

1. INTRODUCTION AND OVERVIEW

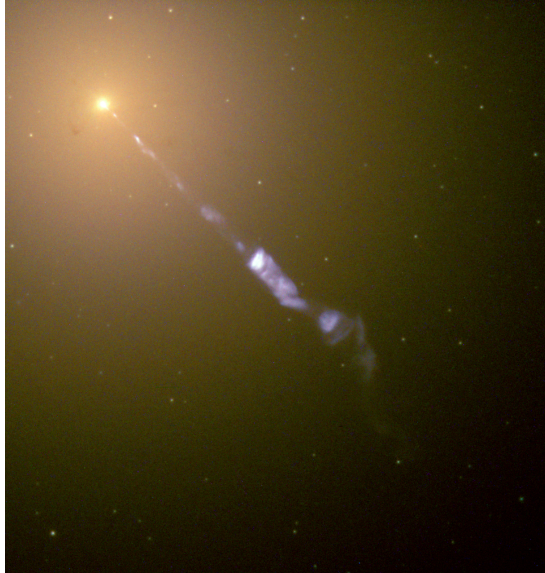


Figure 1.4: HST image of the jet feature in M87 observed in the visible wavelength domain. Image credits: NASA and The Hubble Heritage Team (STScI/AURA).

were dubbed ‘quasi-stellar radio sources’, shortly quasars. They display a peculiar with broad emission lines, which were later identified as strongly redshifted Balmer lines. As it turned out, 3C 48 is extremely distant, which means that it has to be extremely powerful in order to be detected. The bolometric luminosity of quasars is usually between 10^{45} to 10^{48} ergs^{-1} (Carroll & Ostlie, 2006). For comparison, common galaxies like the Milky Way have bolometric luminosities of $\sim 10^{43}$ ergs^{-1} (or $M_B < -21.5 + 5 \log h_0$). In order to maintain such a high energy output, Quasars are required to accrete about 1 to 10 $M_{\odot}\text{yr}^{-1}$. Furthermore, they show an ultraviolet (UV) excess. A result of this is the big blue bump, mentioned in Sect. 1.1.

The vast majority of the quasars ($\sim 90\%$) is called ‘quasi-stellar objects’ (QSO) because their ratio of radio-to-optical luminosity is comparably low with values < 10 (‘radio-quiet’). However, in the literature the term ‘QSO’ often comprises radio-loud *and* radio-quiet optically star-like sources, while the use of ‘quasar’ is restricted to the radio-loud class.

Almost all galaxies of both types have spectra that show the properties of Seyfert 1 AGN plus a strong continuum that obeys a power-law. Type 2 properties are not found amongst the QSO.

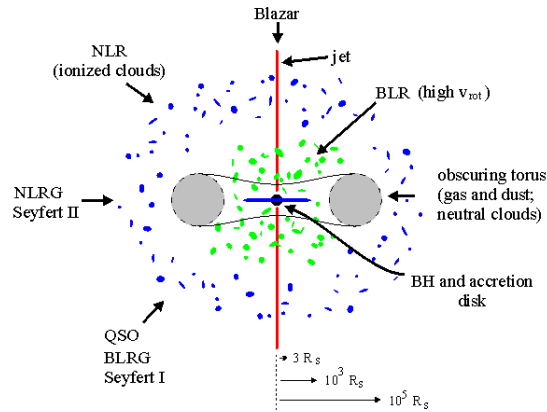


Figure 1.5: The unified model of AGN states that the class of AGN observed depends on the angle under which the the central part of the galaxy is seen (Credits: Stéphane Courteau, Queens University, Canada.)

1.1.4 Blazars, BL Lac objects, and OVV

Some AGN show strong and rapid variations in their radio spectra. Additionally, their emission is characterised by a high degree of linear polarisation, most likely due to synchrotron effects. These AGN are called ‘blazars’ and are always radio-loud. Their vast luminosity is believed to be a result of beaming, the collimation of flux due to relativistic effects (‘boosting’ and ‘abberation’). Hence, these AGN appear brighter than they intrinsically are, assuming isotropic emission.

‘BL Lac’ objects are a sub-clas of blazars, but lack almost completely any emission line. They are predominantly located in elliptical galaxies.

The ‘optically violently variable’ (OVV) quasars are comparable in their appearance to the BL Lacs, but they distinguish themselves by a much higher luminosity and, sometimes, broad emission lines.

1.1.5 The Unification Theory of AGN

The galactic nucleus, the central engine, must be provided with energy (also known as ‘fuelling’) to become active in the sense described in the afore sections. Nowadays, it is commonly accepted that most or even all galaxies host a SMBH in their center, which composes the central engine. The energy required for the nucleus to become active is likely provided via the accretion of matter, in the same or at least similar way for all

1. INTRODUCTION AND OVERVIEW

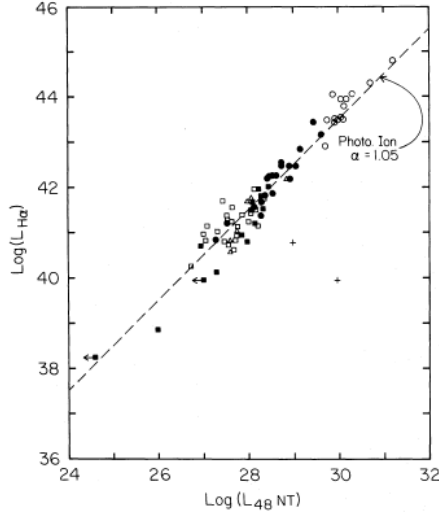


Figure 1.6: The logarithmic total $H\alpha$ luminosity in ergs s^{-1} vs. the logarithmic non-thermal continuum luminosity at $\lambda 4800 \text{ \AA}$ in $\text{ergs s}^{-1} \text{ Hz}^{-1}$, taken from Shuder (1981). Open Circles (QSOs), Seyfert 1 galaxies (filled circles), Seyfert 2 galaxies (open squares), narrow-line radio galaxies (triangles) from the work of Koski (1976). Seyfert 2 galaxies and emission-line galaxies from the survey of Shuder (1981) are depicted with filled squares.

galaxies. If so, the diversity of classes of AGN observed and described in sections 1.1.1 to 1.1.4 is only a result of orientation effects, the mass of the central black hole, and the accretion rate.

Mainly two different facts lead to the development of the unified model. First, the confirmation that in most kinds of AGN (except blazars) the luminosity of the $H\alpha$ emission line is proportional to the luminosity of the featureless continuum $L_{H\alpha} \propto L_{FC}$. This proportionality (with a slope $\simeq 1$) is expected if the hydrogen is photoionised by the continuum radiation. Therefore, the broad and the narrow component of $H\alpha$ emission line in AGN have the same origin.

The second fact is based on the discovery made by Antonucci & Miller (1985). The observation of the spectrum of the Seyfert 2 galaxy NGC 1068 in *polarised* light revealed features characteristic for a Seyfert 1. The polarised light comes from reflections from the interstellar medium. The conclusion is that Seyfert 2 galaxies may have the same nucleus as Seyfert 1s, but in type 2 galaxies the direct view on the nucleus is obstructed. The interstellar material acts like a mirror that enables the observer to

look behind the obstruction. Hence, the difference between Seyfert 1 and Seyfert 2 galaxies is founded in the orientation of the galaxy. The location of origin of the narrow emission lines is not the same as that of the broad emission lines. As a result, the unified picture of AGN has been developed and it consists of following components (see also Fig. 1.5):

Broad-Line Region: The broad-line region (BLR) is the area where the broad component of the emission lines are emitted. The emission lines are due to the photoionising continuum radiation of the AGN as the variability of the emission line fluxes correlate with the variations of the continuum intensity. It also is the strong variability of the recombination lines that leads to the conclusion that the BLR consists of clouds which are optically thick to ionising radiation. From their response time, their distance to the nucleus is calculated to of the order of lightdays to lightweeks). From the permitted lines, one can estimate the temperature of the BLR ($T \sim 10^4$ K), and its electron density ($10^9 \leq n_e \leq 10^{11} \text{ cm}^{-3}$). In Sect. 1.2 I will explain, how this information can be derived from emission line spectra.

Typically, forbidden emission lines in the BLR yield much lower densities than calculated from permitted emission lines. This is simply due to the high collision rates of the atoms and the low emission probabilities of forbidden transitions. The atoms are deexcited by collisions before the radiative transition can occur. In other words, the electron density is too high and the amount of necessary atoms is too small to allow for significant emission from forbidden transitions. Consequently, there are usually no broad components in forbidden emission lines.

The BLR is thought to be of clumpy nature (Peterson, 1997). The BLR clouds take only $\sim 1\%$ of the volume and are optically thick. The velocities of the clouds ($\sim 5000 \text{ km s}^{-1}$) are consistent with the expected values assuming the clouds are orbiting the SMBH at their observed distance.

Torus: The continuum emission of Seyfert 2 galaxies is weaker compared to those of type 1 galaxies and they do not show broad emission lines. Since both Seyfert types are basically the same, obscuring matter has to be in the line of sight toward the nucleus of Seyfert 2s, such that the observed continuum does not find its way on a direct path to the observer. Generally, an optically thick torus consisting of gas and

1. INTRODUCTION AND OVERVIEW

dust is assumed. It would permit continuum radiation to be emitted only in the direction of the axis perpendicular to the mid-plane of the torus. This manifests itself in large scale ionization cones. However, newer findings indicate the torus not to be ‘doughnut’-shaped but rather to be flatter and more complex in its composition and structure (e.g. [Bartscher et al., 2013](#); [Tristram et al., 2012](#)). The torus is likely to be opaque to soft X-ray, explaining why only hard X-ray emission is detected in Seyfert 2s.

Narrow-Line Region: Permitted and forbidden emission lines can be produced in the narrow-line region (NLR), which is located outside the torus. Because of its relatively low electron density ($\sim 10^4 \text{ cm}^{-3}$) and the presence of sufficient material, permitted and forbidden emission lines can be produced. Like in the BLR, the temperature in the NLR is $\sim 10^4 \text{ K}$ and it has a clumpy structure. Since the torus shields the gas clouds close to its plane, the gas is not ionised by the continuum radiation of the nucleus. In contrast, the clouds that are well above or below the plane of the torus have a direct line of sight to the nucleus and, therefore, are ionised. NLRs extend between 100 and 1000 pc and the clouds fill roughly $\sim 1\%$ of the space volume.

NLRs in Seyfert 2 galaxies are often subject to showing radial outflows, which is evidenced by a doppler-shifted blue wing in the narrow-line emission profile. The red wing, indicative for the outflow in the receding direction is believed to be often extinguished. Radiation pressure and winds originating from the accretion disk are possible mechanisms for radial outflows. Since their velocities are decreasing with radius it is believed that they are decelerated by the gravitational pull of the galaxy center. Jets, on the other hand, are massive energy outflows which are highly collimated compared to mass outflows like winds. Since jets entrain matter of the interstellar medium they can also be associated with wing components.

The viewing angle does not only account for the difference between Seyferts of types 1 and 2. It can furthermore explain the occurrence of blazars. According to the unified model, a blazar is observed, when looking directly into the jet of the galaxy. This explains the high luminosity, strong polarisation, and also variability. Their jets are believed not to have the same density throughout their structure. Within their jets the galaxies expel clumps of plasma of different size, density and therefore of different

luminosity. If a clump of plasma is crossing the line of sight the observed luminosity of the nucleus will vary.

1.1.6 Low Luminosity AGN - LINERs

In the previous sections, the establishment of a thorough picture of the different AGN classes, and their connection to each other has been described. However, the class of low-luminosity AGN (LLAGN) has been spared out. It deserves closer attention, since this work deals with NUGA galaxies, which are, by selection, LLAGN. They represent more than one third of all galaxies in the present time universe. In the following, I describe their appearance and properties and how they fit into the AGN picture. I give special emphasis to Low-Ionisation Nuclear Emission Regions (LINER) as most LLAGN are LINERs (and vice versa), and at least two out of three galaxies treated in this thesis are classified as LINER galaxies (NGC 5850 and NGC 3626). LLAGN also comprise transition objects, whose emission can be accounted to ionisation by a mixture of LINER and starburst (SB, strong star formation activity) objects. LLAGN are AGN with low bolometric luminosities (commonly $L_{\text{bol}} \lesssim 10^{42}$ erg s⁻¹ is assumed). The average luminosity of LINERs is $\langle L_{\text{bol}} \rangle \sim 10^{40}$ to 10^{41} erg s⁻¹.

1.1.6.1 Frequency of Detection

LINERs as a class of galaxies were first defined by Heckman (1980). They are characterized by high-luminosity emission lines of low-ionization species (e.g. [N II] $\lambda 6585$, [S II] $\lambda\lambda 6718, 6732$) with respect to the Balmer recombination lines and by a moderate [O III] $\lambda 5008$ luminosity when compared to those of Seyfert galaxies. The threshold is defined as $([\text{O III}]/\text{H}\alpha) < 3$ for LINERs (Osterbrock & Ferland, 2006). Further details on the identification criteria of LINERs will be given in Sect. 1.2.5.

LINERs can be found predominantly in the local universe, preferentially in early-type galaxies. The stellar population in the nuclear region is mainly evolved down to scales of $\lesssim 10$ pc towards the nucleus. In cases where a young stellar population is present in the nuclear region, its energetic impact is small.

More than 30% of all galaxies and 60% of Sa/Sab spirals with $B \leq 12.5$ mag are LINERs (Ho et al., 1997). Within the Palomar survey (Ho et al., 1997), LINERs can be detected in $\sim 20\%$, and transition objects in another $\sim 13\%$ of all observed sources. Kauffmann et al. (2003) analysed the spectra obtained by the Sloan Digital Sky Survey

1. INTRODUCTION AND OVERVIEW

(SDSS) and found 75% of all AGN to be LINERs. LINERs account for 1/3 of all galaxies and for 2/3 of all AGN. By numbers, LINERs are highly important objects within the AGN scheme. However, the latter assumes that all LINERs are indeed AGN. This is not always the case.

While Seyfert galaxies have clearly an AGN and are driven by accretion of matter onto a SMBH, it has been a long-standing matter of debate whether LINERs represent the low-luminosity (and/or low-accretion) tail of the AGN family or a class on their own. The debate is rooted in the fact that the observed line intensities in the circumnuclear gas of LINERs can be sufficiently powered by compact UV cores. This can be found in approximately 25% of the LINERs (Maoz et al., 1996). In the remaining 75%, the UV-core is likely present but obscured by dust. Although not excluded, the presence of a non-stellar source like an AGN would not be mandatory to achieve the observed energy output. The radiation observed in LINERs can, at least partially, be provided by a compact stellar cluster (e.g. Maoz et al., 1998; Pogge et al., 2000).

1.1.6.2 The Spectral Energy Distribution

If LINERs are AGN, one would expect them to have SEDs similar to those of more luminous active galaxies. Instead, the UV-domain is particularly different compared to luminous AGN. The optical-UV spectral index of LINERs is very steep ($\alpha_{\text{ou}} \approx -1$ to -2.5 compared to $\alpha_{\text{ou}} \approx -0.5$ to -0.7 in Seyferts; (Ho et al., 1996; Sabra et al., 2003)). This is due to the Big Blue Bump (BBB), commonly detected in AGN, but only weakly detected (if at all) in LLAGN/LINERs. Instead of the BBB, we find a flux excess in the infrared domain. Since the BBB is considered to be emission from an optically thick, geometrically thin accretion disk (Shields, 1978) emitting most of the ionising radiation, a major component of the AGN is missing.

Also in X-rays differences between LLAGN and other AGN can be found. LLAGN can have very steep X-ray spectral indices ($\alpha_{0.5-10 \text{ keV}} \approx -0.4$ to -1.2), though in average they do not differ that strongly from Seyfert 1 and radio-quiet quasars ($\langle \alpha_{0.5-10 \text{ keV}} \rangle \sim 0.8$ in LLAGN, $\langle \alpha_{0.5-10 \text{ keV}} \rangle \sim 0.87 \pm 0.22$ in Seyfert 1s (Nandra et al., 1997), and $\langle \alpha_{0.5-10 \text{ keV}} \rangle \sim 0.93 \pm 0.22$ in radio-quiet quasars (Reeves & Turner, 2000)). The SED of radio-loud quasars are comparably flatter with $\langle \alpha_{0.5-10 \text{ keV}} \rangle \sim 0.6 \pm 0.16$. The power-law component in the X-rays of LLAGN is only weakly absorbed, and this

is in contrast to the expected correlation of decreasing luminosity with increasing obscuration. Further, the long-term variability, observed in luminous galaxies, is rarely present in LLAGN (Ptak et al., 1998).

With some rare exceptions, LLAGNs are all radio-loud ($R_0 \equiv L_\nu(5 \text{ GHz})/L_\nu(B) \gtrsim 10$ or, alternatively, $R_X \equiv \nu L_\nu(5 \text{ GHz})/L_X \gtrsim 10^{-4.5}$). LINERs have mostly a flat radio spectrum $-0.2 \leq \alpha \leq 0.2$ (median spectral index of Seyferts is $\alpha = 0.4$) and show variability on the time scale of months. This short term variability is evidence for the radio emission to originate in a compact core or in the emerging point of a jet.

Furthermore, the AGN scenario (which assumes the AGN to be an unresolved point source) is particularly challenged by evidence of extended LINER-like emission in an increasing number of galaxies. Therefore, distributions of photoionising sources have been taken into consideration. Cooling flows (Fabian, 1994; Voit & Donahue, 1997) and photoionization by post-asymptotic giant branch (p-AGB) stars (Binette et al., 1994; Sarzi et al., 2010; Stasińska et al., 2008; Terlevich & Melnick, 1985; Trinchieri & di Serego Alighieri, 1991) are possible sources of LINER-like emission. Cooling flows are predominantly found in massive galaxies and clusters. Post-AGB stars can only explain LINERs with relatively weak emission lines (Binette et al., 1994; Cid Fernandes et al., 2009). These two mechanisms are not the only candidates for LINER-like emission. The characteristic emission can be shock induced as well. Several authors have calculated and modeled shocked gas in various configurations (Dopita & Sutherland, 1996; Heckman, 1980; Kewley et al., 2001; Rich et al., 2010). Especially in galaxies showing large scale outflows and in galaxy mergers, shock excitation is important (Lípari et al., 2004; Monreal-Ibero et al., 2010; Sharp & Bland-Hawthorn, 2010; Veilleux & Rupke, 2002) and resembles extended LINER-like spectra. In contrast to these intragalactic shock processes, Farage et al. (2010) observed extragalactic material spiraling inwards on an inclined trajectory in a brightest cluster galaxy NGC 4696. This filament structure exhibits LINER-like spectra over its entire extension, which is explained by ram-pressure induced shocks as a result of the transonic passage of a gas-rich galaxy. LINER-like spectra also have been reported for ionization cones emerging from the nucleus (e.g. Kehrig et al., 2012). However, despite the number of scenarios alternative to AGN, extended emission can be produced by an unresolved point source as well (e.g. Yan & Blanton, 2012). The resulting profile of the line emission depends on parameters like density, filling factor, and spatial distribution of the gas.

1. INTRODUCTION AND OVERVIEW

The idea of LINERs being LLAGN is supported by the detection of a compact radio core (Nagar et al., 2005) in many of these objects with medium radio powers of 10^{19} to 10^{21} W Hz⁻¹ at 5 GHz (Wrobel, 1991). Furthermore, the frequency of detection of compact radio cores in LINER 1s and LINER 2s is similar to their Seyfert counterparts (Ho, 2008). Phillips et al. (1986) and Ho (1999) found the detection rate of LLAGN in radio to be similar to the frequency of detection of optical emission lines. From these emission lines the objects are predominantly identified as LINER galaxies. The radio brightness temperature of LINERs is measured to be between 10^6 and 10^{11} K and therefore, the emission is definitively of non-thermal origin (Nagar et al., 2005).

There are more hints on the presence of AGN in LINERs. The UV-emission, if detected, is observed to be variable. Also the observation of hard X-ray cores (González-Martín et al., 2006) supports this idea, though one has to take care not to include extranuclear emission in the measurement. About 75% of the LINERs have at least faint ($L_{2-10 \text{ keV}} \sim 10^{38}$ erg s⁻¹) cores (Ho & Ulvestad, 2001). However, Flohic et al. (2006) found diffuse X-ray emission in 70% of their LINER-sample centrally concentrated within ~ 100 pc. In most cases it contributes more than 50% to the central X-ray luminosity. In normal E-galaxies we can also find similar luminosity distributions. In these objects the X-ray luminosity is produced by X-ray emitting gas originated in stellar ejecta (either due to stellar mass loss or SN Ia) that has been thermalised. This can also be the case in LLAGN. The excitation of the stellar ejecta results from collisions, in contrast to that of Seyfert galaxies, where usually photoionisation by the AGN is responsible.

The detection of broad-line H α emission in LINERs lead to the classification, analogous to Seyferts, of LINER 1 and LINER 2 and suggests the presence of an AGN. LINERs are low-luminosity sources and, as such, their emission lines are faint as well. It is very difficult to observe the weak and broad component of emission lines against the stellar continuum (especially of HII regions) of the galaxy and requires its careful subtraction. It is likely that the number of detections of broad emission lines (approximately in 25% of all LINERs) underestimates the real frequency of occurrence. Unlike to Seyfert 2 galaxies, the BLR in LINER 2s has not been observed in polarised optical emission. The conclusion is, that the broad line component is not always scattered towards the observer. Moreover, if no broad emission lines are detected at all, the BLR might simply not exist. In this case, the classification of LINERs in type 1 and type 2



Figure 1.7: An HST image of the sombrero galaxy (M104) as an example for a LINER 2 galaxy. Image credits: NASA and The Hubble Heritage Team (STScI/AURA).

is not a matter of orientation with respect to the observer, as described by the unified picture, but it is a matter of mere existence of the BLR. In Fig. 1.7 the Sombrero Galaxy (M104) is shown as a prime example of a LINER 2 without a polarised BLR.

In luminous galaxies, the width of the broad emission line component is inversely correlated to the BH mass and the bolometric or hard X-ray luminosity. [Laor \(e.g 2003\)](#) find a limiting bolometric luminosity of $L_{\text{bol}} \approx 10^{41.8} (M_{\text{BH}}/10^8 M_{\odot}) \text{ erg s}^{-1}$, yielding a cloud velocity of $\approx 25000 \text{ km s}^{-1}$. At higher velocities (and therefore lower luminosities) the clouds may be torn apart by shear or tidal forces. On the other hand, if the clouds of the BLR condensate out of radiation-driven winds ([Murray & Chiang, 1997](#)), then it is likely that low-luminosity sources cannot create a wind. Thus, the BLR cannot be created either. Lower limits for the luminosity to support a BLR have been estimated by [Elitzur & Shlosman \(2006\)](#). They find that BLRs disappear for $L_{\text{bol}} \lesssim 10^{42} \text{ erg s}^{-1}$, assuming the clumpy torus model. Assuming that the BLR is formed by an outflow from the accretion disk, [Nicastro \(2000\)](#) concludes the radius of the disk to decrease with Eddington ratio and calculate the BLR to vanish at $L_{\text{bol}}/L_{\text{Edd}} \lesssim 10^{-3}$ with $L_{\text{Edd}} \lesssim 10^{38} (M_{\text{BH}}/M_{\odot}) \text{ erg s}^{-1}$. One should keep in mind, that there are a number of galaxies, which simply do not conform with these models.

1. INTRODUCTION AND OVERVIEW

The power-law component in the X-ray spectra of LLAGN is only weakly obscured, in contrast to the expected inverse correlation of luminosity with obscuration. Further, the X-ray processing (Fe K α emission and Compton reflection) is weak, which is also supposed to become increasingly stronger with decreasing luminosity of the AGN. If observed at all, Fe K α is always a narrow line. Taking these all into account, we come to the conclusion that the torus might disappear at sufficiently low AGN luminosities. Indeed, most nearby LLAGN have Eddington ratios $L_{\text{Edd}}/L_{\text{bol}} < 10^{-3}$ compared to $L_{\text{Edd}}/L_{\text{bol}} = 10^{-1}$ to 10^0 for luminous AGN.

The question whether LINER 2 galaxies are AGN is basically the question of whether they are powered by accretion. Doubts on LINER 2s being AGN came up when it became clear that the X-ray SED can be fit with a combination of a power-law ($-1.5 < \alpha < -0.7$) and soft thermal emission. This resembles the SED of starburst (SB) galaxies. One cannot conclude directly on the existence of a connection between SB and LLAGN by the presence of extended hard X-ray emission and central star formation. On the other hand, $L_{\text{X}}/L_{\text{H}\alpha}$ is lower for LINER 2s than for LINER 1s (Ho & Ulvestad, 2001). Thus, if we extrapolate the X-ray luminosity to the UV, there are too few ionizing photons to account for the observed H α emission (Terashima et al., 2000). Since the X-ray emission is only little absorbed, if at all, only two possible explanations exist. Either a large fraction of the optical emission lines are produced by non-nuclear mechanisms or our idea on the SED of LINERs is incomplete. Probably both is true. The detection rates of radio and X-ray cores make the strongest case for LINER 2s being AGN. The ratio of detections between LINER 1s and LINER 2s is similar to Seyfert 1s and Seyfert 2s. This is likely a result of decreasing luminosity over the whole spectrum and consequently, LLAGN have low accretion rates.

To explain the low luminosity of LINERs, models of radiatively inefficient accretion flows (RIAF) and obscuration have been invoked (e.g. Dudik et al., 2009; González-Martín et al., 2009), although Ho (2008) dismissed the obscuration hypothesis for LLAGNs. RIAF models became necessary as evidence accumulated that LLAGN have enough fuel to power the central engine to generate luminosities common for AGN. The low luminosity has to be explained by a decreased efficiency of radiation. Basically, there are two main types of RIAF models. On one hand, the accretion efficiency can be reduced if the accreted matter is too tenuous. In this case the time for radiative

cooling is shorter than the time it takes to accrete the matter onto the central SMBH. This type of RIAF models focus on the low radiation efficiency and are predicted for accretion rates of $\dot{M} \lesssim 0.01\dot{M}_{\text{Edd}}$, a value LINERS are frequently found to be below. One of the known kinds of low radiation efficiency are the advection dominated accretion flows (ADAF). On the other hand, the low luminosity of LLAGN can be caused by inefficient accretion and jet feedback. These models make convection responsible for the removal of gravitational energy and angular momentum towards larger distances to the central SMBH. Global outflowing winds can have the same effect as well. They agree with the observation that the decrease of accretion correlates with increasing influence of jets.

LINER SEDs distinguish themselves from common AGN SEDs in several aspects. RIAF models do well in approximating the SED of LINERs, often in combination with a jet (e.g. [Fabbiano et al., 2003](#); [Quataert et al., 1999](#); [Yuan et al., 2002](#)). These models show only little similarity to SB-galaxies. As for LINERs, most of the radiation is emitted in the optical, UV, and thermal IR domains.

1.1.6.3 Energy Budget Considerations

Closely related to SEDs of LINERs are energy budget considerations. [Koratkar et al. \(1995\)](#) found a $L_{\text{H}\alpha}$ - L_{X} correlation for luminous sources. LLAGN concur with it approximately. No clear difference between LINERs and Seyferts was found, which supports the idea of LINERs being AGN. In the hard X-ray domain (2–10 keV) LINER galaxies of type 2 show an ionizing photon deficit. The extrapolation of the X-ray emission to the UV domain yields an $\text{H}\alpha$ luminosity, which is 10–100 times below the observed one. In contrast, LINER 1 galaxies follow the correlation $L_{\text{H}\alpha} \propto L_{\text{X}}^{1.1}$, valid for all broad line sources. This is the result of $L_{\text{UV}}/L_{\text{X}}$ decreasing with luminosity. LINER 1s are weaker than Seyfert 1s and they do not show the UV bump. Therefore, the ratio of $L_{\text{X}}/L_{\text{H}\alpha}$ in LINER 1s is a bit smaller than in Seyfert 1 galaxies. Some part of the narrow component of $\text{H}\alpha$ in LINER 1 sources is likely not to be photoionised by an AGN. This corresponds again to the photon deficit, which is characteristic for type 2 LLAGN. The photon deficit is best explained by the UV radiation from p-AGB stars ([Binette et al., 1994](#)). The stellar population within the central 100–200 pc can emit enough Lyman continuum photons to produce the $\text{H}\alpha$ emission observed in ~ 30 – 40% of all LINER 2 galaxies. However, this estimation has assumed a cloud covering factor

1. INTRODUCTION AND OVERVIEW

of $f_c = 1$, which is likely too high (more realistic is $f_c = 0.3$). Nevertheless, this scenario stays interesting, especially if one considers that p-AGB stars can also be responsible for LINER-like emission line ratios.

1.2 Spectroscopy and Physical Quantities

Spectra are composed of continuum emission, absorption lines, and emission lines. It is important to understand their physical background for the proper interpretation of the observed spectrum. Once this has been understood, a detailed analysis of the spectral features can be performed yielding a wealth of information about the object and the matter in the line of sight toward it. Here, I will constrain myself mostly to the optical wavelength domain according to the observational data analysed in this thesis.

1.2.1 The Components of Spectra

One can define the sphere of influence of a particle. It is given by its electromagnetic and gravitational forces and its size. This sphere of influence is called ‘cross section’, denoted with σ . For symmetry reasons, this idea can be regarded in two dimensions, rendering the sphere of influence into a circle of influence and giving the cross section the unit of area. Whenever a photon passes through the cross section of a particle, they will interact with each other.

An absorption/emission line is the result of such an interaction and manifests itself in the decrease/increase in intensity in a relatively small wavelength range. Absorption is best interpreted in terms of opacity, since photons emitted by a source are removed by matter in the line of sight (LOS) between the object and the observer. Generally, one can distinguish two basic mechanisms for photon removal, which again can come in different flavours: absorption and scattering.

Absorption means the destruction of the photon; it simply does not exist any more. In contrast, a scattered photon still exists but has changed its direction of movement such that it cannot be collected by the telescope (or any other optical instrument, like the eye). As said before, both remove photons from the beam of light and, therefore, increase the opacity κ . The observed intensity I is described by an exponential equation with I_0 being the initial unabsorbed/unscattered radiation intensity from the source:

$$I = I_0 e^{-\tau\lambda},$$

where τ_λ is the optical depth at wavelength λ , given by the integration of the opacity at λ over the thickness s of the absorbing/scattering medium; $\tau_\lambda = \int \kappa ds$.

The slow change of the opacity with wavelength composes the continuum radiation. The sudden change of opacity creates absorption lines, which requires the photon to have the exact energy needed for orbital transitions. For the production of absorption lines four different mechanisms can be held accountable.

1. **Bound-bound transitions:** By absorption of a photon an electron in an atom or ion can be transferred to another orbital. The photon must have the exact energy corresponding to the energy difference between the initial and the final orbital. Otherwise, no transition of the electron will occur. This process can be reversed by random or by stimulated downward transition of the electron to its initial orbit. This yields an emission line in the spectrum. The created photon is emitted in an arbitrary direction. Most likely it is not emitted again in the LOS. Therefore, bound-bound transition and the following downward transition resemble a scattering process, though the photon is absorbed. However, if the electron's downward transition does not lead to the initial orbital, the photon will not be recreated and is lost forever. Instead photons of other energies are created. In this case the process is truly an absorption.
2. **Bound-free absorption:** This process of absorption is also known as photoionisation and one of the most important for this work. A photon interacting with an atom has an energy higher or equal to the ionization energy of the atom. The atom is then ionised and releases an electron, which has a kinetic energy corresponding to the difference of the photon energy and the ionisation energy. The inverse process, the recombination of a free electron with an ionised atom, releases photons (free-bound emission). As the electron cascades downwards from one orbital to lower ones, the released photons have energies that represent exactly the energy differences between these different orbitals. The emission of photons at discrete energies manifests itself in sharp peaks in a spectrum: the emission lines.
3. **Free-free absorption:** Photons can be absorbed by electrons which are close to atoms. The absorption process increases the kinetic energy of the electron.

1. INTRODUCTION AND OVERVIEW

This is not confined to a certain wavelength area. Therefore, this process adds to the optical depth of the continuum. The reverse process, consequently, emits a photon as the electron loses kinetic energy as it is decelerated by a nearby ion. This is a bremsstrahlung mechanism.

4. **Electron scattering:** By ‘Thomson scattering’ a photon is scattered by a free electron. The small cross section of the electron has the size of about the photon’s wavelength. This makes the scattering very effective at high temperature and is therefore a major reason for opacity. Two other scattering mechanisms are of importance. Firstly, ‘Compton scattering’, the scattering of a photon by a weakly bound electron, which takes place if the photon wavelength is much smaller than the size of the atom. Secondly, ‘Rayleigh scattering’, which occurs for photons which have a wavelength much larger than the atom’s diameter.

The Balmer emission lines are of special importance in optical spectroscopy, as we will see in Sec. 1.2.5 and 1.2.4.1. The Balmer lines are indicative for electrons making transition between higher orbitals and the $n = 2$ energy level. These, and other emission lines, will be described in the following section.

1.2.2 Photoionisation and Recombination

1.2.2.1 The Hydrogen Atom

Though the mechanisms for the creation of emission lines have been shortly mentioned in Sec. 1.2.1, a more thorough treatment is necessary because of their importance for this work. Emission lines not only tell the observer that there is a particular element present in a gaseous state. The mere presence of some emission lines are indicative for certain astronomical objects. Other emission lines can be used to derive the physical conditions in the observed gas. In this and the following section, I shortly abstract the theory on recombination and photoionisation, and the physical quantities that can be derived from them. In large parts I will follow [Osterbrock & Ferland \(2006\)](#).

Prerequisite for the emission of one or several photons by an atom in a gaseous nebula is the excitation and/or ionisation of the gas. We consider first the ionisation by a radiation field, the so-called photoionisation.

1.2 Spectroscopy and Physical Quantities

The most simple, but also the most descriptive example is the assumption that we observe a gaseous nebula consisting of Hydrogen (H) only. Furthermore, we presume a radiation source which emits photons with energies higher than the ionisation potential of H (13.6 eV). Both assumptions are already very close to reality. H is by far the most abundant element in the universe and consequently it dominates the chemical composition in nebulae. The energy needed to photoionise the Hydrogen requires the photons at least to be emitted in the UV domain or to have even higher frequencies. Young stars (spectral type O and B) are sources of strong UV radiation and are almost always found close to shining nebulae. However, non-stellar sources can photoionise the gas as well and for those the same thoughts are valid.

Within any point of the nebula the gas is in ionisation equilibrium, which means that the number of photoionisations equals the number of recombinations of H-ions with free electrons. Mathematically expressed,

$$n(H^0) \int_{\nu_0}^{\infty} \frac{4\pi J_{\nu}}{h\nu} a_{\nu}(H^0) d\nu = n_e n_p \alpha(H^0, T) \text{ [cm}^{-3}\text{s}^{-1}\text{]}. \quad (1.1)$$

J_{ν} is the mean intensity of the incident radiation, which makes $\frac{4\pi J_{\nu}}{h\nu}$ to be the number of incident photons per unit area, unit time and unit frequency range. The ionisation cross section of H is represented by $a_{\nu}(H^0)$, with typical values of 10^{-18}cm^2 . Therefore, the whole integral corresponds to the number of photoionisations per H-atom per unit time or, analogously, to the inverse lifetime τ_{ph}^{-1} of an atom until it is ionised, which is commonly of order $10^{-8}\text{[s}^{-1}\text{]}$. $n(H^0)$ is the number density of neutral H-atoms per unit volume. The number of recombinations per unit volume and unit time is described by the term on the right-hand side of the equation with n_e and n_p being the density of free electrons and protons, respectively. Here the recombination coefficient is denoted with $\alpha(H^0, T)$.

With the simple conversion of the mean intensity to radiative flux and further to units of luminosity ($4\pi J_{\nu} = \frac{L_{\nu}}{4\pi r^2} \text{[erg cm}^{-2}\text{s}^{-1}\text{Hz}^{-1}\text{]}$ with r being the distance to the radiation source), we can calculate the number of incident photons per second in a point within the cloud:

$$Q(H^0) = \int_{\nu_0}^{\infty} \frac{L_{\nu}}{h\nu} d\nu \text{ [photons s}^{-1}\text{]}. \quad (1.2)$$

1. INTRODUCTION AND OVERVIEW

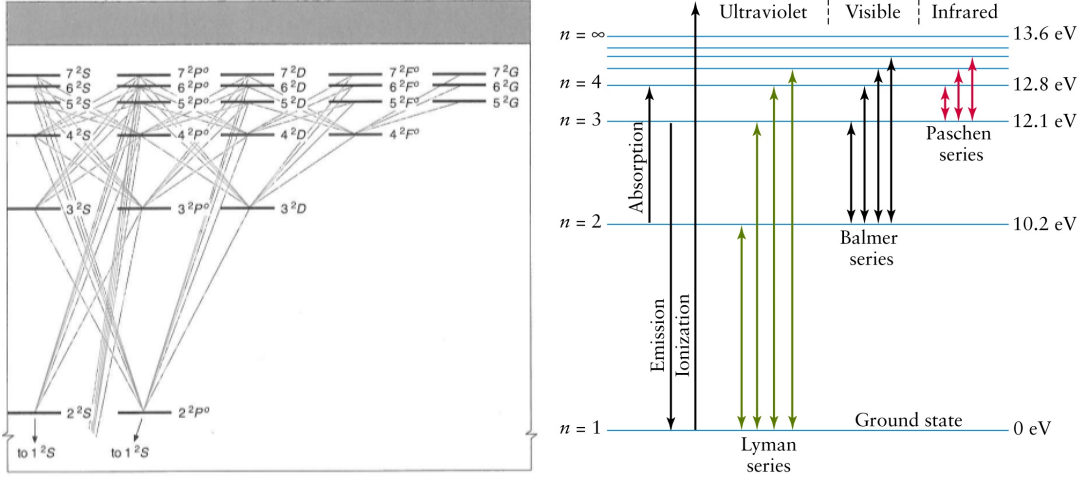


Figure 1.8: **Left:** Energy-level diagram (Grotrian diagram) for neutral hydrogen. This diagram is restricted to low n and low L . The lines connecting different levels show permitted radiative transitions. Taken from [Osterbrock & Ferland \(2006\)](#). **Right:** Energy-level diagram as in the left panel, but neglecting the orbital information (L) and showing the wavelength regime of the emitted photons for each transition.

The size of the ionised volume depends on the strength of the source. However, within this size the nebula is almost completely ionised. This area is called the ‘Strömgren sphere’ but is also often referred to as the ‘H II region’. In a very thin zone, connected immediately to it, the transition from ionised to neutral gas (H I) takes place. The thickness of the transition zone has approximately the length of one mean free path of the ionising photon ($l \approx [n(\text{H}^0)a_\nu]$) and is typically of order 0.1 pc. Further outwards the Hydrogen is only neutral.

After recombination, the electron cascades quickly downwards to the ground level ($n = 1$) by changing its principal quantum number n and its angular momentum quantum number $L = 0, 1, 2, 3, \dots$ (often denoted with S, P, D, F, ..., respectively, see left panel of Fig. 1.8). The selection rule of $\Delta L = \pm 1$ is almost always obeyed for each transition. The probability for a transition from one level to another is of order $10^4\text{--}10^8 \text{ s}^{-1}$. Only the downward transition from $2 \ ^2S \rightarrow 1 \ ^2S$ is significantly less likely with 8.23 s^{-1} . It is a so-called ‘forbidden’ transition because it does not obey the selection rule. The term ‘forbidden’ is to be interpreted as ‘very unlikely’. All the given probabilities can be converted to average lifetimes of an electron in a certain level

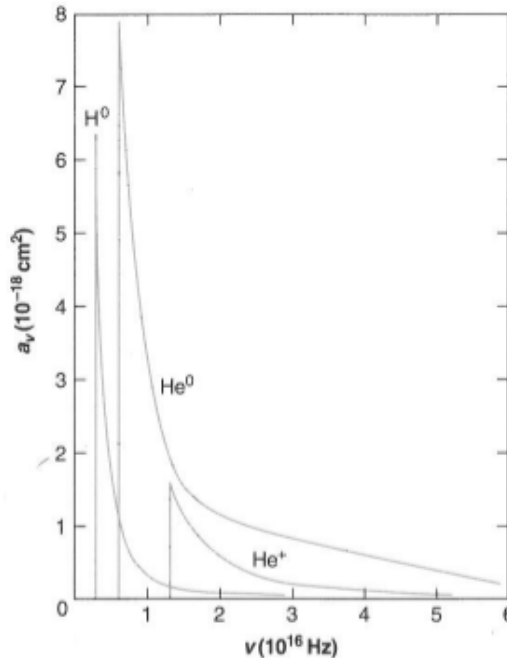


Figure 1.9: Cross section for the absorption of photons with sufficient energy to ionise the atom. Here it is shown for H^0 , He^0 , and He^+ . Taken from [Osterbrock & Ferland \(2006\)](#).

by inversion. The time scale for the downward transitions is much smaller than the average lifetime of the H-atom until it is photoionised ($\tau_{\text{ph}} \approx 10^8$ s). This justifies the assumption that the number of photoionisations in a nebula is equal to the number of recombinations, since after each recombination the downward transition takes place immediately, bringing the H-atom back to its ground state.

In the right panel of Fig. 1.8 we can see that only the emission lines of the Balmer-Series are of interest for this work. These are the only hydrogen recombination lines detectable in the optical wavelength regime.

The cross section of a hydrogen-like atom in its ground state is a function of nuclear charge Z and the ratio of the ionization potential and the energy of an interacting photon. In Fig. 1.9 the cross section for different atoms and ions is plotted against the photon energy. The cross section is largest for photons with an energy close to the ionisation energy of the atom and quickly decreases with approximately ν^{-3} . From this we can conclude that harder radiation (photons with energy higher than the ionization potential) have a higher chance to ‘miss’ the neutral atom and, consequently, travel

1. INTRODUCTION AND OVERVIEW

deeper into the nebula. This explains also the observed hardening of the radiation with distance to the ionising source.

Photoionisation leads to free electrons with an energy distribution which is a function of mean intensity of the radiation (J_ν), the photoionisation cross section (a_ν), and the energy of the incident photon ($h\nu$). However, this energy distribution does not last for long. The electrons collide elastically with each other because the cross section for this kind of scattering is much bigger than for any other mechanism. Hence, the energy distribution assumes a Maxwell-Boltzmann one, where the collisional processes are defined by the local temperature T . The recombination coefficient for a certain n and a certain 2L is then described by the velocities of the electrons u , the recombination cross section $\sigma_n \ ^2L$ and the Maxwell-Boltzmann energy distribution of the electrons $f(u)$:

$$\alpha_n \ ^2L(\text{H}^0, T) = \int_0^\infty u \sigma_n \ ^2L(\text{H}^0, u) f(u) \, du \text{ [cm}^3\text{s}^{-1}\text{]} \quad (1.3)$$

with

$$f(u) = \frac{4}{\sqrt{\pi}} \left(\frac{m}{2kT} \right)^{3/2} u^2 e^{-\frac{mu^2}{kT}}. \quad (1.4)$$

From these equations we can see that $\alpha_n \ ^2L(\text{H}^0, T) \propto T^{-1/2}$ and the cross sections are $\propto u^{-2}$.

Summing up the electron captures to all levels gives us the total recombination coefficient α_A to a level n . From this the recombination time can be calculated, $\tau_r = 1/(n_e \alpha_A)$, which has typically values $\approx 10^5/n_e$ years.

1.2.2.2 Cloud of Hydrogen

The afore described mechanisms of photoionisation and recombination took only one radiation source and its impact on a spot of Hydrogen into account. As usual, nature is more complicated. Of course, the radiation cannot go infinitely through a cloud of Hydrogen but is absorbed, as we could already guess from the mentioned hardening of the radiation. The behaviour of radiation within a medium is described by the radiation transfer equation:

$$\frac{dI_\nu}{ds} = -n(\text{H}^0) a_\nu I_\nu + j_\nu. \quad (1.5)$$

1.2 Spectroscopy and Physical Quantities

I_ν denotes the specific radiative intensity and j_ν describes the local emission coefficient in units of energy·(unit volume)⁻¹·(unit time)⁻¹·(solid angle)⁻¹·(unit frequency)⁻¹. The radiation does not only come from a stellar source but also from the nebula itself, since it emits photons as a result of recombination. This is often called ‘diffuse’ radiation. Hence, the specific intensity can be written as the sum of the stellar and the diffuse radiation field:

$$I_\nu = I_{\nu s} + I_{\nu d}. \quad (1.6)$$

While the stellar contribution decreases as a function of absorption in the cloud and distance to the star, the diffuse radiation from the nebula itself can contribute photoionising photons. For low temperatures $kT \ll h\nu_0$ the ionising photons come only from recombinations directly to the ground level 1^2S .

The mean intensity $J_{\nu d}$ in an **optically thin** nebula is ≈ 0 . In an **optically thick** nebula the photons can hardly leave the nebula and instead they are absorbed again very close to the location of their creation. This is called the ‘on-the-spot’ approximation, which is close to reality, since the photons have energies close to the ionisation potential. This in turn yields the largest recombination coefficient (see Sec. 1.2.2.1). In this case is $J_{\nu d} = j_\nu / (n(\text{H}^0)a_\nu)$. The bottom line is that ionising photons, resulting from recombinations to the ground level, are quickly absorbed again and therefore, are without impact on the ionisation balance.

1.2.2.3 Cloud of Hydrogen and Helium

The ionisation structure of any cloud is very well described if the second most abundant element ($\sim 10\%$ in terms of number density) is taken into account as well: Helium (He). Its ionisation potential is 24.6 eV. The photons emitted by hot O-stars are sufficiently energetic to ionise He to He⁺ (or analogously He I to He II). The implication is that photons with energies between the ionisation potentials of H and He ($13.6 \text{ eV} < h\nu < 24.6 \text{ eV}$) ionise the Hydrogen only. Every photon with energy higher than 24.6 eV can ionise either Hydrogen or Helium. This has effects on the geometric ionisation structure of the nebula. We assume as a first case that most of the photons have energies just above the ionisation potential of H and only a small number of photons is

1. INTRODUCTION AND OVERVIEW

more energetic than the ionisation energy of He. The low-energy photons then keep the H ionised while basically all high energy photons ionise the He. The result is that the small core of the nebula is a mixture of H II and He II. Around this core the gas is a mix of H II and neutral He I. In the other extreme case, where the radiation is dominated by photon energies beyond 24.6 eV, all atoms are ionised, resulting in a large region consisting of H II and He II. There will be no neutral gas surrounding the completely ionised core.

The cross section of He can be calculated in the same way as for H. However, for the total recombination coefficient one has to take into account that He has two electrons, which results in singlet and triplet levels.

The on-the-spot approximation to derive the ionisation equations can be used for a cloud-mix of H and He, but there are some issues that have to be kept in mind. The fraction of the diffuse radiation of the nebula, that comes from the recombination to the ground level of He, can again ionise He *and* H. Further, a number of photons are emitted by the recombination of He to other levels than the ground level, which cannot ionise He but nevertheless, are capable to ionise H. Finally, the metastable 2^3S level can be depopulated by deexcitation to the ground level emitting a forbidden photon at 19.8eV. However, collisional excitation by electrons can depopulate this level as well, but for typical n_e in H II regions ($\leq 10^{-2}\text{cm}^{-3}$) this can be neglected.

Though the ionisation of He II to He III can play a significant role, I do not treat this topic here, since it goes beyond the purpose of this work. I refer the interested reader to [Osterbrock & Ferland \(2006\)](#).

1.2.2.4 Metals

Elements heavier than He (commonly called ‘metals’ by astronomers) obey the same equation of equilibrium between photoionisation and recombination (see Eq. (1.1)). Because of their low abundance, the diffuse contribution to the ionisation can usually be neglected.

The energies needed to photoionise metals are higher than usually provided by stars. Once an electron has been removed from any shell within the atom, different processes can set in. Either electrons from outer shells drop down to fill the gap emitting a number of high energy photons or the Auger effect takes place, a combination of downwards

cascading electrons and the release of electrons. These effects contribute to the X-ray spectrum and are not important for the optical domain.

1.2.3 Collisional Excitation

Very important for this work, but also as a cooling mechanism compared to radiative cooling, is the excitation of ions (like O^+ , O^{++} , O^{+++} and N^{++}) by collisions with electrons. The low-energy levels of such ions have a special characteristic: they are of the order of kT while the excitation energy for H and He is much higher. This makes the metal ions an effective medium to cool the nebula, in contrast to H and He, which cannot cool via collisions.

The cross section σ_{12} for excitation from level 1 to level 2 is a function of kinetic energy of the electron. Electrons with energies below $h\nu_{21}$ are not able to excite the ion and therefore, $\sigma_{12} = 0$. Above this limit, σ scales approximately with u^{-2} , where u is the velocity of the electron. We assume the thermodynamic equilibrium, which means that each excitation is balanced by a deexcitation and that the Boltzmann equation applies. Then we can describe the connection between excitation and deexcitation as

$$\omega_1 u_1^2 \sigma_{12}(u_1) = \omega_2 u_2^2 \sigma_{21}(u_2), \quad (1.7)$$

where σ_{21} is the cross section for deexcitation and ω_i ($i = 1, 2$) are the statistical weights of their respective energy levels. Of course, after the collision the energy has to be conserved,

$$\frac{1}{2} m u_1^2 = \frac{1}{2} m u_2^2 + h\nu_{21}. \quad (1.8)$$

From the collisional cross section for deexcitation σ_{21} the collisional deexcitation rate per unit volume and per unit time can be calculated similar to Eq. (1.3):

$$n_e n_2 q_{21} = n_e n_2 \int_0^\infty u \sigma_{21} f(u) du. \quad (1.9)$$

The collisional excitation rate per unit volume and per unit time is

$$n_e n_1 q_{12} = \frac{\omega_2}{\omega_1} q_{21} e^{-h\nu_{21}/kT}. \quad (1.10)$$

1. INTRODUCTION AND OVERVIEW

The electric-dipole selection rules do not permit any radiative transitions between the ground and the excited level. However, there is a small chance for the magnetic-dipole/electric-quadrupole transition, creating the forbidden lines in the spectra of nebula or the ISM.

For very low electron densities we can assume that every collisionally excited ion falls back to ground state by the emission of a forbidden photon. The cooling rate L_C per unit volume is then simply calculated by

$$L_C = n_e n_1 q_{12} h \nu_{12}. \quad (1.11)$$

For very high n_e the deexcitation by collisions becomes important. Cooling is not as efficient as for low electron densities and the cooling rate is described by

$$L_C = n_e n_1 q_{12} h \nu_{21} \left[\frac{1}{1 + \frac{n_e q_{21}}{A_{21}}} \right], \quad (1.12)$$

with A_{21} as the probability for the radiative transition from level 2 to level 1.

Most ions have more than only two low-energy levels, and are more complicated to handle since collisional transfers and radiative transfers between all levels are possible. These ions (e.g. O^{++} and N^+) are very important for the analysis of the optical spectra in this work. The cooling rate for $n_e \rightarrow 0$ is calculated from the sum of Eq. (1.11) for all the different levels involved. For a high density gas the equilibrium equation has to be calculated completely taking all levels into account. It is convenient to define a critical density

$$n_c(i) = \sum_{j < i} A_{ij} / \sum_{j \neq i} q_{ij}, \quad (1.13)$$

where collisional deexcitation is not needed to be taken into account for $n_e < n_c(i)$.

1.2.4 Optical Emission Lines as Indicators for Physical Conditions

The optical domain of the spectrum roughly extends from 4000Å to 8000Å. Though this section treats the physical conditions derived from emission lines, I do not intend to touch the topics related to velocities. Here I assume the reader is familiar with the basic concepts of Doppler shifts and mechanisms concerning the width of emission lines.

1.2 Spectroscopy and Physical Quantities

However, the central statement is that the displacement of an emission line from its rest wavelength is a measure for the radial velocity of the gas or the stars,

$$v = \frac{\lambda_{\text{observed}} - \lambda_{\text{rest}}}{\lambda_{\text{rest}}} c, \quad (1.14)$$

and the width of an emission line is a measure of the order of the motion. The latter is commonly expressed as Full Width at Half Maximum (FWHM) or by the standard deviation of an assumed Gaussian shape of the emission line designated with σ . It can also be expressed in units of velocities using Eq. (1.14).

In the following I briefly comment on the emission lines that are most important for this work and describe how they are produced. More emission lines exist and they will be described shortly along the text whenever is necessary.

1.2.4.1 Extinction within the Nebula

To derive physical quantities from a spectrum it is necessary to remove any effects of extinction caused by the intergalactic or interstellar medium. The extinction does not apply to all parts of the spectrum in the same way but affects shorter wavelengths stronger compared to longer wavelengths. Consequently, the extinction results in the ‘reddening’ of the spectrum, changing the relative luminosity between short and long wavelengths towards the longer, redder wavelengths. The actually observed flux f_{obs} and the ‘real’ intrinsic flux of an object f_{int} are linked by

$$f_{\text{obs}}(\lambda) = f_{\text{int}}(\lambda) 10^{-0.4A_V \cdot \frac{A_\lambda}{A_V}}. \quad (1.15)$$

A_V denotes the total extinction in the optical band (V-band) in units of magnitude and serves as a reference extinction. The extinction in any wavelength is commonly expressed in terms of *visual* extinction to make communication among scientists easier. In principal A_V could be canceled out in the exponent of this expression, but it is left to emphasise two things: First, the choice of that reference wavelength is arbitrary and the calculation would also work with the extinction in any other wavelength, if preferable and known. Second, the equation is based on the comparison of extinction in different

1. INTRODUCTION AND OVERVIEW

spectral areas (which introduces A_V as a normalisation factor in the equation). It is important to understand that $\frac{A_\lambda}{A_V}$ is a function of λ : $\frac{A_\lambda}{A_V} = \frac{A_\lambda}{A_V}(\lambda)$.

The description of the extinction is approached by defining the ratio of A_V to the color excess between the blue optical/UV band (U-band) and the V-band $E_{B-V} = A_B - A_V$. The ‘color excess’ is also called ‘selective extinction’. E_{B-V} is the amount by which the $B - V$ color of an object is changed. The ratio of total extinction to color excess is then defined as

$$R_V = \frac{A_V}{E_{B-V}}. \quad (1.16)$$

With these ingredients we can calculate the extinction at a given wavelength A_λ by

$$A_\lambda = k(\lambda)E(B - V) = \frac{k(\lambda)A_V}{R_V} \quad (1.17)$$

$$\Leftrightarrow \frac{A_\lambda}{A_V} = \frac{k(\lambda)}{R_V}, \quad (1.18)$$

where $k(\lambda)$ is the reddening curve. The reddening curve has been derived for several environments like the Milky Way (Allen, 1976; Fitzpatrick & Massa, 1986; Seaton, 1979), the Small and the Large Magellanic Cloud (Bouchet et al., 1985; Fitzpatrick, 1986; Prevot et al., 1984), and high redshift starburst galaxies (Calzetti et al., 2000). R_V has been derived e.g. by comparison of UV observations with NIR/optical data for molecular clouds (Cardelli et al., 1989) and has a value of ≈ 3.1 . Depending on the environment other values might be more applicable (e.g. Calzetti, 1997). We combine (1.18) with Eq. (1.15) and derive

$$A_V = -2.5R_V \frac{\log(f_{\text{obs}}/f_{\text{int}})}{k(V)}. \quad (1.19)$$

With this equation we are now in a position to use the ratio of observed flux from different wavelengths ($f_{\text{obs}}(\lambda_1)$, $f_{\text{obs}}(\lambda_2)$) and compare it with the relative intrinsic flux ($f_{\text{int}}(\lambda_1)$, $f_{\text{int}}(\lambda_2)$),

$$A_V = -2.5R_V \frac{\log\left(\frac{f_{\text{obs}}(\lambda_1)/f_{\text{obs}}(\lambda_2)}{f_{\text{int}}(\lambda_1)/f_{\text{int}}(\lambda_2)}\right)}{k(\lambda_1) - k(\lambda_2)}. \quad (1.20)$$

1.2 Spectroscopy and Physical Quantities

If the latter is known, we can conclude on the extinction, which in turn enables us to derive the absolute intrinsic flux. This technique is popular in spectroscopy, where the observed flux ratio of emission lines is compared with the value expected from theory. In optical spectroscopy the Hydrogen emission lines are commonly used and the flux ratio of Balmer lines is referred to as the ‘Balmer decrement’.

The emission lines of the Hydrogen Balmer series ($H\alpha$, $H\beta$, $H\gamma$, $H\delta$) are results of the recombination and downward transition process to level $n = 2$, as described in Sec. 1.2.2.1. The intensity of the lines, expressed in terms of the emission coefficient $j_{nn'}$ of the involved level is determined by the population n_{nL} in the level and orbital nL :

$$j_{nn'} = \frac{h\nu_{nn'}}{4\pi} \sum_{L=0}^{n-1} \sum_{L'=L\pm 1} n_{nL} A_{nL,n'L'}. \quad (1.21)$$

However, this is valid only for the extreme case of optically thin nebulae, which assumes that every produced recombination photon can escape the nebula and, hence, cannot induce any upward transitions in the atoms. This is commonly dubbed ‘Case A’. Since those nebulae are so sparse in gas they are also faint and hard to observe. Indeed, most easily observable nebulae are optically thick in the Lyman resonance line of H I. Every Lyman photon absorbed by an H-atom has a certain chance to be simply scattered back into the gas. But there is also the lower chance of converting the Lyman photon into several photons of lower energy. For example, in average the $Ly\beta$ photon is converted to $H\alpha$ and two continuum photons after nine scatterings. Similar holds for the $Ly\gamma$ photon, which is turned after a few encounters with atoms into a Paschen $Pa\alpha$, a $Ly\alpha$, and an $H\alpha$ photon, or into an $H\beta$ plus two continuum photons. We can conclude that the large optical depth leads to the assumption that every Lyman photon is scattered several times and eventually converted to a number of photons with lower energy, which in turn correspond to Hydrogen emission lines. This assumption is commonly called ‘Case B’.

The recombination spectrum can be numerically calculated and yields the emission line intensities depending on the electron density and the temperature. The ratio of different Hydrogen emission lines can then be compared with the observed spectrum as described before. Required are valid assumptions or constraints on the temperature and the electron density in the observed gas. Any deviation between the observed and

1. INTRODUCTION AND OVERVIEW

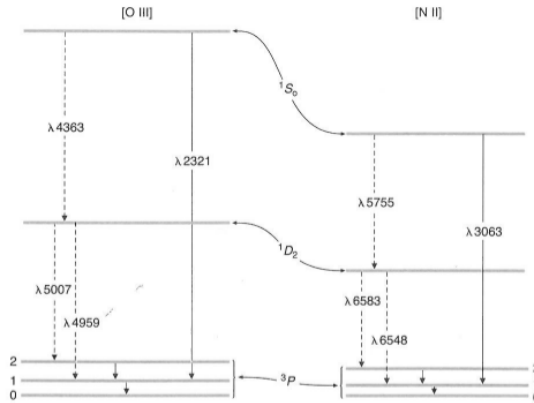


Figure 1.10: a

and [N II].] Energy level diagrams for [O III] and [N II]. Taken from [Osterbrock & Ferland \(2006\)](#).

the theoretical emission line ratio is then accounted to extinction effects. For a typical gaseous nebula the temperature is of the order of 10^4K and $n_e \sim 10^{-2}\text{cm}^{-3}$. For the most commonly used Balmer decrement, consisting of $\text{H}\alpha$ and $\text{H}\beta$ emission lines, this yields a value of $\text{H}\alpha/\text{H}\beta = 2.86$. Consequently, Eq. (1.20) is transformed to

$$A_V = -2.5R_V \frac{\log\left(\frac{f(\text{H}\alpha)/f(\text{H}\beta)}{2.86}\right)}{k(\text{H}\alpha) - k(\text{H}\beta)}. \quad (1.22)$$

1.2.4.2 Temperature

In the low-density limit we can neglect collisional deexcitation. The emission lines [O III] and [N II] are the result of radiative deexcitation after the ions were collisionally excited by electrons (see Sec. 1.2.3 and Fig. 1.10). The excitation energy depends on the input energy coming from the electron, namely its kinetic energy. Since the electrons' energy distribution follows the Maxwell-Boltzmann distribution, it is determined by the temperature. Therefore, the ratio of the population of different excited levels can be used to calculate the electron temperature of the gas.

The relative population of each energy level can be exactly calculated as roughly sketched out in Sec. 1.2.3. Hence, the temperature can be calculated purely from emission line ratios. Most commonly used and most important for the optical wavelength range are [O III] and [N II]:

$$[\text{O III}] : \frac{j_{\lambda 4960} + j_{\lambda 5008}}{j_{\lambda 4364}} = \frac{7.9 \times e^{(3.29 \times 10^4/T)}}{1 + 4.5 \times 10^{-4} n_e / T^{1/2}} \quad (1.23)$$

$$[\text{N II}] : \frac{j_{\lambda 6549} + j_{\lambda 6585}}{j_{\lambda 5756}} = \frac{8.23 \times e^{(2.5 \times 10^4/T)}}{1 + 4.4 \times 10^{-3} n_e / T^{1/2}} \quad (1.24)$$

Note that the electron density of the observed gas is needed. How this can be derived from the spectrum is described in Sec. 1.2.4.3. However, we will see that n_e is derived from other emission lines than [O III] and [N II]. Therefore, the derived density does not necessarily reflect the one of the ions used for the temperature measurements.

The temperature can, alternatively, be calculated from the relative strength of the recombination line and the recombination continuum belonging to the same recombination as the emission line. The continuum emission is a result of free-bound and free-free mechanisms which involve free electrons (see Sec. 1.2.1). As mentioned before, the velocity distribution of the free electrons is a function of T . As an example for the optical domain, one can choose the H β ($\lambda = 4862\text{\AA}$) emission line and the continuum near to it, which includes the continuum emission of the two-photon excitation from the $n = 2$ level and the He I recombination continuum. The ratio H β / νF_ν decreases with decreasing T . However, this method is difficult to apply since small contributions from other emission lines can have a serious effect on the measurement.

1.2.4.3 Electron Density

We remember from Sec. 1.2.3 that the collisional (de)excitation is a function of electron density. If we find the right circumstances, we should be able to calculate the electron density of the gas from the observed spectrum.

We consider two emission lines of the same ion, commonly [O II] $\lambda\lambda 3730 + 3727$ or [S II] $\lambda\lambda 6717 + 6732$ are used in the optical domain. These lines are characterised by radiative deexcitation from different levels and have almost the same excitation energy. Consequently, their photoionisation cross section is the same but they differ in the collisional cross sections. In other words, their relative excitation rate depends only on the relative collision strength. Given that the probability for radiative deexcitation or for collisional deexcitation is different for each level, the relative population of the

1. INTRODUCTION AND OVERVIEW

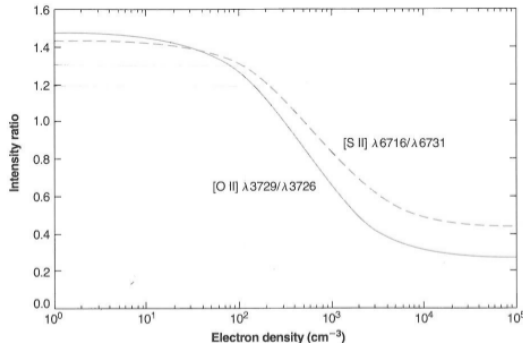


Figure 1.11: The emission line intensity ratios of $[\text{O II}]\lambda 3730/[\text{O II}]\lambda 3727$ (solid line) and $[\text{S II}]\lambda 6717/[\text{S II}]\lambda 6732$ (dashed line) as a function of electron density for a gas at $T = 10^4$ K. Taken from [Osterbrock & Ferland \(2006\)](#).

involved levels - and with it the emission line intensity ratio - will be a function of density only.

In the low-density limit, the emission line intensity ratio corresponds simply to the statistical weights of the relative excitation rates of the two levels because basically no collisional deexcitation takes place and every downward transition is a radiative one. From Fig. 1.11 we can see that in this case the emission line intensity ratio of $[\text{O II}]\lambda 3730/[\text{O II}]\lambda 3727 \approx 1.5$ and of $[\text{S II}]\lambda 6717/[\text{S II}]\lambda 6732 \approx 1.45$. In the high-density limit, in contrast, collisional deexcitation plays again an important role enforcing a Boltzmann population ratio. The emission line ratios are then described by the ratio of their statistical weight *and* the probability for a collisional deexcitation. The emission line ratios have values of around 0.34 and 0.41 for $[\text{O II}]$ and $[\text{S II}]$, respectively. However, one should be aware that the emission line intensity ratio slightly depends on the temperature with $n_e/T^{1/2}$. The derivation of density has similar issues as the temperature calculations. The temperature is yielded by an ionised species which differs from the one used to calculate the density and therefore the temperature is not necessarily valid.

1.2.5 Diagnostic Diagrams

Now, with the theory of emission line production as the thorough foundation, we can interpret the spectra in terms of ionisation mechanisms. Seyfert galaxies are often identified by an emission-line flux ratio of $[\text{O III}]/\text{H}\alpha$ with values greater than three. This is not unambiguous because very low-metallicity starforming (SF) regions can show

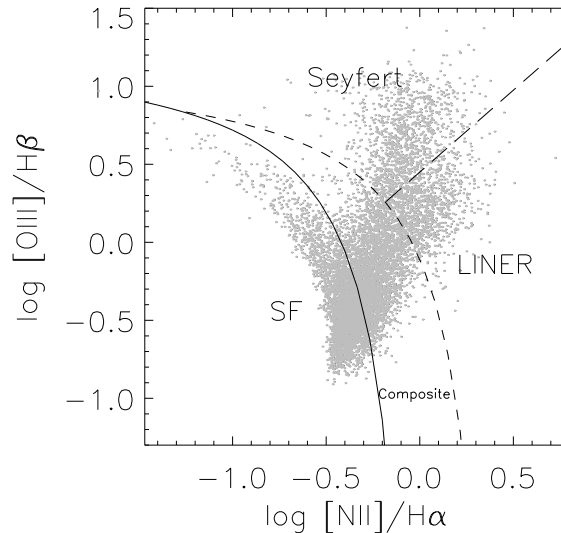


Figure 1.12: The BPT diagnostic diagram (Baldwin et al., 1981) adopted from Vitale et al. (2013): $\log([\text{O III}]\lambda 5008/\text{H}\beta)$ vs. $\log([\text{N II}]\lambda 6585/\text{H}\alpha)$. The solid line represents the pure SF demarcation line by Kauffmann et al. (2003), the short-dashed line corresponds to the extreme SB line by Kewley et al. (2001), and the long-dashed line denotes the Seyfert-LINER demarcation by Schawinski et al. (2007).

similar emission line ratios and therefore, other means are needed to distinguish whether the interstellar gas is ionised by AGN, a young stellar population, or a composite radiation source. Baldwin et al. (1981) developed the so-called diagnostic diagram (also BPT-diagram, named after their inventors), which was refined by Veilleux & Osterbrock (1987). These diagnostic diagrams (hereafter I abbreviate them with DD) show mostly the ratio of emission-line fluxes of a high-ionisation species to that of a Balmer emission line on one axis versus the ratio of a low-ionisation species to another Balmer line on the other axis.

The intention of this diagram was to distinguish whether the radiation field that ionises the interstellar gas has its origin in an AGN or in a young stellar population. With the Sloan Digital Sky Survey (SDSS) the DDs were again proven a very successful tool. As it turned out, to the surprise of many, the galaxies occupy a certain space with in the diagrams (see Fig. 1.12). In the $\log([\text{O III}]\lambda 5008/\text{H}\beta)$ vs. $\log([\text{N II}]\lambda 6585/\text{H}\alpha)$ DD, the galaxies compose an image which is commonly called the ‘seagull’. It is most

1. INTRODUCTION AND OVERVIEW

comprehensive to explain the meaning of the emission line ratios by using this DD.

We start in the upper left corner of panel a) in Fig. 1.12. The galaxies are characterised by high $[\text{O III}]\lambda 5008/\text{H}\beta$ values. From this line ratio alone we cannot determine whether the emission line flux $[\text{O III}]$ is high or the one of $\text{H}\beta$ is low. We remember Sec. 1.2.2.1 or 1.2.4.1, where it was explained that the emission line ratio of Balmer emission lines is relatively constant. This provides us with the opportunity to estimate whether $\text{H}\beta$ is low or high. If we assume a SF-region, the Balmer emission lines are strong. The UV-radiation of hot young stars is not hard enough to photoionise $[\text{O III}]$. However, if the temperature is high enough also $[\text{O III}]$ emission lines can be observed. Here, other metals come into play, e.g. $[\text{N II}]$. Generally, the cooling of a gas is most effective via the emission of photons by a metal. As a result we can therefore say, that in SF-regions with low metallicity the $[\text{N II}]\lambda 6585/\text{H}\alpha$ emission-line flux ratio is low while $[\text{O III}]\lambda 5008/\text{H}\beta$ is high. The higher the metallicity, the better the cooling works and the fainter $[\text{O III}]$ is. This behaviour forms the left ‘wing’ of the seagull, which is also called the ‘metallicity’ sequence, and it represents the SF-galaxies. [Kauffmann et al. \(2003\)](#) empirically derived a demarcation line where all galaxies to the left of it show emission line ratios purely due to SF.

The efficiency of cooling is not unlimited and at a certain metal-abundance threshold the cooling effect will not increase any further. If a source with a harder radiation field than a SF region is present then the metal lines like $[\text{N II}]$ increase stronger than the Balmer lines. Additional $[\text{O III}]$ is observed, because it is a result of collisional excitation, or in other words, it is a result of increasing temperatures. These sources are most notably AGN, but also shocks or a stellar population of post-AGB stars, and others.

[Kewley et al. \(2001\)](#) define a demarcation line that indicates the line ratios for the strongest possible starburst galaxies. Everything beyond, on the right hand side of the DD, cannot be due to SF alone. The area between the Kauffmann and the Kewley demarcation lines is considered as the ‘composite’ region. This name is misleading since pure AGN sources as well as pure SB-galaxies can be located in this region. However, real composite objects are also present there.

A third demarcation line has been developed by [Schawinski et al. \(2007\)](#), which distinguishes the LINER population from the Seyfert galaxies.

1.2 Spectroscopy and Physical Quantities

The DDs are designed to determine the dominant ionising mechanism in the nuclei of galaxies. It is clear that the emission line ratios depend heavily on the aperture used to observe the spectrum of galaxy. If we assume a spiral galaxy, then the aperture might comprise SF activity in areas that do not belong to the nucleus. As a result a nucleus containing an AGN could be classified as a composite object. The area comprised by the aperture is also a function of distance of the galaxy to the observer. It is important to keep this in mind while using DDs.

1. INTRODUCTION AND OVERVIEW

2

NGC 5850

2.1 Introduction

Low-ionization nuclear emission regions (LINERs) were first defined by Heckman (1980). They are characterized by high-luminosity emission lines of low-ionization species (e.g. [N II] $\lambda 6585$, [S II] $\lambda\lambda 6718, 6732$) with respect to the Balmer recombination lines and by a moderate [O III] $\lambda 5008$ luminosity when compared to those of Seyfert galaxies. The bolometric luminosity of LINERs is weak, even when compared to the Seyfert galaxies. While Seyfert galaxies have clearly an active galactic nucleus (AGN) and are therefore driven by accretion onto a super-massive black hole (SMBH), it has been a long-standing matter of debate whether LINERs represent the low-luminosity (and/or low-accretion) tail of the AGN family or represent a class on their own. Given their substantial frequency of appearance (more than 30 % of all galaxies and 60 % of Sa/Sab spirals with $B \leq 12.5$ mag; Ho et al. (1997)) LINERs pose an important piece in the picture of galaxy/AGN evolution. In principal, the debate is rooted in finding that the observed line intensities in the circumnuclear gas of LINERs can be sufficiently powered by compact UV cores. Although not excluded, the presence of a non-stellar source like an AGN would not be mandatory. The necessary radiation can at least partially be provided by a compact stellar cluster (e.g. Maoz et al., 1998; Pogge et al., 2000). Furthermore, the AGN scenario is particularly challenged by evidence of extended LINER-like emission in an increasing number of galaxies. Therefore, distributions of photoionizing sources have been taken into consideration. Cooling flows (Fabian, 1994; Voit & Donahue, 1997) and photoionization by post-asymptotic giant branch (p-AGB) stars (Binette et al., 1994;

2. NGC 5850

(Sarzi et al., 2010; Stasińska et al., 2008; Terlevich & Melnick, 1985; Trinchieri & di Serego Alighieri, 1991) are possible sources of LINER-like emission. Cooling flows are predominantly found in massive galaxies and clusters. Post-AGB stars can only explain LINERs with relatively weak emission lines (Binette et al., 1994; Cid Fernandes et al., 2009). These two mechanisms are not the only candidates for LINER-like emission. The characteristic emission can be shock induced as well. Several authors have calculated and modeled shocked gas in various configurations (Dopita & Sutherland, 1996; Heckman, 1980; Kewley et al., 2001; Rich et al., 2010). Especially in galaxies showing large scale outflows and in galaxy mergers, shock excitation is important (Lípari et al., 2004; Monreal-Ibero et al., 2010; Sharp & Bland-Hawthorn, 2010; Veilleux & Rupke, 2002) and resembles extended LINER-like spectra. In contrast to these intragalactic shock processes, Farage et al. (2010) observed extragalactic material spiraling inwards on an inclined trajectory in the brightest cluster galaxy NGC 4696. This filament structure exhibits LINER-like spectra over its entire extension, which is explained by ram-pressure induced shocks as a result of the transonic passage of a gas-rich galaxy. LINER-like spectra also have been reported for ionization cones emerging from the nucleus (e.g. Kehrig et al., 2012). However, extended emission can be produced by an unresolved point source as well, despite the number of scenarios alternative to AGN (e.g. Yan & Blanton, 2012). The resulting profile of the line emission depends on such parameters as the density, filling factor, and spatial distribution of the gas.

The idea of LINERs being low-luminosity AGN (LLAGN) is supported by the detection of compact radio (Nagar et al., 2005) and hard X-ray cores (González-Martín et al., 2006) in many of these objects. Furthermore, the frequency of detection of compact radio cores in LINERs and Seyferts is similar (Ho, 2008). To explain the low luminosity of LINERs, models of radiatively inefficient accretion flows and obscuration have been invoked (e.g. Dudik et al., 2009; González-Martín et al., 2009), although Ho (2008) dismissed the obscuration hypothesis for LLAGNs.

I present the data of NGC 5850¹ observed with the optical integral field spectrograph (IFS) VIMOS. The galaxy NGC 5850 is a prototype double-barred early-type spiral galaxy (SBb(sr) I-II) (Buta & Crocker, 1993; Friedli et al., 1996; Prieto et al., 1997). It is located at a distance of 34.2 Mpc (Wozniak et al., 1995). Its two spiral arms

¹Based on observations obtained with VIMOS at ESO VLT under program ID 083.B-0906(A).

form a ring-like structure, almost resembling the morphology of the center, where the inner bar (projected half-length of $6''.2$) is surrounded by a (pseudo-) ring. The spiral arms are distorted $\sim 2'$ west and southwest from the center, probably due to a recent (< 200 Myr) high-velocity encounter with NGC 5846 (Higdon et al., 1998), which is $10'$ to the northwest of NGC 5850. In optical color images, Lourenso et al. (2003) found the large scale (primary) bar and the inner (secondary) bar to differ in their projected position angle by -67° ($\text{P.A.}_{\text{secondary}} \approx 49.3^\circ$). The nested bar morphology is not a very rare feature. Laine et al. (2002) found in their sample of 112 nearby ($v_{\text{hel}} < 6000 \text{ km s}^{-1}$) galaxies that $(28 \pm 5)\%$ of the barred spiral galaxies and $(13 \pm 4)\%$ of non-Seyfert galaxies are double-barred. Observations of NGC 5850 with the optical IFS SAURON by de Lorenzo-Cáceres et al. (2008) showed significant drops in the stellar velocity dispersion exactly at the tips of the inner bar, which they attribute to contrast effects between the high dispersion of the bulge and the low dispersion of the bar. The existence of a gaseous polar disk, instead of the secondary bar, was suggested by Moiseev et al. (2004), who also used an optical IFS. They also found the core to be kinematically decoupled. From here on, I refer to the kinematically decoupled core as KDC. The low X-ray luminosity $L_X(0.5 - 3 \text{ keV}) = 10^{40.36} \text{ erg s}^{-1}$ suggests NGC 5850 to be in a state of low activity, and Fabbiano et al. (1992) did not consider it likely to be dominated by an AGN. The high luminosity of [N II] lines at the center classifies it as a LINER (Heckman, 1980; Keel, 1983a).

Integral field spectroscopy in the visible wavelength regime allows us to study the excitation mechanisms of the gas and to investigate the gas kinematics in detail. The proximity (high angular resolution), the low luminosity (no outshining by the AGN), and the double-barred structure of NGC 5850 make it an ideal object to study the gas excitation and kinematics in a LINER galaxy.

After describing the observations and how I treat the data to retrieve the needed information in Sect. 2.2, I describe the morphologic, kinematic, and excitational properties of NGC 5850 (Sect. 2.3). In Sect. 2.4, I discuss the results within different assumed scenarios or under certain aspects (i.e., H II-regions). I summarize our results in Sect. 2.5. Throughout this chapter I assume $H_0 = 75 \text{ km s}^{-1} \text{ Mpc}^{-1}$ with standard ΛCDM cosmology ($\Omega_{\text{matter}} = 0.27$, $\Omega_{\text{vacuum}} = 0.73$).

2.2 Observations, data reduction, and line measurements

2.2.1 Observations and data reduction

The observations were undertaken in April and May 2009 at the ESO Very Large Telescope (VLT) unit *Melipal* with the Visible Multi-Object Spectrograph (VIMOS; [Le Fèvre et al. \(2003\)](#)) in Paranal, Chile. The VIMOS was configured in IFU mode with high spectral resolution for the blue (4100 – 6300 Å) and the red (6500 – 8650 Å) grating and a spectral sampling of 0.54 Å and 0.58 Å, respectively. This provides a spectral resolving power of $R \sim 2700$ at 5500 Å and ~ 3200 at 7500 Å. The opening angle of the lenslets attached to the fibers is $0''.66$, resulting in a field of view (FOV) of $27'' \times 27''$ with 40×40 pixels. The observations were conducted for each grating separately with an integration time of 755 s per exposure. Three images per grating were taken, consisting of 1600 spectra each. For each set of three images, the second one was pointed to an apparently source-free region to observe the sky emission. Overall, I have eight on-source exposures in the blue grating and twelve in the red grating with a total integration time of 6040 s and 9060 s, respectively. The exposures are seeing limited with the worst seeing of $\text{FWHM} = 0''.86$ (blue) and $0''.84$ (red).

I used the VIMOS pipeline in version 2.3.3 for the basic data reduction steps, which comprises bias correction, spatial extraction, wavelength calibration, relative transmission correction, and flux calibration. The exposures suffered from a ‘fringing-like’ pattern ([Lagerholm et al., 2012](#)), a spectral and spatial high frequency variation depending on the telescope orientation. The possible origin of fringing in the case of VIMOS is discussed in [Jullo et al. \(2008\)](#). A technique to correct for it has been described in [Lagerholm et al. \(2012\)](#) but is only recommended for objects similar to early-type galaxies with spatially slowly changing spectra. For our data, I corrected for the fringing-like pattern based on the flat images taken in the same night as the science exposures. I fitted a medium-order polynomial (on order 4 to 6) to each normalized spectrum of the lamp flat exposures and divided the flat spectrum by the fit. The result is the normalized fringe pattern for each fiber, which shows a standard deviation of about $\sigma \sim 2.5\%$ in the blue grating and $\sigma \sim 8\%$ in the red one. This approach assumes that the true flat spectrum is dominant on large wavelength scales and does not change significantly on small scales. Furthermore, the fringing-like pattern itself should not change too much with detector position. I found the fit to be less reliable

2.2 Observations, data reduction, and line measurements

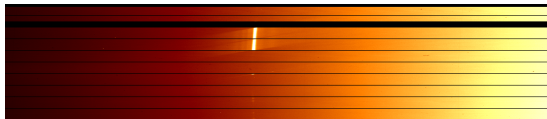


Figure 2.1: Part of a flat image as extracted by the VIMOS pipeline. Each horizontal line corresponds to a fiber and therefore to a spatial pixel. The wavelength axis extends from left (small λ) to right (high λ). The reflection at $\sim 5100 \text{ \AA}$ is clearly visible.

at the high wavelength end in the red grating. Therefore, I discarded the spectrum redwards of 6800 \AA . This also comprises parts at the edge of the spectrum that are unreliable (e.g., sudden intensity jumps). I divided the normalized flat images by the fit to retrieve the fringe pattern. Simple division of the science image by the fringe pattern removed the problem quite well. Since I discarded the spectral areas that could not be fitted well in the flat image, the fringing had an influence of only $\simeq 5 \%$.

The flat exposures were contaminated by a strong reflection in quadrant 4 between 5000 \AA and 5200 \AA (Fig. 2.1). Since this spectral area contains important emission lines (redshifted [O III] $\lambda\lambda 4960, 5008$) and influences the fringe correction, I attempted to compensate for this by assuming a perfect detector response in this regime of the spectrum. The intensity variation between spatial pixels (spaxels) was corrected by scaling each spectrum to the median emission-line flux of the 5577 \AA sky line for the blue grating data and 7316 \AA sky line for the red.

Although dedicated sky observations have been performed, they could not be used because of the unexpected variability of the detected sky lines in intensity and in shape. I estimated the influence of the sky continuum on the galaxy spectrum to be only 5% , and therefore, I decided to correct for contaminations in emission lines only where necessary.

The individual cubes were combined after aligning them using the galaxy center as reference. I also corrected for differential atmospheric refraction (DAR; Filippenko (1982)), which had a maximum influence of about 0.3 pixels corresponding to $0''.2$. Further I calibrated our ground based spectra to the wavelength range in vacuum (Edln, 1966; Morton, 1991). I corrected for Galactic reddening using the extinction law by Cardelli et al. (1989) with $E(B - V) = 0.056$.

Up to this point, I treated each grating separately. For the latter performed fit of the stellar continuum, it was advantageous to have as many stellar features (e.g., absorption

2. NGC 5850

lines) in each spectrum as possible. For this reason, I created a common data cube containing both VIMOS gratings as I describe in the following. I found the centroid position of the galaxy center of NGC 5850 to have a slightly different position in the SDSS g-band image compared to the SDSS i-band image. The spatial difference is $0''.2$. I used these images as a reference for the blue and red cube, respectively, to spatially align the cubes. The g- and the i-band are not fully covered by our remaining VIMOS spectra but by a dominant fraction. Afterward, the blue grating spectra were deteriorated to the sampling of the red grating spectra; both were combined and eventually shifted to the rest wavelength.

I used the observed spectrophotometric standard stars for the relative flux calibration of the spectra via the VIMOS pipeline recipe. The absolute flux calibration was performed by scaling the spectra to the available SDSS spectrum. From the VIMOS cube, I extracted a stacked spectrum corresponding to the PSF of the SDSS. The SDSS fiber diameter is $3''$, and I assumed the worst seeing, given by the 80-percentile seeing information in the header of the SDSS plate with $3''.46$. Because there is an observational gap between the gratings ($6145 - 6400 \text{ \AA}$) in the VIMOS spectra, I scaled both parts separately. In Fig. 2.2, I show the results of the scaling procedure. Bluewards of $\sim 5000 \text{ \AA}$, the VIMOS spectrum shows flux densities, which are by 5 – 10 % lower than the ones of the SDSS spectrum. This is a result of the reflection in the flat spectra mentioned above and its influence on the fringe correction.

To enhance the S/N, I convolved each cube slice (i.e., image of each wavelength bin) with a Gaussian of $FWHM = 2 \text{ px}$.

2.2.2 Continuum Subtraction and Emission Line Measurements

I used the stellar population synthesis program STARLIGHT (Cid Fernandes et al., 2005) to subtract the stellar continuum by fitting a linear combination of stellar template spectra to each spaxel in the VIMOS cube. I used the library of theoretical simple stellar population (SSP) models by Bruzual & Charlot (2003), which is based on a Chabrier initial mass function. I limited the library to a maximum age of 11 Gyr. All emission lines, visible sky lines (Hanuschik, 2003), telluric absorption features, artifacts, and the observational gap between the gratings were masked for the STARLIGHT

2.2 Observations, data reduction, and line measurements

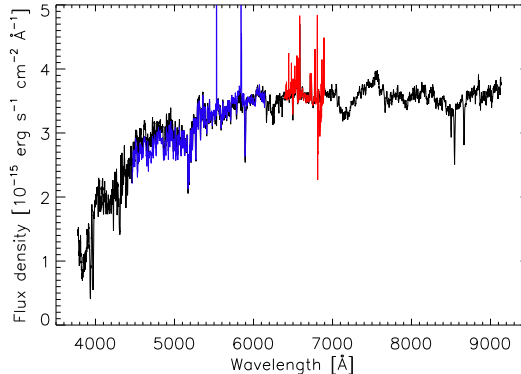


Figure 2.2: NGC 5850 spectrum from the SDSS with 3'' aperture in black. The scaled VIMOS spectrum observed with the blue grating is overplotted in blue; the one observed with the red grating is overplotted in red. All shown VIMOS spectra are extracted from an aperture with a diameter corresponding to the SDSS aperture and considers the seeing conditions. All spectra are shown in the rest-wavelength system. As explained in the text, the spectra are not corrected for sky contamination.

fit. Figure 2.3 shows the spectra, fit results, and residuals for different representative regions. To ensure a minimum quality of the fit, I clipped all spaxels, when STARLIGHT shows an absolute deviation (ADEV) of more than 4 %.

The intensities and the kinematic information of the emission lines were derived by the fitting of a double-component Gaussian to [N II] $\lambda 6585$ and its sky-line contamination. The peak of the sky-line fit was constrained to a narrow wavelength range instead of a fixed wavelength to consider possible instabilities of the emission line. I derived this wavelength range from spectra in which the sky-line was stronger than the [N II] emission. All other emission lines were fitted with a single Gaussian. The [N II] $\lambda 6550$ emission line was fitted simultaneously with H α ; both emission lines of the [S II] $\lambda\lambda 6718 + 6732$ doublet were fitted together. The fit was additionally constrained by keeping the spectral position difference of the line peaks fixed. I used the IDL routines MPFITEXP and MPFITPEAK for this tasks. The uncertainties were calculated from the fitted parameter errors via error propagation. The input uncertainties are given by the standard deviation of the continuum in a line-free region that is close to the respective emission line in the input spectra. As noted by Asari et al. (2007), the SSP models used for the stellar continuum fit have a weak hump around the H β line. Consequently, the line base after stellar continuum subtraction is positioned in the negative

2. NGC 5850

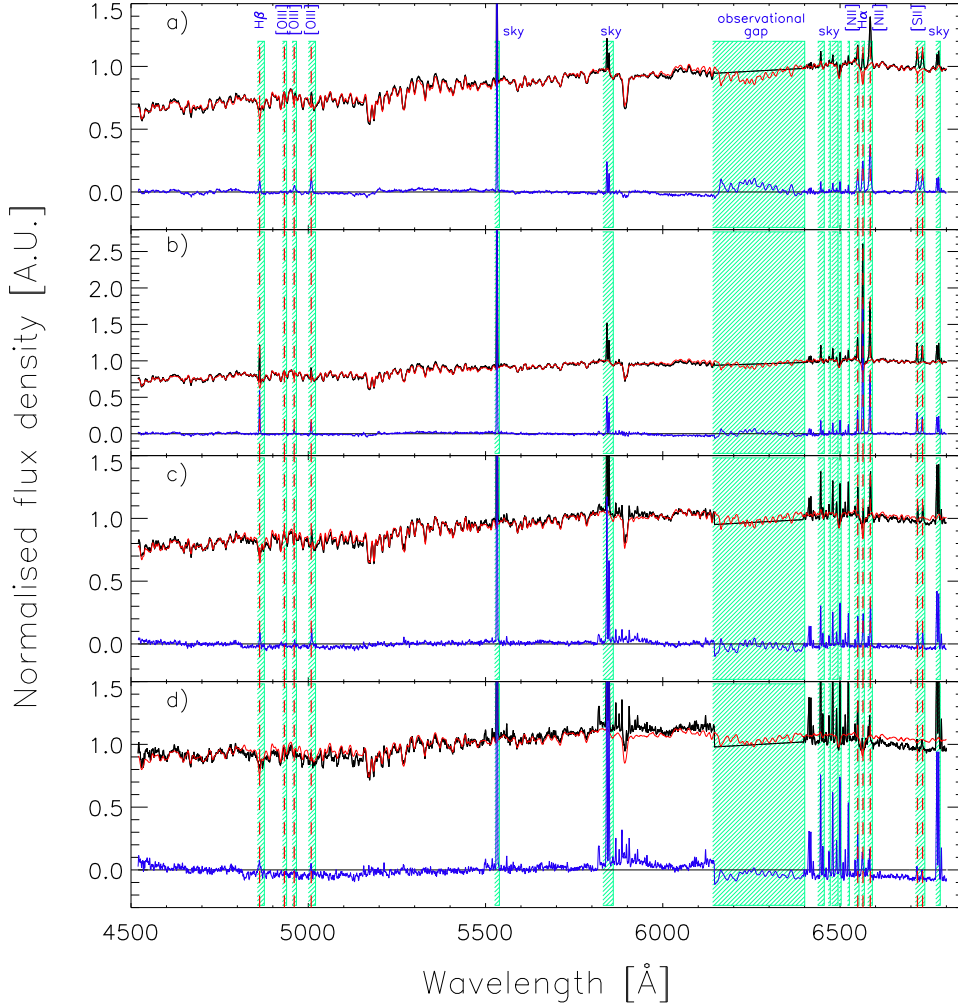


Figure 2.3: Spectra of different regions (given in arbitrary units; A.U.) within NGC 5850 before stellar subtraction (black) with overplotted stellar continuum fits by STARLIGHT (red) and residual spectrum (blue). The galaxy’s emission lines, the most prominent sky emission lines, and the observational gap between the blue and the red grating have been masked and are marked by the green colored boxes. The panels show the following regions: a) central pixel of NGC 5850, b) a star-formation region, c) a spectrum in a medium distance from the galaxy’s center ($\approx 6''$), and d) a spectrum extracted from a spaxel at the edge of the remaining FOV (ADEV $> 4\%$; see text for details).

flux regime. As this is a simple offset, I used the negative continuum as the baseline of the Gaussian fit.

In general, only emission line detections with a S/N that exceed 3σ were used for further analysis (emission line maps, kinematic maps). Additional spaxels were clipped if the uncertainties of the fits were nevertheless high (relative error $> 33\%$) or if the contrast in the map benefited from it. One should keep in mind that the use of single Gaussian fits disregards possible line asymmetries. In Sect. 2.3.2, I revisit this topic again.

The emission line fluxes were corrected for extinction only if necessary - that is, for the calculation of emission line ratios of spectrally distant emission lines, luminosities, and values based on them - such as in star-forming rates in high S/N areas. For this, I made use of the Balmer decrement $H\alpha/H\beta$. I applied the Calzetti extinction law (Calzetti, 1997) and a theoretical Balmer ratio of 2.863 (Osterbrock & Ferland, 2006), which corresponds to case-B recombination for a region with an assumed temperature of 10^4 K and an electron density of $n_e \sim 10^2 \text{ cm}^{-3}$ as derived from the [S II] emission line ratio.

In summary, the data reduction and the clipping described in Sect. 2.2.1 and 2.2.2 leave us with a FOV of $\sim 21'' \times 19''$ in the largest extensions. The PSF has a size of $FWHM \simeq 2''$. This value is based on the PSF of a spectrophotometric standard star and has been calculated by considering the worst seeing in our science exposures and smoothing. The spatial sampling is $0''.66$. The spectra cover a range from 4520 \AA to 6800 \AA with an observational gap from $6145 - 6400 \text{ \AA}$. The spectral sampling is 0.58 \AA and the median spectral resolution is $FWHM_{\text{line}} \approx 2 \text{ \AA}$.

2.3 Results

2.3.1 Morphology

The 6000 to 6100 \AA continuum image of NGC 5850 (Fig. 2.4) shows an elongated structure, which strongly peaked in its center, that agrees with the location of the inner (secondary) bar derived by Lourenso et al. (2003). They calculated the position angle (P.A.) of the secondary bar to be $49.3^\circ \pm 1^\circ$ similar to our own elliptical fits

2. NGC 5850

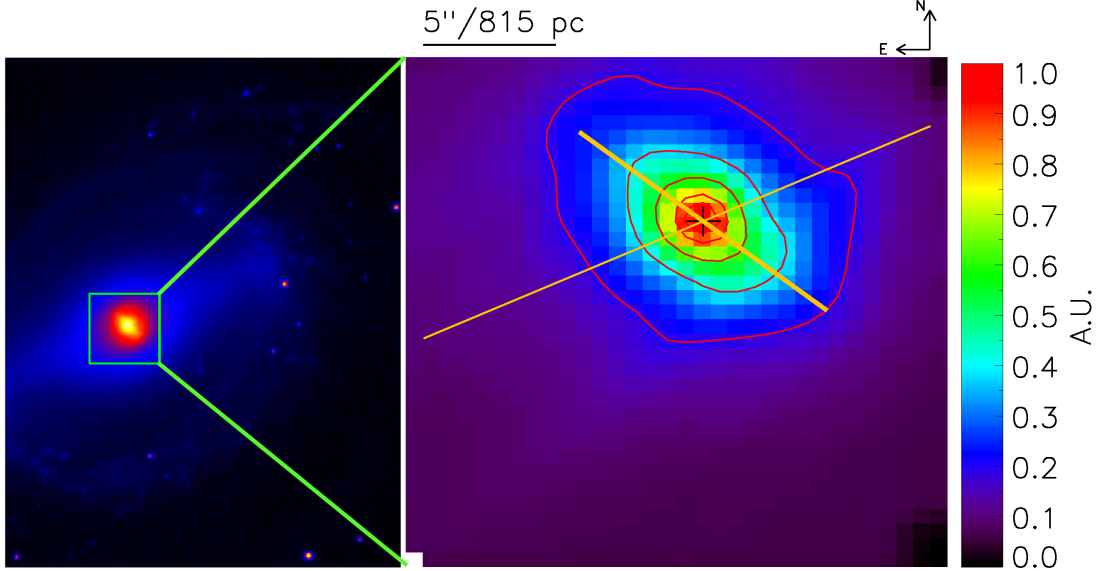


Figure 2.4: Left: SDSS r-band image of NGC 5850. Right: Continuum image of NGC 5850 from 6000 to 6100 Å zoomed in on the central $27'' \times 27''$. The flux density is given in arbitrary units (A.U.). The major axis of the primary (thin line) and the secondary bar (thick line) are overplotted. The contours are given at 20, 40, 60, 80, 90, and 95 percentage of maximum flux density. The continuum peak is marked with a black cross.

using the IRAF STSDAS ELLIPSE task¹. The locations of the projected primary and secondary bars, as taken from Lourenso et al. (2003), are overplotted in Fig. 2.4 and all subsequent maps for comparison. The continuum peak is used as the galaxy core throughout the thesis.

Figure 2.5 shows the emission line maps of the strongest emission lines. Though relatively strong in the center, the $H\alpha$ and $H\beta$ emission is more strongly peaked at $\sim 2''.1$ (~ 346 pc) southwest of the center, providing evidence of the presence of an $H\text{ II}$ -region complex. A second but faint $H\text{ II}$ -region complex can be found at a distance of $\sim 10''$ (~ 1627 pc) to the east of the center. It does not lie on the axis of the secondary bar but might be part of the circumnuclear ring.

In the emission line maps of the forbidden low ionization species ($[\text{N II}] \lambda 6585$, $[\text{S II}] \lambda\lambda 6718 + 6732$), I see that the location of the emission peak coincides with that of the

¹IRAF is distributed by the National Optical Astronomy Observatories, which are operated by the Association of Universities for Research in Astronomy, Inc., under cooperative agreement with the National Science Foundation.

continuum emission, confirming this to be the location of the galaxy’s center. Furthermore, the emission in both forbidden lines is extended along the major axis of the bar. I also note a contribution from the inner H II-region. The forbidden high ionization transition [O III] $\lambda 5008$ is mostly extended along the secondary bar.

2.3.2 Kinematics

The line of sight velocity (LOSV) maps of H α and [N II] $\lambda 6585$ are shown in Fig. 2.7. All emission lines, including those whose kinematics are not displayed here, show s-shaped isovelocity contours in the center. The nucleus is at relative rest, as expected. Areas of negative velocities are found in a ring-like structure in the east and southeast of the FOV, while positive velocities are predominantly found in the north and northwest.

To complete the kinematic picture on a larger scale, I additionally display the [N II] $\lambda 6585$ LOSV map in Fig. 2.7. It was derived *before* I subtracted the stellar continuum. Consequently, this map has not been subject to any clipping for fitting quality reasons. The values are consistent with the H α velocities and do not deviate much from those of [N II] $\lambda 6858$ that are derived *after* the subtraction of the stellar continuum, since [N II] is only weakly affected by the stellar population.

In the inner 3'' of NGC 5850, the LOSV field is characterized by a positive and negative velocity peak. These peaks are located almost symmetrically with respect to the galaxy center. The negative peak southwest of the center and the positive peak in the northeast of the center have almost the same absolute velocity and lie on a straight line through the center. I estimate the position angle to be $\text{P.A.}_{\text{kin,ion}} \approx 25^\circ$. Consequently, the kinematic major axis is tilted with respect to the major axis of the secondary bar ($\text{P.A.}_{\text{secondary}} \approx 49.3^\circ$; Lourenso et al. (2003)). Furthermore, the velocity peaks do not have the same distance to the center.

In most pixels, the [N II] $\lambda 6585$ emission line is the strongest line in our spectra. Since it is contaminated by but corrected for a weak sky line, I prefer to show the H α velocity dispersion map in Fig. 2.7. After the correction for the instrumental resolution, the H α velocity dispersion map is characterized by regions of medium to high dispersion that coincide with strong velocity gradients. The high dispersion areas are aligned approximately in the north-south direction, extending over but not peaked on the center.

2. NGC 5850

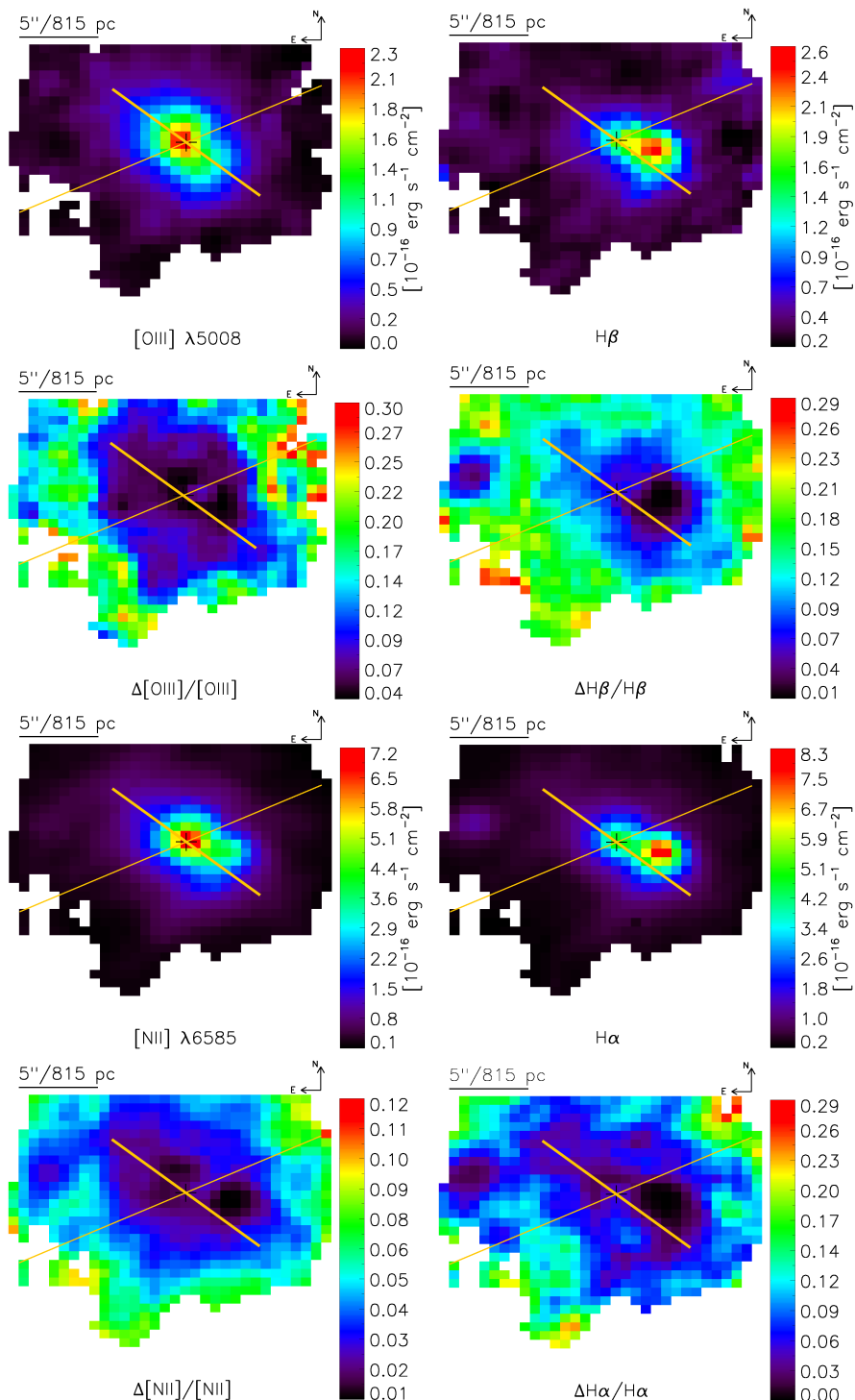


Figure 2.5: The first and the third row show the emission line maps of the indicated species. The second and the fourth row show the according relative error maps. In all images, the cross denotes the center of the continuum peak. The major axis of the primary (thin line) and the secondary bar (thick line) are overplotted.

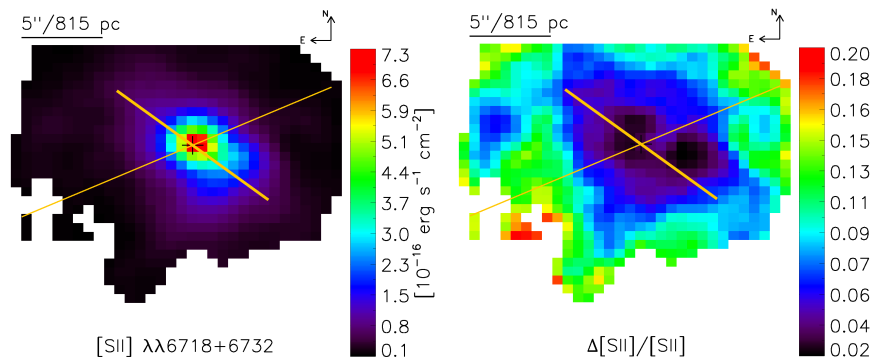


Figure 2.6: The same as in Fig. 2.5 but for [S II].

I notice the spatial coincidence of increased LOSV dispersion and strong LOSV gradients. This is a symptom of beam smearing. To evaluate the influence of this effect, I calculated the average dispersion value in the FOV ($\approx 65 \text{ km s}^{-1}$) and compared it with the dispersion peak values ($95 - 105 \text{ km s}^{-1}$). From this, I estimate the dispersion of the potentially unresolved component of about 70 to 80 km s^{-1} . This value is similar to the observed LOSV differences in seeing elements on both sides of areas with increased dispersion values. Hence, the increase in line width might be dominated by the change in LOSV within a seeing element, and it appears likely that I are observing gas at different velocities within one spatial element.

The H II emission regions have the lowest dispersion in the whole map with $\sim 30 \text{ km s}^{-1}$ as is expected for star-forming regions (e.g., Wisnioski et al., 2012). After a close inspection of all emission lines, I find asymmetries in their shape. They show blue line wings south of the core. The wing moves to the red flank of the line, while the emission is traced to the north of the center. As a global multicomponent fit is too uncertain, I only show example spectra for the regions, where the lines show the strongest asymmetries. These example regions and the fits to their respective emission line shapes are plotted in Fig. 2.8, and the fit results are reported in Table 2.1.

The stellar LOSV dispersion map in the right panel of Fig. 2.9 is a byproduct of the STARLIGHT code used to subtract the stellar contribution to the galaxy spectrum. The spatial distribution and the values of the dispersions agree with Moiseev et al. (2004) and de Lorenzo-Cáceres et al. (2008). Furthermore, I can confirm the detection of the σ -hollows at the edges of the secondary bar, which were observed by de Lorenzo-Cáceres et al. (2008).

2. NGC 5850

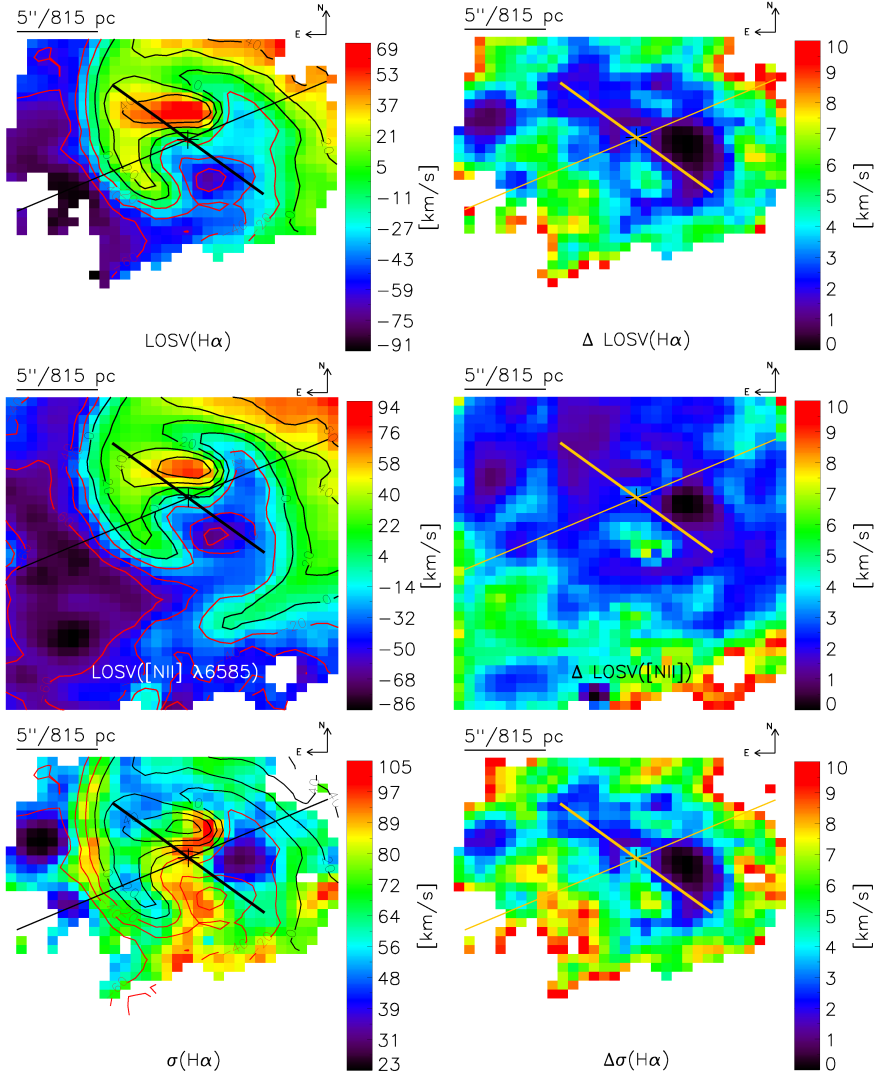


Figure 2.7: (Left column top): $H\alpha$ line of sight velocity maps with overplotted major axis of the primary (thin line) and the secondary bar (thick line). The contours mark the velocities -60 , -40 , -20 , 0 , 20 , and 40 km s^{-1} . Contours of negative velocities are red. (Left column center): $[\text{N II}] \lambda 6585$ line of sight velocity map. It has been derived *before* the subtraction of the stellar continuum and clipping of spaxels according to the criteria outlined in the text. Both velocity maps show the same morphology. (Left column right): $H\alpha$ velocity dispersion map corrected for instrumental resolution. The isovelocity contours of $H\alpha$ line emission are overplotted. (Right column): The error maps corresponding to the maps in the left column.

Table 2.1: Results of the double Gaussian emission line-fit attempts for regions with strong line asymmetry.

Location	Emission line	Fit component	v [km s ⁻¹]	σ [km s ⁻¹]	Flux [10 ⁻¹⁶ erg s ⁻¹ cm ⁻²]
north	H β	main	11	55	0.5
		2 nd	200	33	0.2
	[O III] λ 5008	main	10	57	0.3
		2 nd	76	134	0.5
	[N II] λ 6549	main	3	28	0.6
		2 nd	143	26	0.1
	H α	main	-44	43	0.6
		2 nd	66	93	1.0
	[N II] λ 6585	main	-25	52	1.2
		2 nd	124	68	0.9
south	H β	main	-18	110	0.5
		2 nd	-259	-	-
	[O III] λ 5008	main	-11	132	0.7
		2 nd	-268	76	0.1
	[N II] λ 6549	main	10	21	0.4
		2 nd	-92	72	0.2
	H α	main	2	52	0.5
		2 nd	-118	90	0.5
	[N II] λ 6585	main	-24	73	1.3
		2 nd	-158	50	0.1

2. NGC 5850

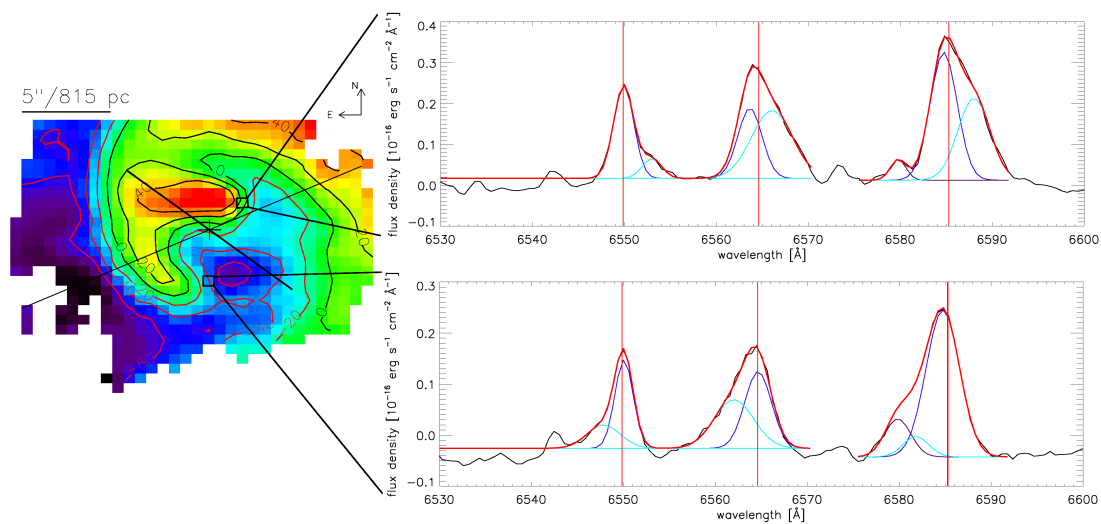


Figure 2.8: $H\alpha$ line of sight-velocity map (left) as in Fig. 2.7. On the right hand side, I display the red grating spectra of the regions highlighted by black boxes in the velocity map. The different components of the attempted line fits are plotted in the spectra as well. In red, the overall fit is displayed. The third (and left-most) fitting component in the $[\text{N II}] \lambda 6585$ emission line is the fit on the sky line contamination. The fitting results are reported in Table 2.1. The vertical red lines denote the rest wavelength of the emission line.

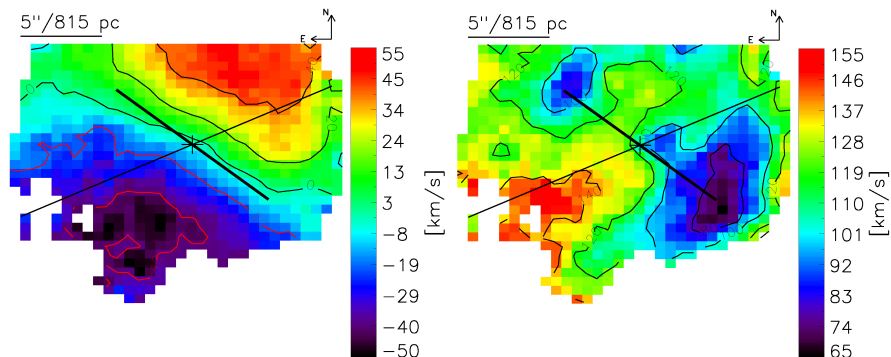


Figure 2.9: Stellar kinematic maps derived by STARLIGHT. The major axis of the primary (thin line) and the secondary bar (thick line) are overplotted. Left: Stellar line of sight velocity map with overplotted isovelocity contours at -40, -20 (red), 0, 20, 40 (black) km s^{-1} . Right: Stellar velocity dispersion map.

The stellar LOSV map derived by STARLIGHT in the left panel of Fig. 2.9 is very regular. It hardly deviates from the spider diagram typical of circular rotation. The influence of the secondary bar is negligible. This also can be seen in Fig. A7 in [de Lorenzo-Cáceres et al. \(2008\)](#) with a general agreement in the velocity values.

2.3.3 Excitation

Maps of the observed line ratios in NGC 5850 are shown in Fig. 2.10. The highest line ratios are consistent with a LINER classification. The LINER emission is not confined to the location of the continuum peak but extended. In the $\log([\text{N II}]/\text{H}\alpha)$ map, the high line ratios extend mainly from the center to the northeast with additional components to the northwest of the core's location and to the south. In this map (Fig. 2.10 middle top), I denoted several regions of interest, where I stacked the spectra in a 3×3 spaxel aperture for further analysis. The first region is directly at the location of the continuum peak (region A). The second one (B) is the inner H II-region. With (C), I denoted an area nearby and northwards of the center, showing a strong velocity gradient (see Fig. 2.7). The region in the northwestern extension of the LINER field close to the tip of the secondary bar is marked with (D). The H II-region in the far east of the FOV is marked with (E). In $\log([\text{S II}]/\text{H}\alpha)$, the map (right panel of Fig. 2.10) shows a dominant peak on the galaxy core, but high line ratios are also found south of the center (region F). The center of the galaxy does not coincide with the line ratio

2. NGC 5850

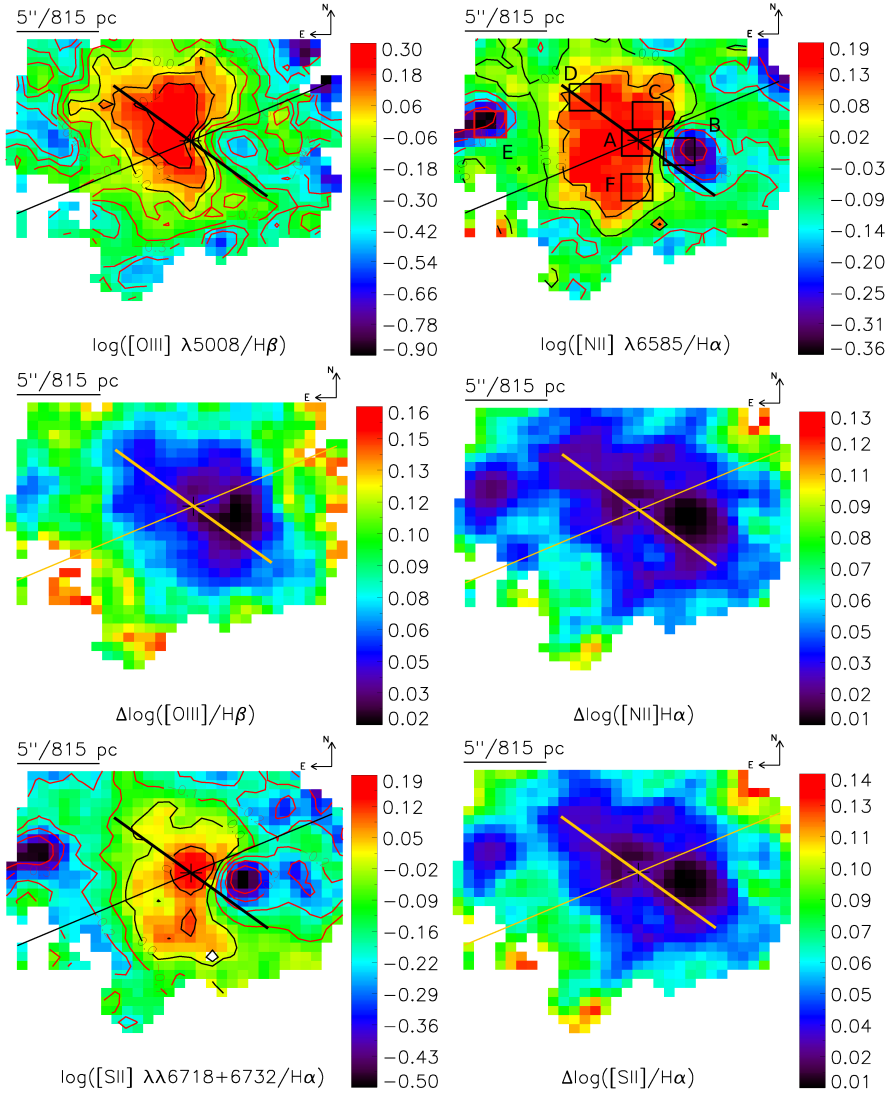


Figure 2.10: Left column: Logarithmic line ratio maps of lines used for diagnostic diagrams. Black (red) contours mark regions of positive (negative) logarithmic line ratios. For the explanation of the denoted regions see text in Sect. 2.3.3. Right column: The error maps corresponding to the maps in the upper row. In all panels, the major axis of the primary (thin line) and the secondary bar (thick line) are overlotted.

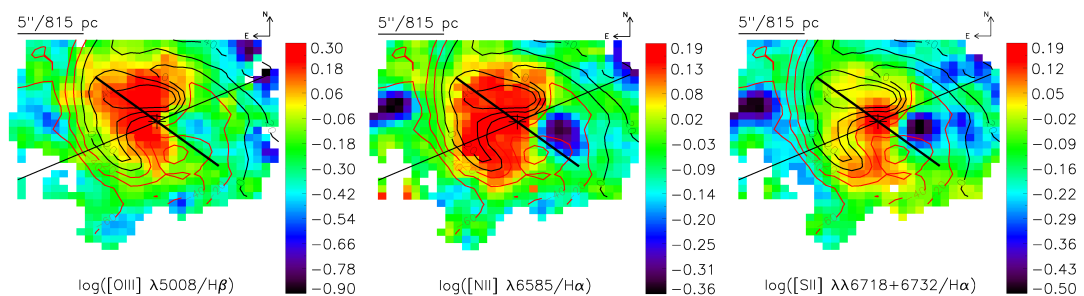


Figure 2.11: Map of logarithmic line ratios with overplotted $H\alpha$ line of sight velocity contours as in Fig. 2.7. The high line ratios are largely confined by steep velocity gradients. The major axis of the primary (thin line) and the secondary bar (thick line) are overplotted.

peak in the $\log ([\text{O III}] / H\beta)$ map (left panel of Fig. 2.10). This is likely a contrast effect induced by the $H\text{ II}$ -region, because the $[\text{O III}]$ peak clearly coincides spatially with the continuum peak. Nevertheless, the center has an elevated value consistent with the classification as LINER.

Comparison of the shape of the $\log ([\text{N II}] / H\alpha)$ map with the $H\alpha$ LOSV (left panel of Fig. 2.11) shows that the high emission line ratios largely follow the steep velocity gradients. In $\log ([\text{S II}] / H\alpha)$, the spatial coincidence of the high values and the strong velocity gradients are only prominent in the center and south of it (see right panel of Fig. 2.11).

I note further the tail of lower line ratios indicated in all maps by the contours in Fig. 2.10. They start at the inner $H\text{ II}$ -region and are oriented radially outwards to the west. The average line ratios corresponding to the apertures indicated in Fig. 2.10 are plotted in the diagnostic diagrams of Fig. 2.13 with the line ratio of each individual pixel.

Figure 2.13 confirms the LINER nature of the core region A and of regions C, D, and F. In addition to the demarcation lines by [Kauffmann et al. \(2003\)](#) and [Kewley et al. \(2001, 2006\)](#), I added a mixture line to evaluate the LINER influence on the inner $H\text{ II}$ -region and the FOV (see Sec 2.4.2). The line was calculated as the linear combination of line ratio fractions of the inner SF-region and the LINER core (each from an aperture of 3×3 pixels), i.e.,

$$\left(\frac{[\text{O III}]}{H\beta} \right)_{\text{mix}} = x \times \left(\frac{[\text{O III}]}{H\beta} \right)_{\text{SF}} + y \times \left(\frac{[\text{O III}]}{H\beta} \right)_{\text{LINER}},$$

2. NGC 5850

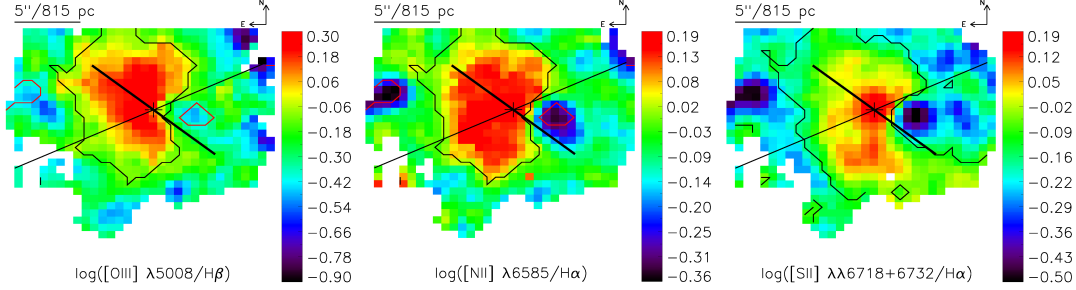


Figure 2.12: Line ratio maps overplotted with classification contours and the major axis of the primary (thin line) and the secondary bar (thick line). Left and center: Areas surrounded by the black contour line correspond to AGN-like ionization. Areas enclosed by the red contour line contain regions classified as star forming. Other regions are dominated by composite-type line ratios. The classification was made according to the diagnostic diagram, the extreme starburst demarcation line of [Kewley et al. \(2001\)](#), and the pure star-formation demarcation line of [Kauffmann et al. \(2003\)](#). Right: Areas encircled by the black contour line are classified as LINER-like within the $\log ([S II] / H\alpha)$ diagnostic diagram using the LINER-Seyfert demarcation line of [Kewley et al. \(2006\)](#) and the extreme starburst line.

where $x + y = 1$ and $x = 0.01, 0.02, \dots, 0.99$. The average spectra of both H II-regions, B and E, are very close to the demarcation line that separates the SF classification from the composite one. However, they are not classified as SF, but the apertures comprise SF classified pixels. It is also interesting to note that the remaining parts of the FOV are dominated by composite type spectra.

2.4 Discussion

2.4.1 Composite emission

In NGC 5850, I observe spatially extended regions with spectra containing narrow emission lines, which are not purely originating in the photoionization by an AGN. Large continuous parts of the FOV are classed as composite, as shown in Fig. 2.12. Within the diagnostic diagram in Fig. 2.13, the composite region is significantly populated and forms a sequence that connects the H II-regions with the LINER-regions. With the line ratio maps, this might indicate that the importance of sources capable of producing LINER-like emission increases with decreasing distance to the center. The mixing line in the $\log ([O III] / H\beta)$ vs. $\log ([S II] / H\alpha)$ diagram, which is introduced in Sect. 2.3.3 and

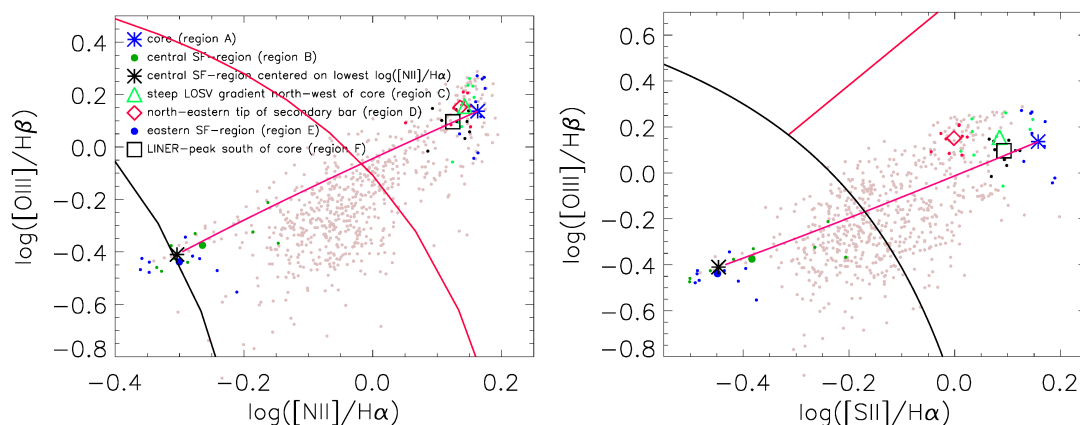


Figure 2.13: Diagnostic diagrams: The gray dots mark the positions in the diagnostic diagrams of spaxel for which I have all necessary line measurements. The big colored symbols mark areas in the FOV, consisting of stacked spectra of 3 by 3 spaxels. The small colored dots are the corresponding single spectra of which the average spectrum of a region was calculated. Medium blue asterisk: core region (A); dark green filled circle: central H II-region centered on spaxel with brightest H α emission (B); black asterisk: central H II-region centered on spaxel with lowest $\log([\text{N II}]/\text{H}\alpha)$ (B); light green triangle: steep velocity gradient area northwest of core (C); red square: northeastern LINER-region close to tip of secondary bar (D); dark blue filled circle: eastern H II-region (E); and black square: LINER peak south of core (F). The solid magenta line is the SF-AGN mixture line, as explained in the text. Left: $\log([\text{O III}] \lambda 5008 / \text{H}\beta)$ vs. $\log([\text{N II}] \lambda 6585 / \text{H}\alpha)$ with the extreme starburst line of Kewley et al. (2001) overplotted in red and the pure star formation line of Kauffmann et al. (2003) in black. Right: $\log([\text{O III}] \lambda 5008 / \text{H}\beta)$ vs. $\log([\text{S II}] \lambda\lambda 6718 + 6732 / \text{H}\alpha)$ with the LINER-Seyfert demarcation line of Kewley et al. (2006) in red and the extreme starburst line in black.

2. NGC 5850

connects the classification of the core (blue asterisk) with the strongest SF-like spectrum of the inner H II-region (black asterisk), confirms the hypothesis that the bulk of the gas in the FOV is ionized by a mixture of SF and a mechanism that produces LINER-like spectra. However, the mixing line in the $\log[\text{O III}]/\text{H}\beta$ vs. $\log[\text{N II}]/\text{H}\alpha$ diagram is located at the upper edge of the point cloud. The proximity of the central H II-region to the nucleus leads to an increase of the ionization parameter of the SF-region and lifts its position within the diagnostic diagram into the composite area. This effect might appear overpronounced by the extent of the point-cloud toward low $[\text{O III}]/\text{H}\beta$ values. Some of these spaxels have relatively high uncertainties in $[\text{O III}]$, indicating the line measurement to be close to the 3σ detection limit. These spaxels are commonly outside the KDC, as can be seen in the $\log([\text{O III}]/\text{H}\beta)$ -error map (Fig. 2.10).

This would not be the first discovery of an extended narrow line region (ENLR) that is classified as composite in terms of diagnostic diagrams and that is interpreted as the result of a mixture of different ionizing sources. [Scharwächter et al. \(2011\)](#) found composite emission in the circum-nuclear region and between H II-regions in the ring of HE 2211-3903. They concluded the ionization to stem from star formation and from the AGN. [Rich et al. \(2011\)](#) shows how star formation and slow shocks resemble the composite emission of two nearby luminous infrared galaxies. The composite emission in NGC 5850 does not appear to stem from a mixture of SF and slow shocks. Given that the velocity of slow shocks is of the order of 100-200 km s⁻¹ ([Rich et al., 2011](#)) and that our observed LOSV dispersion values are mostly below this range; the contribution of shocks to the composite emission seems to be of low relevance.

2.4.2 H II regions

Within our FOV, NGC 5850 contains two SF-regions, as identified by means of diagnostic diagrams. In the following, I report their properties. In Table 2.2, I list the star-formation rates (SFR) as derived from the H α luminosity according to [Kennicutt \(1998\)](#) and [Calzetti \(2012\)](#) (see also [Leroy et al., 2012](#)) for the east and the central SF-region within a 3×3 pixels aperture. Note that the extinction correction is a source of uncertainty for the derived star formation rates. For the faint eastern H II region, the data suggest a Balmer decrement that is smaller than the case B value, and therefore, the extinction was assumed to be zero. This could be the result of inaccuracies

Table 2.2: Star-formation rates and oxygen abundances (OA) in the H II-regions of NGC 5850.

Region	SFR ^a	SFR ^b	OA ^c	OA ^d	OA ^e
	[10 ⁻³ M _⊙ /yr]	[10 ⁻³ M _⊙ /yr]	12 + log (O/H)	12 + log (O/H)	12 + log (O/H)
H II east	1.0 ± 0.1 ^f	0.7 ± 0.1 ^f	9.02 ^{+0.03} _{-0.02}	≥ 9.14	8.77 ± 0.04
H II center ^g	9.3 ± 3.7	6.5 ± 2.5	8.99 ^{+0.04} _{-0.04}	≥ 9.20	8.77 ± 0.06

Notes. The oxygen abundance (OA) is given in values for 12 + log (O/H). Details are described in the text.

(^a) calculated following Kennicutt (1998). (^b) Calculated following Calzetti (2012) assuming a Kroupa (2001) initial mass function, stellar masses in the range of 0.1 M_⊙ < M < 100 M_⊙, continuous star formation lasting for τ ≥ 6 Myr with a temperature of T_e = 10⁴ K and an electron density of n_e = 100 cm⁻³. (^c) Calculated from [O III]/Hβ. (^d) Calculated from [N II]/Hα. (^e) Calculated from O3N2. (^f) Zero extinction has been assumed. (^g) Aperture has been centered on brightest Hα spaxel.

in the choice of the stellar templates during the stellar continuum subtraction process. Another possibility could be scattering, which is not considered by the assumed dust screen model of the applied extinction law. The Hα emission in the central SF-region is affected by LINER-like photoionization, as indicated by its classification as ‘composite’ in the diagnostic diagram. This extra radiation enhances the forbidden emission line intensity stronger than the Balmer line intensity. Furthermore, it prevents us from estimating the influence of diffuse ionized gas, which can boost the Balmer emission (Blanc et al., 2009), and therefore, I might overestimate the calculated SFR. Scaling the Calzetti (2012) star-formation rate of the central SF-region to an area of 1 kpc² yields a SFR-density of Σ_{SFR} ≈ 0.06 M_⊙ yr⁻¹ kpc⁻², which is lower than the median value of 0.2 M_⊙ yr⁻¹ kpc⁻² for circumnuclear (0.2 kpc ≤ 2 kpc) SF in galaxies that are the same Hubble type and that are located at roughly the same distance (z = 0.00344 – 0.0344) (Shi et al., 2006) (see also Valencia-S. et al., 2012).

To get an impression of the nebular metallicity¹, I make use of the connection between the optical emission line ratios and 12 + log (O/H), as shown in Fig. 6 in Maiolino et al. (2008). Our work focuses on the gas present in NGC 5850. Thus, I do not use

¹In the context of nebulae, I use metallicity and oxygen abundance synonymously. However, they are not strictly the same as metallicity commonly describes the iron-to-hydrogen ratio, and the oxygen abundance is the oxygen-to-hydrogen ratio.

2. NGC 5850

the stellar metallicity (de Lorenzo-Cáceres et al., 2013) and choose the strong-lines method instead. I use $\log([\text{O III}] \lambda 5008/\text{H}\beta)$ and $\log([\text{N II}] \lambda 6585/\text{H}\alpha)$ again for the close separation between the emission lines involved. I apply the method on 3×3 pixel apertures on both H II-regions and report the results in Table 2.2. The values derived from different line ratios are not consistent with each other but they indicate the gas in both regions to be characterized by super-solar abundances with values roughly around 9, which correspond to an oxygen abundance $(\text{O}/\text{H}) \gtrsim 1.8 (\text{O}/\text{H})_{\odot}$. For comparison, the solar value is $12 + \log(\text{O}/\text{H})_{\odot} = 8.69$ (Asplund et al., 2009). Please note that the metallicity calculated from $\log([\text{O III}] \lambda 5008/\text{H}\beta)$ in Maiolino et al. (2008) is double-valued. I constrained the range of possible solutions by considering the value derived from $\log([\text{N II}] \lambda 6585/\text{H}\alpha)$. For the abundance calculated from $\log([\text{N II}] \lambda 6585/\text{H}\alpha)$, I can only give a lower limit, since our line ratios intersect the value space of the fit by Maiolino et al. (2008) only with the negative error bar. This high value is possibly the signature of a nitrogen overabundance, a feature commonly associated to AGN (e.g., Scharwächter et al., 2011).

Additionally, I calculated the oxygen abundance from

$$\text{O3N2} \equiv \log\{([\text{O III}] \lambda 5008/\text{H}\beta) / ([\text{N II}] \lambda 6585/\text{H}\beta)\}$$

(Pettini & Pagel, 2004) that yielded values of about 8.77 for both H II-regions, which are close to the solar value.

To complete the picture, I refer the reader to the results of de Lorenzo-Cáceres et al. (2013) on the stellar metallicity. They found a systematically increased value in NGC 5850 ($Z \approx 1.3 Z_{\odot}$) within the secondary bar compared to the remaining parts of the kinematically decoupled core. The central H II-region is located well within the stripe of increased metallicity of the secondary bar. The eastern H II-region, in contrast, is not positioned within the secondary bar but nevertheless shows values higher than solar in its approximate region. Due to the projected proximity of the central H II-region to the LINER-center, I expect signatures of mutual contamination of their spectra. Indeed, the outer parts of the central H II-region are diagnosed as composite and as LINER-like while approaching the galactic center (Fig. 2.10).

On the other hand, the $[\text{O III}]$ and $[\text{N II}]$ emission in the central SF-region do not appear to originate in the gas irradiated by young stars only, but it comprises the contribution of other distributed ionizing sources and/or the AGN. This becomes clear if

I look at Fig. 2.13. Though close to the pure-SF-demarcation line, harder radiation lifted the average line ratios of the inner SF-region (aperture centered on the brightest H α pixel, thick green dot in Fig. 2.13) to the composite area. Note that the aperture centered on the strongest H α pixel is slightly closer to the nucleus than the aperture centered on the lowest $\log([\text{N II}]/\text{H}\alpha)$ ratio of the central SF-region (black asterisk), but the latter is more ‘SF-like’ in the diagnostic diagrams.

The line ratios of the outer SF-region are almost coinciding with the position of the black asterisk within the diagnostic diagrams, i.e. the least core contaminated average spectrum of the central SF-region. Both show approximately the same gas abundance.

Possibly the interplay of radiation originating in the core and in the central SF-region is not only confined to the space in between them. The wedge-shaped line ratio contours in all of the three diagnostic maps (Fig. 2.10) indicate reduced line ratios radially outwards from the inner SF-region. This hints at a shielding effect, where the parts of the galaxy located behind the H II-region are protected from the LINER-like emission from the more central region. However, the wedge more likely represents an area of enhanced SF, although weaker than in the central SF-region. This wedge is unlikely caused by an extinction effect. CO is detected weakly in this area as can be seen in Fig. 2.14, where I display $\log([\text{N II}]/\text{H}\alpha)$ overplotted with CO emission contours from the NUGA observation by Leon et al. (2000). CO emission is related to the hydrogen column density which again is linked proportionally to extinction (Heiles et al., 1981; Predehl & Schmitt, 1995). The extinction map derived from the H α /H β Balmer decrement shows no extinction there. Furthermore, the emission lines used to calculate the line ratio are spectrally close to each other so that reddening effects can be neglected. Unfortunately the differences between the ‘shielded’ area and its immediate surroundings are small, so this effect disappears in the uncertainties. In the $\log([\text{O III}]/\text{S II})$ map (Fig. 2.17), this feature is much better visible, though this line ratio map might be more prone to extinction effects than the others despite our effort to correct for them. However, it is remarkable that the feature can be seen in all diagnostic maps.

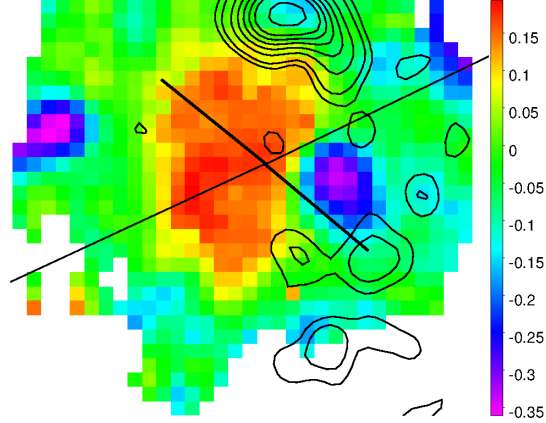


Figure 2.14: The same as in the $\log([\text{N II}]/\text{H}\alpha)$ map in Fig. 2.12, but the CO intensity contours at 0.006, 0.01, 0.02, 0.03, 0.04, 0.05, 0.06, 0.08 and 0.1 Jy/beam are additionally superimposed in black .

2.4.3 Photoionization by AGN-contribution

Generally, I confirm the classification of the nucleus of NGC 5850 to be a LINER, following the classical diagnostic diagrams. However, the extent of the LINER-like emission (Fig. 2.13) over the few central arcseconds leads to the question of whether the emission really originates in an AGN, which is a point source that is supposed to be unresolved. In this section, I examine the question of whether the gas in the central few arcseconds is photoionized by an AGN.

Extended line emission has been observed in all kinds of galaxies (see Sect. 2.1). For example, Yan & Blanton (2012) agreed on AGNs to be a possible origin. Further, they pointed out that the line surface brightness depends on the photoionizing flux profile, the gas volume filling factor, the spatial distribution of the gas clouds, and the gas density as function of distance to the point source.

In NGC 5850, one could imagine the elongated extent of the forbidden line emission could be attributed to an increased gas reservoir within the secondary bar. If there were not the central H II-region, especially in the $\log([\text{S II}] \lambda 6718 + 6732/\text{H}\alpha)$ map, the impression of the LINER-like emission elongated along the complete bar would be striking. Nevertheless, this scenario is not supported by the electron density distribution, which is roughly constant throughout the complete FOV.

In the $\log([\text{S II}] \lambda 6718 + 6732/\text{H}\alpha)$ map, the central region of increased line ratios is not so largely extended but almost unresolved. The second peak in the south of the core coincides spatially with the ‘horn’ of the velocity field, and therefore, I do not connect it to the photoionization by the putative AGN.

Surprisingly, the $\log([\text{O III}] \lambda 5008/\text{H}\beta)$ map does not peak on the center though the continuum peak position is still classified as LINER-like. Outflows are usually made responsible for such behavior (e.g. [Arribas et al., 2001](#)). The possible existence of an outflow, as discussed later in this section, would argue in favor of the single AGN model. However, the proximity of the central SF-region to the core makes a contamination of the core’s emission probable.

In general, the detection of a compact X-ray and/or radio source at the position of the nucleus is a strong evidence of the presence of an AGN ([Ho, 2008](#); [Nagar et al., 2005](#)). The faint X-ray luminosity of NGC 5850 ($L_{\text{X}}(0.5 - 3 \text{ keV}) \approx 10^{40.36} \text{ erg s}^{-1}$; [Fabbiano et al. \(1992\)](#)) suggests the nucleus to be in a state of low activity. Unfortunately, the value is integrated over a radius of $80''$, and therefore, it does not allow a statement on the compactness of the source. Further, it could comprise other X-ray emitting sources, such as supernova remnants, accreting binaries, or a hot interstellar medium ([Fabbiano et al., 1992](#)). Hence, the X-ray luminosity can only be used as an upper limit for the activity state of the nucleus, and as such, it would be consistent with luminosities expected for LINERs. Consequently, [Fabbiano et al. \(1992\)](#) considered NGC 5850 as unlikely to be AGN dominated. [Condon et al. \(2002\)](#) classified the luminosity of NGC 5850 in their radio continuum survey at 1.4 GHz as star formation driven, though one should keep the beam size of $FWHM = 45''$ here in mind as well. The beam easily comprises the central and the eastern SF-region. The beam used by [Hummel et al. \(1987\)](#) at 1.49 GHz was narrower (half power beam width = $1''3$), but the flux measurement yielded a value below the detection limit ($S_{\nu} \lesssim 0.6 \text{ mJy}$).

The bolometric luminosity of the core region can also give a hint of the presence of an AGN. I measured the extinction corrected luminosity of $[\text{O III}] \lambda 5008$ in a circular aperture of $3 \times FWHM(\text{PSF})$, corresponding to $\sim 6''.04$ in diameter. I derive from this aperture $\log(L_{[\text{O III}]}/\text{erg s}^{-1}) = 39.1$. Making use of the estimation of [Shen et al. \(2011\)](#), the bolometric luminosity is then $\log(L_{\text{bol}}/\text{erg s}^{-1}) = \log(3200 \times L_{[\text{O III}]}/\text{erg s}^{-1}) =$

2. NGC 5850

42.6, which corresponds to $L_{\text{bol}} \approx 3.7 \times 10^9 L_{\odot}$. I emphasize that this large aperture comprises parts of the central H II-region. This conversion has been derived from a sample of quasars and might not be applicable to LINER galaxies. Therefore, I include the calculation by [Netzer \(2009\)](#), who gave a conversion for Seyfert 2 and LINER 2 objects relying on both the [O III] and the H β emission lines:

$$\log(L_{\text{bol}}) = \log(L(\text{H}\beta)) + x + \max[0.0, 0.3(\log([\text{O III}] / \text{H}\beta) - 0.6)],$$

where $x = 3.75$ for galactic reddening. I calculate $\log(L_{\text{bol}}) = 42.8 \pm 0.6$. The uncertainty of the scaling relation is mentioned to be 0.3 – 0.4 dex. Here, the central H II-region also influences the calculation. Therefore, the bolometric luminosity can only be an upper limit. However, the derived value agrees with the one derived by the scaling relation of [Shen et al. \(2011\)](#), and both are within the range expected for LINER AGN ([Ho, 2008](#)).

In summary, there is no clear evidence of the presence of an AGN in NGC 5850 from X-ray and radio observations, but the calculated upper limit of bolometric luminosity cannot be used to reject the presence of an AGN either.

2.4.4 Outflows

Outflows can become apparent in the shape of ionization cones, which are elongated structures that present an increased degree of ionization. Generally, outflows can have two different origins: They are driven by either AGN or starbursts. [Sharp & Bland-Hawthorn \(2010\)](#) found that in AGN-galaxies the wind filaments are predominantly photoionized by the AGN. In starburst galaxies on the other hand, the mechanical interaction with the ISM (i.e., shocks) is made responsible for their ionization. As mentioned in Sect. 2.1, shocks can be associated with spectra showing LINER-like line emission ratios (e.g. [Dopita & Sutherland, 1995](#)). Furthermore, outflows leave a kinematic signature in the form of an increased velocity dispersion and/or additional line components with different velocities compared to the main component. [Walsh et al. \(2008\)](#) showed that outflows can have a significant impact on the kinematics of NLRs.

In NGC 5850, the spatial distribution of LINER-like emission is strongly extended, resembling a structure that could be interpreted as an ionization cone mainly oriented

along the secondary bar (Fig. 2.12). Only some regions in our velocity dispersion map show increased values, possibly due to beam smearing (Sect. 2.3.2). A wing component in the emission lines was detected north and south of the core (regions C and F) but also spatially coincided with both steep gradients and strong twists in the velocity field. I could not properly fit these wings with multicomponent fits of Gaussian profiles in the few spectra concerned. The procedure either tended to fit the continuum or encountered the parameter limits. Hence, no uncertainties could be derived. Stacking the spectra of 3×3 pixels apertures could not alleviate the problem. I display sample spectra and attempted fits in Fig. 2.8 with the derived kinematic values in Table 2.1 in Sect. 2.3.2. They show velocities up to 260 km s^{-1} , which is a common value for outflows. The LOSV and the LOSV dispersion values of different lines within one spectrum do not agree with each other. Since the spatial extent of the emission lines that show wing components is not oriented along the major axis of the LINER-like emission it is likely that they are not directly linked to each other. As discussed before, the asymmetries coincide with steep velocity gradients that point to beam smearing effects.

In the case of NGC 5850 the differentiation of a potential outflow by its ionization mechanism is problematic. Assuming the presence of a LINER-AGN, the outflow would manifest itself with LINER-like line ratios, making it indistinguishable from a starburst-driven and therefore shock-ionized wind (e.g. Arribas et al., 2001). The SF-region close to the center also makes the presence of a starburst-driven wind a viable option.

In Sect. 2.4.3, I inferred the bolometric luminosity. In combination with the Eddington luminosity, this can give us a hint on the likelihood of the presence of an outflow. To calculate the Eddington luminosity, I first derived the mass of the central black hole (M_{BH}).

I used the M- σ relation (Ferrarese & Merritt, 2000; Gebhardt et al., 2000) for the different morphologic subsamples of galaxy bulges of Gültekin et al. (2009). These subsamples do not consider the highly peculiar environment of NGC 5850 and therefore, they pose a coarse approximation at best for the black hole mass. I set a circular aperture centered on the continuum peak with a radius of $3 \times FWHM$ of the PSF ($\approx 6''$). The covered area excludes the mentioned σ -hollows (Sect. 2.3.2) but comprises the lower σ -values of the central SF-region. From the mean stellar velocity dispersion

2. NGC 5850

in that aperture, I infer $\sigma_* = (113.7 \pm 17.9) \text{ km s}^{-1}$. Hence, the mass calculates to $\log(M_{\text{BH}}/M_{\odot}) = 7.4 \pm 0.3$, using $\log(M_{\text{BH}}/M_{\odot}) = \alpha + \beta \times \log(\sigma/200 \text{ km s}^{-1})$ with $\alpha = 7.67 \pm 0.115$ and $\beta = 1.08 \pm 0.751$ from the barred subsample of [Gültekin et al. \(2009\)](#), which provided the highest value.

It is not clear yet, whether NGC 5850 has an active nucleus or not (Sect. 2.4.3). Therefore, I compare our M_{BH} value with those of 32 inactive galaxies from [Graham et al. \(2011\)](#) and the M- σ relation from [Park et al. \(2012\)](#) for local active galaxies. In the M- σ -plane of inactive galaxies, the M_{BH} of NGC 5850 is close to the regression line. The M- σ relation for local active galaxies results in $\log(M_{\text{BH}}/M_{\odot}) = (7.1 \pm 0.6)$. Hence, our values agree with both samples. I adopt the value of $\log(M_{\text{BH}}/M_{\odot}) = 7.1$ and infer consequently an Eddington luminosity of $(L_{\text{Edd}}/\text{erg s}^{-1}) = 9.6 \times 10^{44}$ and an Eddington ratio of $L_{\text{bol}}/L_{\text{Edd}} \leq 0.007^{+0.009}_{-0.006}$.

In [Ho \(2008\)](#), our Eddington ratio is above the upper end of the distribution amongst LINER-galaxies. Furthermore, there is a non-zero probability for the existence of an outflow ([Ho, 2008](#)) with a luminosity just below 1 % of L_{Edd} . Besides their polar disk scenario, [Moiseev et al. \(2004\)](#) also speculated on an outflow. [Masegosa et al. \(2011\)](#) classed 42 % of their sample of 36 LINERs as outflow candidates. Interestingly, they found a slight trend. Their classification of the galaxy center morphologies from core-halo (i.e., unresolved point source) via outflow to disk systems appears to be accompanied by a decrease in Eddington ratio. Ratios on the order of 10^{-3} are all core-halo classified. For NGC 5850, I derive a similar value.

Another indication of the presence of an outflow is the blueshift of the absorbed sodium doublet (Na D) (e.g. [Martin, 2005](#); [Rupke et al., 2005](#)). The blueshift is the signature of interstellar gas entrained in the outflow. Figure 2.15 shows the 5000 to 6000 Å spectra taken from 3×3 spaxels apertures centered on the different regions described in Fig. 2.10. The proper subtraction of the stellar fraction in Na D is of high importance to examine the absorption due to the interstellar gas. Of course, the subtraction works best on the regions, which have a higher S/N ratio. I compare the residuals of the stellar continuum subtraction in Na D with those in the purely stellar Mg b absorption and find them to be of the same order. In areas of lower S/N, the residuals are dominated by weak sky emission lines that contaminate the spectra. From this, I conclude that either a possible outflow component is not sufficiently significant

to be detected in our data or NGC 5850 lacks the interstellar gas necessary to show the Na D absorption feature.

Considering the asymmetric line shapes and the Eddington ratio, the presence of an outflow appears possible but is not further supported by the presence of blueshifted Na D absorption features. In any case, a possible outflow is not likely linked to the extended LINER-like emission for orientation reasons. I come back to this topic again in Sect. 2.4.6.

2.4.5 Photoionization by p-AGB stars

The photoionization of gas to LINER-like line ratios is not exclusive to AGNs, and indeed Cid Fernandes et al. (2011) pointed out that a nonnegligible number of LINER classified galaxies in the SDSS are retired or passive galaxies dominated by the old stellar population in the post-asymptotic giant branch (p-AGB).

Cid Fernandes et al. (2011) developed an alternative diagnostic diagram, which relies on the equivalent width of $H\alpha$ (from here on denoted as $EW_{H\alpha}$) instead. With this new tool, it turned out that a number of formerly LINER classified galactic nuclei seem to be retired or passive galaxies. Empirically, Cid Fernandes et al. (2010) found a demarcation threshold at $EW_{H\alpha} = 3 \text{ \AA}$, where values below represent retired galaxies. I created an $EW_{H\alpha}$ map of NGC 5850 (Fig. 2.16) to evaluate the importance of p-AGB stars as a possible ionization mechanism.

On average, $EW_{H\alpha} = (0.9 \pm 0.8) \text{ \AA}$ across the FOV. I note that only the inner H II-region shows values well above the threshold, indicating p-AGB stars are not the dominant ionization source. This agrees with our previous classification in the diagnostic diagrams, which was found to be dominated by SF. The eastern H II-region falls a little below the threshold value. In contrast to the central H II-region, the core region has $EW_{H\alpha}$ s well below 3 \AA .

I further explore the possibility of the presence of spatially distributed ionization sources (e.g. shocks, p-AGB stars, etc.). I follow the arguments of Yan & Blanton (2012), where they tested whether increasing line ratios can be a result from a central ionizing source or not. They took advantage of two relations: the sensitivity of $\log([\text{O III}] \lambda 5008 / [\text{S II}] \lambda \lambda 6718 + 6732)$ to the ionization parameter U and the electron

2. NGC 5850

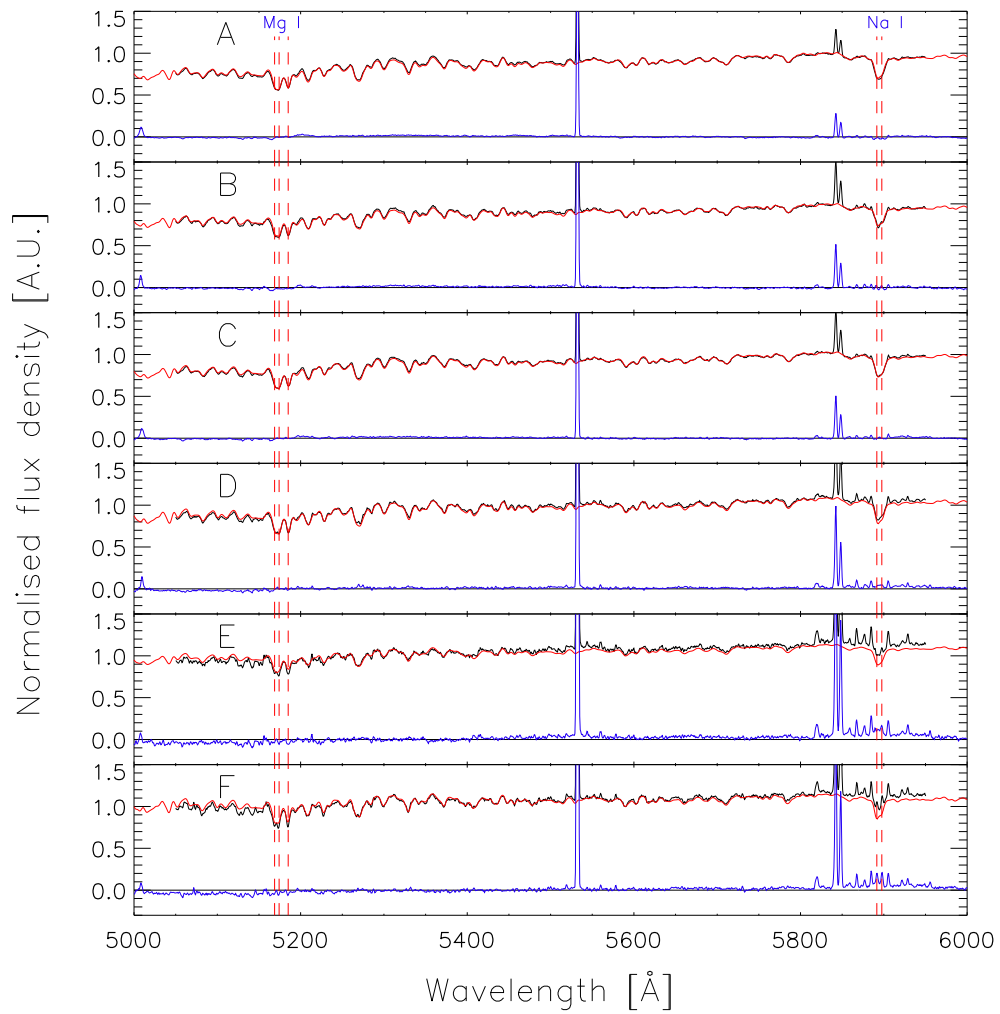


Figure 2.15: The spectra taken from 3×3 spaxels apertures centered on the regions described in Fig. 2.10. The spectra are denoted accordingly. The vertical lines mark the rest wavelengths of the Mg b and the Na D absorption features.

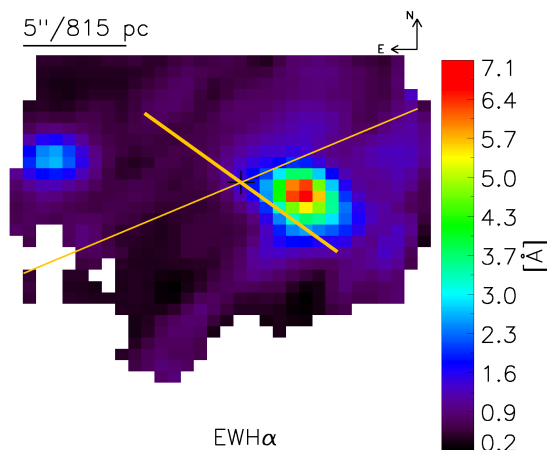


Figure 2.16: Map of the equivalent width of the H α emission line with the major axis of the primary (thin line) and the secondary bar (thick line) overplotted. The EWH α was calculated by using the emission after the subtraction of the stellar continuum. The continuum value was measured in the spectrum before the stellar population was subtracted.

density in giant ellipticals as a power law of the stellar density profile, $n_e \propto \rho_*^{1/2}$. With the gas density profile $\sim r^{-1}$, the presence of a central ionizing source, and the flux scaling with r^{-2} , they conclude the ionization parameter and the line ratio have to decrease outwards, which contrasts their observations. These findings convinced them of distributed ionization sources being dominant rather than AGNs. A similar suggestion was made by [Shields et al. \(2007\)](#), also based on ionization gradients.

The line ratios in our data as presented in Fig. 2.12 generally slightly decrease with distance to the core. In Fig. 2.17, I show the line ratio maps of $\log([\text{O III}] \lambda 5008 / [\text{S II}] \lambda \lambda 6718 + 6732)$ and $\log([\text{N II}] \lambda 6585 / [\text{S II}] \lambda \lambda 6718 + 6732)$. I note that they indeed increase with distance to the center. I calculate the ionization parameter for the 3×3 pixels aperture on the nucleus with $U = Q(\text{H}) / (4\pi r^2 n_e c)$, where $Q(\text{H})$ is the number of photons per second with an energy above the ionization energy of hydrogen, r is the distance to the nucleus, n_e corresponds to the electron density, and the light speed c is a factor used to make the ionization parameter dimensionless. If I consider that the electron density is radially almost constant within the KDC ($n_e \sim 150 \text{ cm}^3$), then U has to decrease with r^{-2} . This would result in a negative gradient of $[\text{O III}] / [\text{S II}]$ and $[\text{N II}] / [\text{S II}]$ as [Yan & Blanton \(2012\)](#) argue. This is in contrast to our observations. Consequently, U must decrease shallower or even

2. NGC 5850

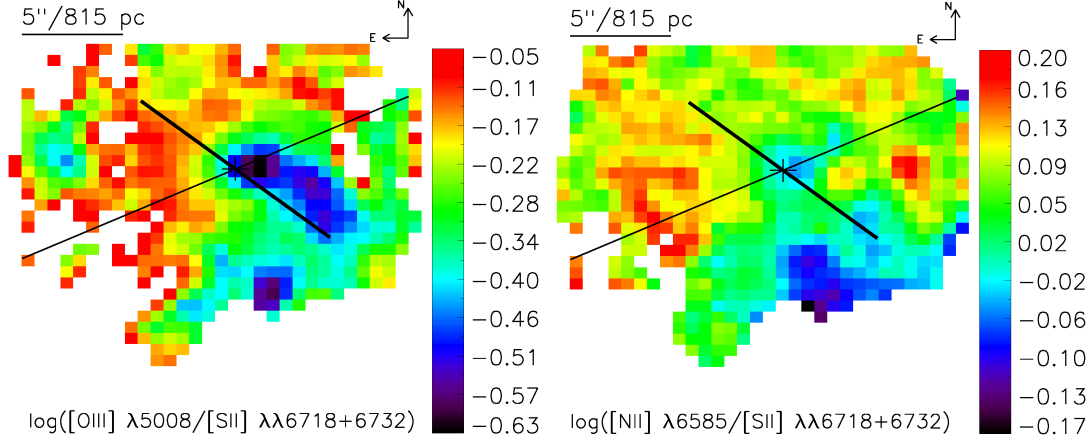


Figure 2.17: Logarithmic line ratio maps. The major axis of the primary (thin line) and the secondary bar (thick line) are overlotted.

increase with distance. This cannot be achieved by a point source but by distributed ionization sources, possibly in combination with a point source. For an overview and model calculation on the radial behavior of the ionization parameter in the presence of distributed ionization sources, I refer the reader to [Yan & Blanton \(2012\)](#).

The combination of the information on the radial behavior of U with the EWH α diagnostics make a strong case in favor of the stellar origin of ionization. A possible contribution of X-ray emitting gas to the ionization budget cannot be estimated, because there is no information on the presence of an X-ray halo around NGC 5850.

2.4.6 Kinematic scenarios

Large scale bars are believed to remove angular momentum from the interstellar medium inside co-rotation, enabling it to fall inwards until it is stopped on the inner Lindblad resonance at a distance of the order of 100 pc. The matter there can form a ring ([Friedli & Martinet, 1993](#); [Shlosman et al., 1989](#)). The gas can proceed further inwards by an inner, secondary bar formed by gravitational instabilities or galaxy encounters ([Hunt et al., 2008](#), e.g). Eventually, viscous processes could take over the transport at scales on the order of 10 pc. Viscous torques could also feed the central engine alternatively to the bar by forming a (temporary) gaseous disk that spans the complete distance from the nuclear ring to the SMBH ([García-Burillo et al., 2005](#)). Simulations by [Hopkins & Quataert \(2010\)](#) showed that lopsidedness ($m = 1$ mode) in the galaxy's gas distri-

bution in the inner few pc could also support the flow to the center. The existence of the secondary bar in NGC 5850 has been shown by isophotal analysis in several papers (see Sect. 2.1). I ask then: Is the kinematic impact of the secondary bar responsible for the extended LINER-like emission?

Shocks are almost always present in galaxies. The LINER-like areas northwest (region C) and south (region F) of the center could be interpreted as shock regions resulting from the kinematics of the secondary bar. This hypothesis would be supported by the steep $H\alpha$ velocity gradients. However, the LOSV dispersion of the gas appears flat and shows only a few values that would be consistent with shocks (i.e., $100 - 200 \text{ km s}^{-1}$ for slow shocks). The number distribution of the dispersion values is not bimodal and cannot give a clear hint of the presence of shocks (Rich et al., 2011).

At the northeastern tip of the inner bar (region D), $H\alpha$ shows signs of beam smearing with LOSV gradients not as steep as in the center. In this region, the sharp transition from the kinematically decoupled core (KDC) to the large scale kinematics of the galaxy takes place. Similar kinematic structures can be found at the opposite end of the secondary bar, though it is not that clear. Both features should be parts of a ring delineating the spatial limit of the core region. Observations with higher S/N ratio should show this feature more clearly.

The LOSV field of the KDC appears to be rotational with a superimposed spiral perturbation. The position angle of the LOSV field of the ionized gas is $P.A._{\text{kin,center}} \approx 25^\circ$ and thus very similar to the kinematic P.A. of HI in the core region (see Fig. 15a Higdon et al., 1998). In the outer parts of NGC 5850, the kinematic P.A. of HI is about $P.A._{\text{kin,outer}} \approx -25^\circ$, comparable to the P.A. of our stellar LOSV field (Fig. 2.9). Since the minor axis of the stellar LOSV field is almost aligned with the nuclear bar, I do not expect any perturbations due to elongated orbits. Indeed, the stellar kinematics are very regular. If the ionized gas disk inside the ring would share the same plane with the outer gas disk, then I would not expect any perturbations. What then is the origin of the perturbations in the ionized gas?

Though I have a weak SF region in the center (Sec. 2.4.2) it is unlikely to be strong enough to perturb the gas sufficiently. The presence of outflows is discussed already in Sec. 2.4.4 and could be a viable mechanism. If the outflow would be oriented along the plane of the inner disk, I would however expect a signature in the LOSV dispersion

2. NGC 5850

map with values of $\sim 200 \text{ km s}^{-1}$, which I do not observe. An outflow oriented along the nuclear bar would disturb the ring-like structure of the KDC that can be seen in the LOSV maps in Fig. 2.7 and 2.18. Therefore, the outflow has an orientation that does not allow interaction with the central disk.

The perturbation observed in the LOSV maps could be due to the ionized gas disk inside the ring being tilted with respect to the outer disk. In HI, the inclination for both gas disks is $i = 30^\circ$. With $P.A._{\text{kin,center}}$ and $P.A._{\text{kin,outer}}$, I calculate a separation of about 24° . Since both planes are close in inclination the KDC precesses very quickly toward alignment and would eventually form a counter-rotating disk with respect to the outer one. This scenario contradicts the proposed presence of a gaseous polar disk (Moiseev et al., 2004), since it requires the planes to be perpendicular to each other.

The counter-rotation might have triggered the lopsidedness ($m = 1$) observed in the HI and ^{12}CO distribution (Higdon et al., 1998; Leon et al., 2000), as simulated by García-Burillo et al. (2000b). The counter-rotation itself has its origin not only in the kinematic impact of the primary and the secondary bar but also requires a companion galaxy which drives the gas violently toward the center by tidal forces. As mentioned before, NGC 5850 experienced a high-velocity encounter with NGC 5846. The encounter might have triggered the accretion of the gas in the nuclear region, which then could have become counter-rotating. In Fig. 2.18, I present a differential LOSV image ($\text{LOSV}_{\text{GAS}} - \text{LOSV}_{\text{STELLAR}}$) to emphasize the peculiar gas motion and the kinematic distinctiveness of the KDC.

It remains open whether the bar kinematics can sufficiently excite the central few arcseconds without a strong central ionizing source. To answer this question detailed calculations of the energy balance and modelling of the kinematics is required. This is beyond the scope of this work.

2.5 Summary

I analyzed optical IFU data of the central $\sim 4 \text{ kpc}$ of NGC 5850 to examine the ionization mechanisms that cause LINER-like spectra and to assess the kinematic impact of the bar on the circumnuclear region. I found no clear indication of the presence of one single dominant ionization mechanism. Evidence of photoionization is present by distributed ionization sources, which is probably p-AGB stars. Nevertheless, the

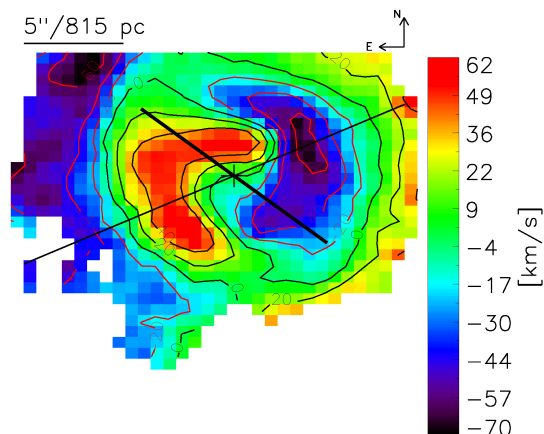


Figure 2.18: Differential LOSV map ($\text{LOSv}_{\text{GAS}} - \text{LOSv}_{\text{STELLAR}}$). The major axis of the primary (thin line) and the secondary bar (thick line) are overlotted. The isoveLOCITY contours are superimposed for 0, 20, and 40 km s^{-1} in black and for -20 , -40 , and -60 km s^{-1} in red. The spatial extent of the KDC is given by its circular structure. Within the KDC, the underlying gas disk is counter-rotating with respect to the large scale gas distribution outside of the KDC.

presence of a weak AGN and an outflow cannot be ruled out. I summarize our results as follows:

1. Although extended, the LINER-like emission is peaked on the center. Neither radio nor X-ray observations can securely confirm the presence of an AGN. Using the M - σ relation, I find $\log(M_{\text{BH}}/M_{\odot}) \approx 7.1$. Application of $L_{[\text{O III}]}$ as a proxy for L_{bol} yields the Eddington ratio to be $L_{\text{bol}}/L_{\text{Edd}} \leq 10^{-2.2}$.
2. The $\text{EWH}\alpha$ is smaller than 3 \AA throughout the areas of extended LINER-like emission, except in the central SF-region. Furthermore, $\log([\text{O III}]/[\text{S II}])$ and $\log([\text{N II}]/[\text{S II}])$ radially increase. From this, I conclude on the presence of an old (p-AGB) stellar population. However, the discrimination to X-ray emitting gas is not possible due to the lack of suitable X-ray data.
3. Almost all regions that are not classified as LINER-like show composite ionization properties, which are likely due to a mixture of photoionization by SF with those by an AGN and LINER-like ionization.
4. I confirm the presence of a kinematically decoupled core (KDC) first observed by [Leon et al. \(2000\)](#).

2. NGC 5850

5. The ionized-gas LOSV field possesses a strong spiral feature that hints at gas inflow toward the center. The perturbation is likely due to the ionized gas disk being tilted with respect to the outer disk. I calculated a tilting angle of about 24° . Both planes precess quickly toward alignment. The counter-rotation might be triggered by the lopsided gas distribution, which could be a result from the high-speed encounter with NGC 5846.
6. I found indications for the presence of an outflow extending from south to the north of the center. However, the wing components are weak and coincide with strong velocity gradients. More observations are needed to confirm this. I do not find a connection between a possible outflow and the extended LINER-like emission.
7. A starforming region close to the center (~ 346 pc) was detected showing super-solar metallicities.
8. Possible evidence of shielding of the outer ISM by the central H II-region were found. However, these decreased line ratios that form a tail oriented radially outward from the central H II-region are more likely explained by enhanced SF.
9. The detection of the σ -hollows by [de Lorenzo-Cáceres et al. \(2008\)](#) was confirmed by us.

The lack of evidence to distinguish between the ionization by an old stellar population and an X-ray emitting gas make X-ray observations with higher spatial resolution necessary. Higher resolution observations in the optical regime are necessary to disentangle the beam-smearing problem from possible intrinsically increased velocity dispersion in regions of steep velocity gradients. This could answer the question of how much shocks are involved in the matter transport within the central few hundred parsec of NGC 5850. In the future, MUSE at the VLT will provide the capabilities necessary.

Since NGC 5850 has been only weakly detected in ^{12}CO , this work shows how well optical integral field spectroscopy can complement the NUGA survey. The impact of the secondary bar on the kinematics and, consequently, on the feeding mechanisms (the matter near to NUGA's heart) are of particularly high interest. NGC 5850 certainly deserves further investigation by theoretical models, which are going to be the subject of a future work.

3

NGC 3626

At the time of writing this chapter the analysis of NGC 3626¹ has not been completed and some of the data is preliminary yet. Nevertheless, the data allows some interpretation which should not be too far from the final results.

3.1 Introduction

One of the main problems in feeding the SMBH is the removal of angular momentum of the matter so that it can approach the circumnuclear area and be eventually accreted. Mergers of galaxies can introduce gravitational perturbances that allow angular momentum to be transferred to matter located in larger distance to the center or to dissipate kinetic energy. Mergers between galaxies with comparable masses leave clear signatures in the morphology, in the star-formation activity, and in the induced nuclear activity. In contrast, mergers between galaxies with clearly different masses, so called *minor* mergers, are not that easily recognized, though they can have some morphological impact as well (Haynes et al. (2000) and references therein). For further identification of a merger of a gas rich small-mass galaxy with a normal spiral galaxy, one has to include spectral data to derive kinematic information. A common feature of these minor mergers are counterrotating gas and/or stellar disks, as observed in e.g NGC 5850 (Bremer et al., 2013) (which is not really a minor merger but a high velocity encounter; see Chapter 2), NGC 7217 (Buta et al., 1995; Merrifield & Kuijken, 1994), NGC 3626 (Cappellari et al., 2011; Ciri et al., 1995; Garcia-Burillo et al., 1998; Haynes

¹Based on observations obtained with VIMOS at ESO VLT under program ID 074.B-0257(A).

3. NGC 3626

et al., 2000; Katkov et al., 2013; Krajnović et al., 2011; Sil’chenko et al., 2010). A recent treatment in terms of numerical simulations is described in Algorry et al. (2014). The assimilation of the (smaller) companion mostly goes along with the heating of the inner disk of the bigger (primary) galaxy by the infalling matter, leading to its vertical expansion or even to its disruption. The morphology of the primary spiral galaxy after the merger is then one of an early spiral (e.g. type Sa) or a lenticular galaxy (SA0). Here, I present a preliminary investigation of the properties of such an early type spiral, which is suspected to be the result of a minor merger based on HI and optical emission line morphologies and kinematics (e.g. Ciri et al., 1995; Haynes et al., 2000).: NGC 3626.

NGC 3626 is classed in different publications either as a lenticular galaxy (R)SA0 $\hat{+}$ (rs) (de Vaucouleurs et al., 1991) or as an early spiral Sa (Sandage & Tammann, 1987), and it is unbarred. The difference in classification origins in the fact that the observed rings could also be tightly wound spiral arms observed under high inclination. Though it is a member of the X-ray bright group Leo II (NGC 3607), it is relatively isolated from the other group members which makes the interaction with them unlikely. This is supported by the fact that NGC 3626 has a regular morphology. Most prominent in NGC 3626 is its dust lane located west of the nucleus and extending from south to north (see Fig. 3.2). The central area ($R < 9''$) is characterised by the presence of a small bulge (Haynes et al., 2000). If the rings are interpreted as tightly wound spiral arms then their movement is found as trailing the stellar rotation (Ciri et al., 1995). The photometric position angle (P.A.) is mentioned to be P.A. = $(158 \pm 3)^\circ$ of the major axis and $= 67^\circ$ of the minor axis, the inclination of the galaxy is 46° (Ciri et al., 1995; Garcia-Burillo et al., 1998; Haynes et al., 2000).

NGC 3626 is well known for its peculiar gas motion. In atomic HI (Ciri et al., 1995; Garcia-Burillo et al., 1998; Haynes et al., 2000; Sil’chenko et al., 2010) as well as in molecular ^{12}CO (Garcia-Burillo et al., 1998) a disk with high gas mass of $M \sim 0.9 \times 10^9 M_\odot$ was detected and which is counterrotating with respect to the stellar population. HI is located in two concentric rings, which are spatially and kinematically separated from each other (Haynes et al., 2000). One disk can be found at a distance of $R < 60''$, the other one is characterised by low hydrogen column density N_{H} at $R \sim 190''$. The overall neutral and molecular gas kinematics is mostly simple rotational but shows some strong deviations which are interpreted as the warping of the outer

disk. Furthermore, [Haynes et al. \(2000\)](#) find a steep velocity gradient within the central $20''$. A high velocity gradient is also reported by [Garcia-Burillo et al. \(1998\)](#) who find deprojected $2430 \text{ km s}^{-1} \text{ kpc}^{-1}$ in the central $1''$ ^{12}CO gas disk. They also find ^{12}CO morphology to be somewhat different from the one of H I. While H I appears to be not present in the nucleus, in ^{12}CO a nuclear disk is observed which extends to $R = 12'' - 15''$ from the center. An outer disk is present at ($R > 20''$). Column densities are observed to be highest in the center and less high in the ring.

Also the ionised gas is observed to counterrotate with respect to the stellar population. [Haynes et al. \(2000\)](#) find H α in the center and in a ring with $R \sim 15''$. H I is spatially associated to H α but cannot be found in the nucleus. Also ^{12}CO can be found at the locations of H α ([Garcia-Burillo et al., 1998](#)). Since H α is often closely linked to star formation, it is not surprising that the gas components are found in sites of current or recent star formation. Furthermore, the kinematic properties are in agreement as well. The LOSV for ^{12}CO , H α , [N II] (the latter two found by [Ciri et al. \(1995\)](#)) are about the same (200 km s^{-1}), but deviate by $50 - 100 \text{ km s}^{-1}$ at the northwestern end of major axis of the central area. [Haynes et al. \(2000\)](#) find evidence for an H α LOSV $\sim 150 - 180 \text{ km s}^{-1}$ within the inner $5''$.

The ionised gas can also be linked to the stellar population. [Ciri et al. \(1995\)](#) note in their spectroscopic data that the gas and the stellar component have similar mean velocities ($\sim 160 \text{ km s}^{-1}$) and conclude that both obey to the same gravitational influence.

[Haynes et al. \(2000\)](#) find in their long-slit observations evidence, like double-peaked [N II] $\lambda 6585$ emission lines at $R \approx 6''$, for a possible secondary gas component that is corotating with the stars. This means, we would observe two gas populations with opposite velocities. However, [Sil'chenko et al. \(2010\)](#) point out that this configuration cannot exist in the same plane because the warm gas is a collisional system. They further conclude from the data in [Haynes et al. \(2000\)](#) that the secondary gas component does not rotate circularly with the stars in the same plane.

[Garcia-Burillo et al. \(1998\)](#) speculate on a spiral density wave in nuclear disk that could explain the signatures of the additional gas subsystems. These anomalous gas motions were accounted to strong non-circular motions like gas inflow towards the center through the mentioned spiral. Here, [Sil'chenko et al. \(2010\)](#) are sceptic again

3. NGC 3626

because there is no observable activity of the nucleus that could make an inflow velocity of $> 200 \text{ km s}^{-1}$ appear likely. However, [Garcia-Burillo et al. \(1998\)](#) refer to [van Driel et al. \(1989\)](#), whose 21 cm observations yield a spectral index of $\alpha = 1.3$ ($S_\nu \sim \nu^\alpha$), which proves the non-thermal origin of this radiation. [Ho et al. \(1997\)](#) class NGC 3626 as a possible LINER using emission line ratios. As such, this galaxy potentially harbours an AGN. It is just not clear whether the inflow continues all the way to the SMBH. The inflow could be interrupted on scales not observable with current spatial resolutions. Therefore, the observed rapid inflow does not necessarily imply nuclear activity or, vice versa, the lack of nuclear activity does not imply low inflow velocities.

It is also [Sil'chenko et al. \(2010\)](#) who find the high S/N fraction of the $[\text{O III}]\lambda 5008$ observations to resemble the counterrotating disk for $R > 8''$ and, additionally, a gaseous ring structure that is orthogonally projected at $R < 7''$. Interestingly, the remaining $[\text{O III}]$ emission of the approaching side of the ring structure coincides spatially with increased stellar velocity dispersion. The increase in dispersion is explained by the superposition of two *stellar* subsystems that differ in LOSV. The conclusion is then that the counterrotating gaseous inner ring is associated with a counterrotating stellar population. Also [Haynes et al. \(2000\)](#) treat this topic and refer to [Jore et al. \(1996\)](#), where such a configuration has been already observed in NGC 4138. In contrast, [Ciri et al. \(1995\)](#) could not find any evidence for a stellar subsystem, but they were stronger limited by their instrumental resolution.

Generally, the maximum stellar velocity dispersion is of the order of $\sigma_* \sim 200 \text{ km s}^{-1}$ and the stellar orbits are consistent with elliptical streaming. Additionally to the the large scale stellar disk, an inner stellar disk has been found by means of isopotial analysis and by kinematics ([Sil'chenko et al., 2010](#)). Together with their afore mentioned gaseous ring and based on kinematical orientation arguments the conclude on the presence of a perhaps inner gas polar ring at $R < 4''\text{--}5''$ with inclinations of $\Delta i = 58^\circ$ or 87° .

Again the stellar population is linked to the gas disk. [Sil'chenko et al. \(2010\)](#) explain that if the gas disk rotational orientation is opposite to the stellar disk, and if both are coplanar, one can refer to the numerical simulations by [Friedli & Benz \(1993\)](#), who show that the counterrotating gas will start to flow inward. The reason for this is a bar that is formed out. The gas will create a highly inclined ring close to the center as a result of resonances. Since the inner disk is oval, which is expected to remain if the

bar has dissolved again (Berentzen et al., 2006), Sil’chenko et al. (2010) suggest that the bar once existed. In a barred system the Inner Lindblad Resonance poses a natural barrier for the inflow of matter at the end of the bar. The inflowing gas forms a ring which may manifest itself in the SF-ring observed today in NGC 3626.

Further they find the main or the last period of SF to have lasted > 1 Gyr for $R < 8''$, including the nucleus and the age of the nucleus - assuming a single starburst population (SSP) - of 1–1.5 Gyr. The stellar age of the region $R < 7''$ is about 1 Gyr.

Additionally, Sil’chenko et al. (2010) detect big complexes ($\sim 6''$ north-west and south-east) with $B - V \sim 0.4$, while the small bulge in the center ($R < 9''$) is redder with $B - V \sim 0.7$. As expected, at the location of the dust lane the colors are comparable red. An area found $4'' - 5''$ north-east of the nucleus shows an age for the stellar population similar to its immediate surrounding but it turns out to be poorer in metals. Combining this information with the counterrotation of the gas they speculate this to be the remnant of the densest part of the merged galaxy, and the area with high stellar sigma would then be the "less dense stellar tail".

Different scenarios have been proposed to explain the observed properties. The first scenario was developed by Ciri et al. (1995) pointing out that gas entering another gas rich system is subject to collisions with the already present clouds of the accepting galaxy. The result is the dissipation of energy and therefore, the loss of angular momentum, leading the gas to flow inward the galaxy quickly. Further they describe that the gas should form new stars or "to evolve in complex ways". As a bottom line they consider the presence of spirals in which gas and stars move in counterrotation as unlikely. They suggest NGC 3626 to be the "evolutionary link" between the several flavours of counterrotation and that it hints on counterrotation to occur potentially in any kind of galaxy. The fact that the counterrotating gas must come from outside the observed galaxy means that the donor source has been destroyed and that its stellar population has been assimilated throughout the acceptor galaxy. Therefore, they could not observe any counterrotating stellar population, while the gas is found in a ring/disk system that evolves independently.

Garcia-Burillo et al. (1998) also describe the capture of gas from a donor galaxy. The H I gas forms the large-scale counterrotating disk. Gravitational torques lead to the loss of angular momentum making the gas move inwards to nucleus. This infall

3. NGC 3626

towards the nucleus is rapid ($t \sim 10^9$ yr). During the infall the gas is converted into H_2 by compression. Eventually it forms a disk in the inner region. They also say that any gas from the acceptor in the early merger phase fell inwards and that the resulting starburst is not visible anymore. Therefore, NGC 3626 is considered to be an old merger case.

Haynes et al. (2000) agree with that scenario. They suggest as well that the counterrotating gas could lead to star formation. However, their thoughts do not stop there, but continue the stellar evolution, concluding that the newly formed stars would create a counterrotating stellar disk, as they found indications for.

Focussing on the current star formation rather than on the past, Sil'chenko et al. (2010) suggest the rings of young stars and $H\alpha$ emission may result from the originally present corotating gas interacting with the acquired counterrotating gas. They refer to Tutukov & Fedorova (2006) for an alternative mechanism to create the ring structure. In their numerical simulations the companion galaxy moves in the equatorial plane of the acceptor galaxy in opposite direction of its rotation sense. Further, Sil'chenko et al. (2010) conclude the SF ring to expand slowly outwards.

3.2 Observations and Data Reduction

The observations have been carried out between 3 January and 17 February 2005 with the Visible Multi-Object Spectrograph (VIMOS; Le Fèvre et al. (2003)) at ESO's Very Large Telescope (VLT) unit *Melipal* in Paranal, Chile. Additionally to the blue and the red grating described in Sec. 2.2.1, the so-called orange grating was available and even mandatory. During the observations, three quadrants of the detector were equipped with the red grating, while the fourth quadrant used the orange grating. The blue (orange,red) grating covered the wavelength range from 4120 to 6217 Å (5223 – 7424 Å, 6280 – 8615 Å) with a spectral sampling of 0.54 Å (0.62 Å, 0.58 Å). The lenslets attached to the fibres have an opening angle of $0''.66$ with resulting FOV of $27'' \times 27''$ with 40×40 pixels. The observations were conducted separately for the blue and the orange-red combined grating. As for the observations of NGC 5850, three images were taken with the blue and with the orange/red grating, where the second exposure was targeted on a source free region to measure the sky emission. In total, 8 exposures for the blue and the orange/red grating each were obtained with an integration time of

3.2 Observations and Data Reduction

830 s per exposure. The data is seeing limited with the lowest DIMM seeing of $0''.79$ for the blue and $0''.92$ for the red/orange grating observations, respectively.

I made use of the VIMOS pipeline in version 2.3.3, corrected for fringing, a reflection in the flat images in quadrant 4, and performed a spatial flat-fielding, as described in Sec. 2.2.1. Also in this case the simple subtraction of the sky from the object exposures could not deliver satisfying results. However, the subtraction of a medianed sky spectrum was mostly successful. The sky emission lines are not superimposed on gas emission lines.

Since to my knowledge no suitable spectra of NGC 3626 exist, a refinement of the flux calibration of the VIMOS spectra could not be performed. Therefore, the flux values are the direct result of the VIMOS pipeline and might be subject to inaccuracies due to variabilities in the response function of the detector. The absolute flux calibration might be affected by the non-photometric observational conditions.

The science exposures were shifted and combined to a median cube for the blue and the red/orange grating each, with the red grating spectral sampling deteriorated to the orange one of 0.62 \AA . To level out severe differences in the continuum flux the spectra had to be rescaled. In areas in which spectra of the red and the orange grating were available, the red spectrum has been scaled to the orange one. Since the blue grating observations cover all quadrants, there was almost for every orange spectrum a blue grating spectrum. Therefore, the orange (and with it the red) spectrum was scaled to the blue one. Any spectral overlap between the different gratings has been replaced by the average of the two spectra. Only a fraction of the FOV is covered by the orange grating. Thus, in these regions of the detector the red spectrum could not be scaled to an orange spectrum but had to be adjusted directly to the blue. In this case a continuum region in both gratings, located close to the spectral region that separates both gratings, is used to calculate their respective continuum level. Both gratings were then scaled to the average value of the two continuum values. Though the blue grating spectra were used to flux calibrate those of the red/orange gratings, the spectra of the blue grating has not been connected to the others, in contrast to the procedure applied to NGC 5850. The concatenation of the spectra would have required the deterioration of the blue grating sampling from 0.54 \AA to the value of the orange grating (0.62 \AA).

3. NGC 3626

The loss of spectral resolution going along with it could prevent the detection of crucial information.

In any other respect, the observational data of NGC 3626 was treated as described in Sec. 2.2.1. The final FOV is $22''.5 \times 26''.3$ with the FWHM of the PSF of $\approx 2''.5$ and $2''.8$ for the blue and the orange/red grating observations, respectively. The final spectra range from $4280 - 7400 \text{ \AA}$ and have an instrumental resolution of $\sigma_{\text{blue}} = 42.3 \text{ km s}^{-1}$ and $\sigma_{\text{orange/red}} = 41.8 \text{ km s}^{-1}$.

The procedure of the stellar continuum subtraction had to be changed compared to its application on NGC 5850 (2.2.2) because the fit performed by STARLIGHT deviated from the observed spectrum in the area bluewards from 5150 \AA . As I will explain in Sec. 3.4.1, the reason for this deviation could be the presence of two kinematically distinct stellar populations. To overcome this problem, I separated the spectrum at 5150 \AA and performed the fit of the stellar population for each. Indeed, the resulting fits are more accurate but the stellar kinematic information are different for each spectral part. Since the red/orange grating spectra were never concatenated with the blue grating spectra, the fit of the stellar continuum had to be performed separately as well. Spectra to which the fit's absolute deviation was higher than 3.5% were disregarded for the scientific analysis. This threshold offered the best compromise between data quality and size of the FOV. In Fig. 3.1 I present the results of exemplary fits.

Compared to the procedure in NGC 5850, the emission line fitting with gaussian functions was slightly changed for NGC 3626. To ensure higher accuracy the three lines of the $[\text{N II}]\text{-H}\alpha$ complex were fitted together. Also the $[\text{O III}]\lambda 4960 \text{ \AA}$ and the $[\text{O III}]\lambda 5008 \text{ \AA}$ emission line were fitted simultaneously. Here I constrained the fitted width of $[\text{O III}]\lambda 4960 \text{ \AA}$ to be the same as for the $\lambda 5008 \text{ \AA}$ line.

3.3 Results

3.3.1 Morphology

In the left panel of Fig. 3.2 I show the SDSS g-band image of NGC 3626, representing the stellar continuum emission. Most noticeable is the strong dust lane surrounding the central area on its western side. The bright central region itself seems to have an elliptical shape. The superposed green square marks the FOV of the VIMOS observations,

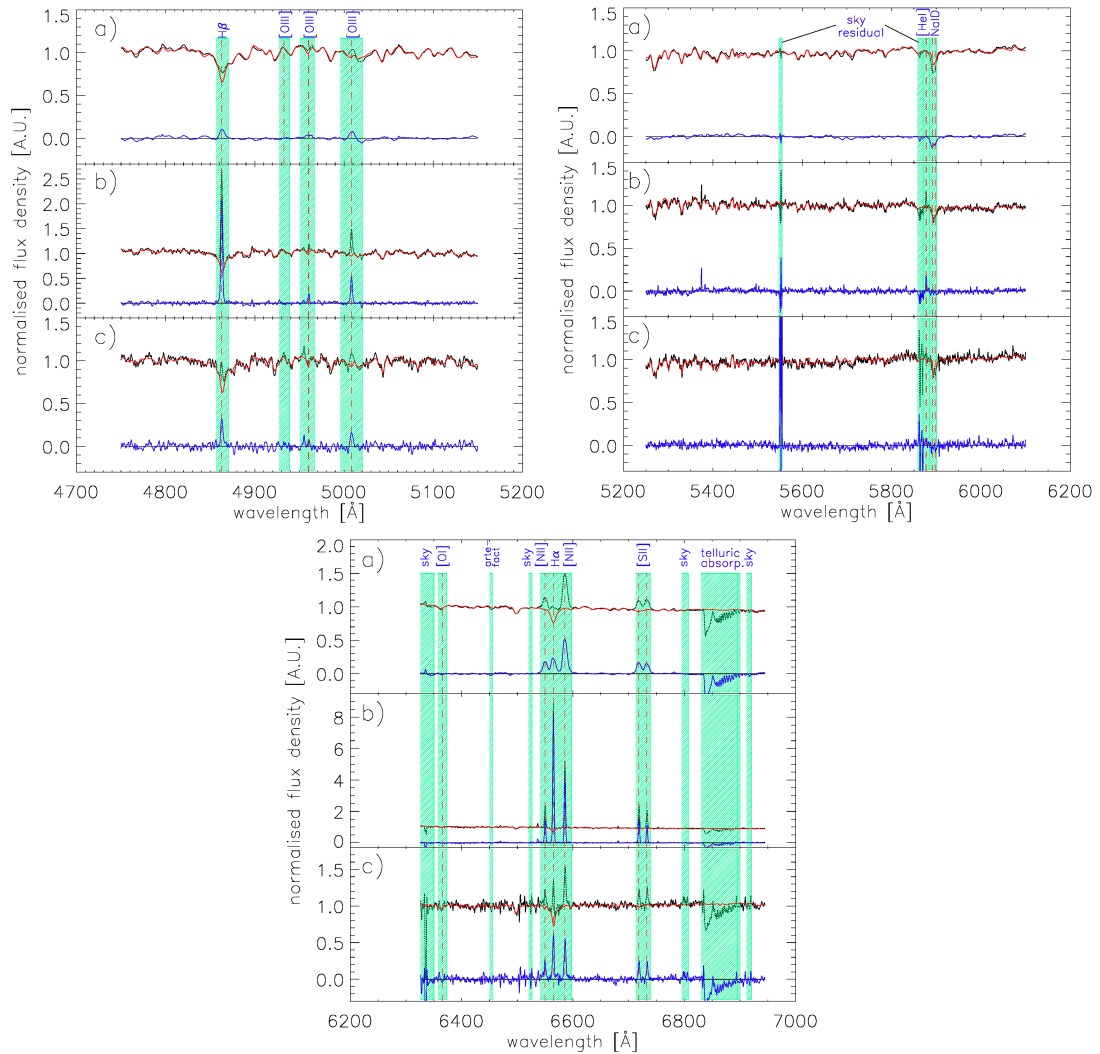


Figure 3.1: Fits with STARLIGHT of the stellar continuum in the galaxy core (a), a SF region (b), and a spaxel located in the dust band (c). The galaxy spectrum is plotted in black, the fit in red and the residual in blue. Areas marked with the green background were masked out and were not taken into account by the fitting algorithm.

3. NGC 3626

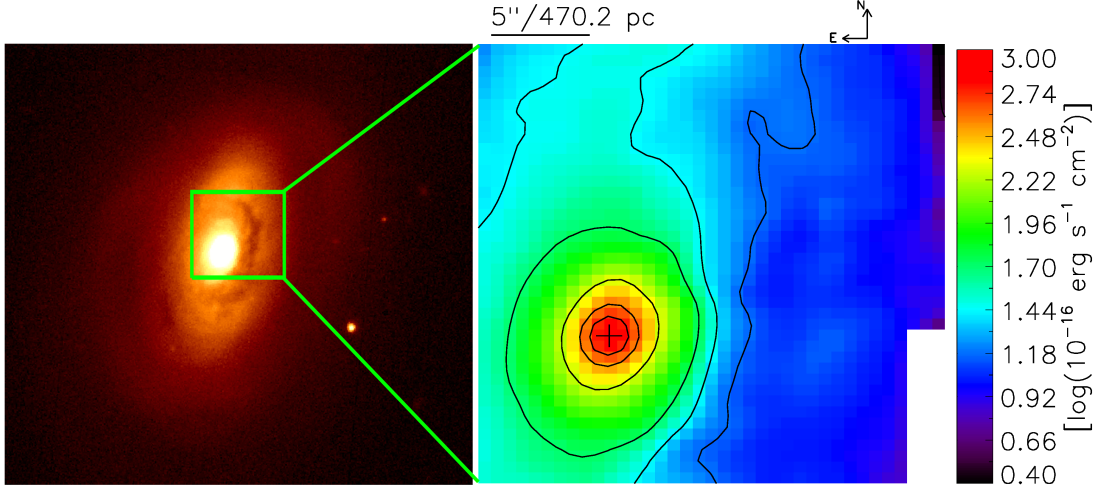


Figure 3.2: Left: SDSS g-band image of NGC 3626 in logarithmic color scale. Right: VIMOS continuum image of NGC 3626 from 6000 to 6100Å zoomed in on the central $24''.4 \times 26''.4$, also in logarithmic color scale. The contours represent 40, 50, 60, 80, 90 and 95% of the maximum logarithmic flux density. The continuum peak is marked with a black cross.

which are shown in the right panel and it covers $24''.4 \times 26''.4$. The stellar continuum peak is marked with a cross and is assumed to be the core of the galaxy throughout this work. Here, the impression of a slight ellipticity of the brightness distribution remains, but it might be artificially produced by the extinctive properties of the dust lane, which manifests itself as the low brightness area. Furthermore, the PSF of VIMOS is somewhat elliptic as well and also projection effects due to the relatively high inclination might play a role. The contour lines of the continuum emission indicate a change of the P.A. with increasing distance to the nucleus. I notice also a kink in the 40% contour line of the logarithmic flux north of the centre. It marks the northern end of the dust lane and mimics a spiral feature.

The gaseous morphology presents itself quite differently, as can be seen in Figs. 3.3 and 3.4. Though the intensities of all gas emission lines peak at the same location as the stellar continuum, they are rich in additional structure. While $H\alpha$ and $[N II]$ are dominated by a point source in the center, the other gas emission lines are clearly extended from southeast to northwest forming a bar-like structure with a projected radius of $\sim 5''$. The P.A. appears to be roughly consistent with the continuum elongation in the central region but deviates from the one further outwards. Particularly well visible in $H\alpha$ and $H\beta$, but also present in all other emission lines, is an elliptical ring of

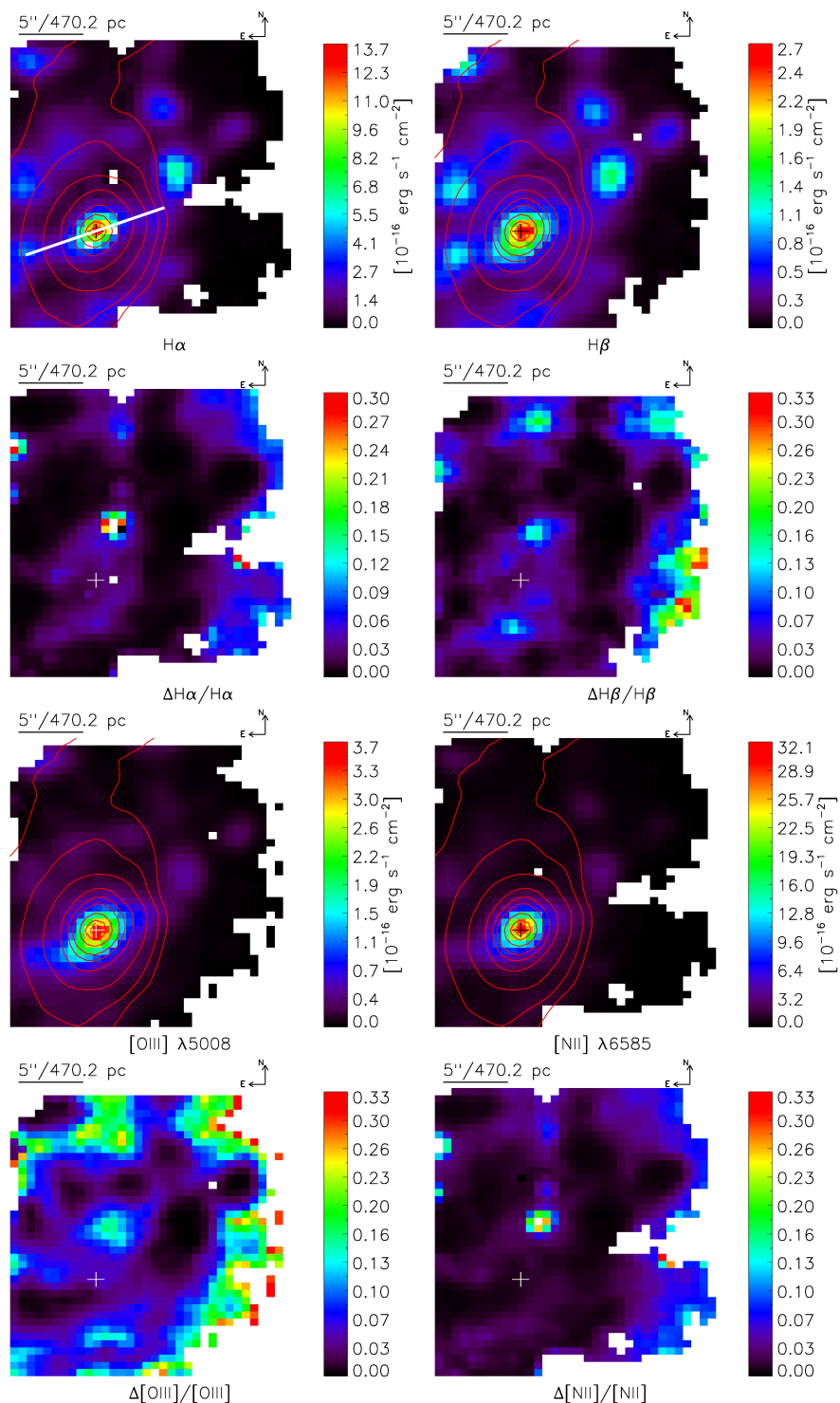


Figure 3.3: The emission line flux maps for $H\alpha$ and $H\beta$ in row 1, and $[O\text{ III}] \lambda 5008$ and $[N\text{ II}] \lambda 6585$ in row 3. Their corresponding maps of relative error are displayed in rows 2 and 4. In the emission line flux maps the contours at levels of 3, 5, 10, 20, 30, 40, 60, 80, 90, and 95 % of the peak continuum emission are superimposed. The location of the continuum peak is marked with a cross. In the $H\alpha$ emission map the P.A. ($\approx 113^\circ$) of the bar-like feature is indicated by the white bar.

3. NGC 3626

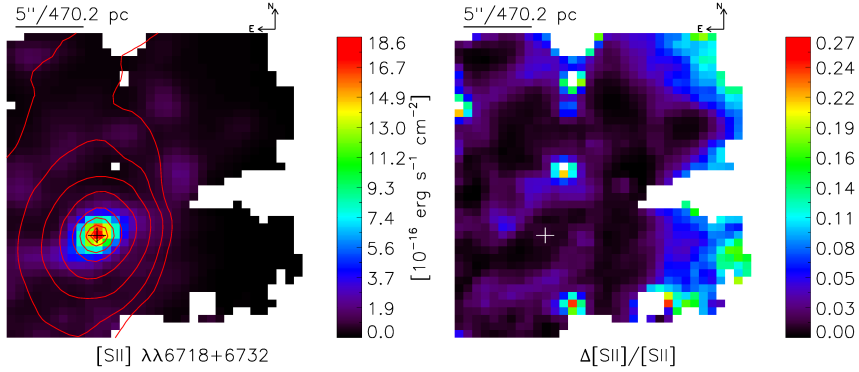


Figure 3.4: The same as in Fig. 3.3 but for the total flux of [S II] $\lambda\lambda 6718 + 6732$.

increased emission. The ring is connected to the centre by the afore mentioned bar-like feature and has a projected inner distance to the centre of $5\text{--}10''$. An H II region can be found in a distance of $8''3$ (780 pc) northwest of the centre located in the dust lane. In all the maps of relative flux error, also shown in Figs. 3.3 and 3.4, one finds an area of increased uncertainty almost north of the core at a distance of $5''2$ (490 pc). This hints to a special shape of the emission line that cannot be properly accounted for with a simple single gaussian fit. Manual inspection of the spectra reveals a double-peaked emission line profile. The more thorough treatment of this region during the emission line fit will be performed at a later stage and is not part of this work. However, it indicates this region to be of special interest. Symmetrically opposite located w.r.t. the centre, the relative flux error is also increased. This is only in H β and in [O III] recognizable. The region inside of and delineated by the ring appears to have slightly increased uncertainties as well, visible in $\Delta\text{H}\alpha$ and $\Delta\text{H}\beta$, likely due to the low flux.

3.3.2 Kinematics

The LOSV of the gas emission lines are shown in Figs. 4.4 and 3.6 and all maps are qualitatively identical. However, there are clear velocity differences in the LOSV, e.g. between H α and H β . The fit of the stellar continuum was performed separately for the blue and the red/orange grating, yielding different kinematic values. Besides the raw numbers, this error does not affect the qualitative interpretation of the LOSV maps, since it should just be a constant offset.

Most interesting in the LOSV maps is the presence of two gaseous disks, one on large scale extending beyond the FOV, and a second one at $R \lesssim 3''1$, the latter measured

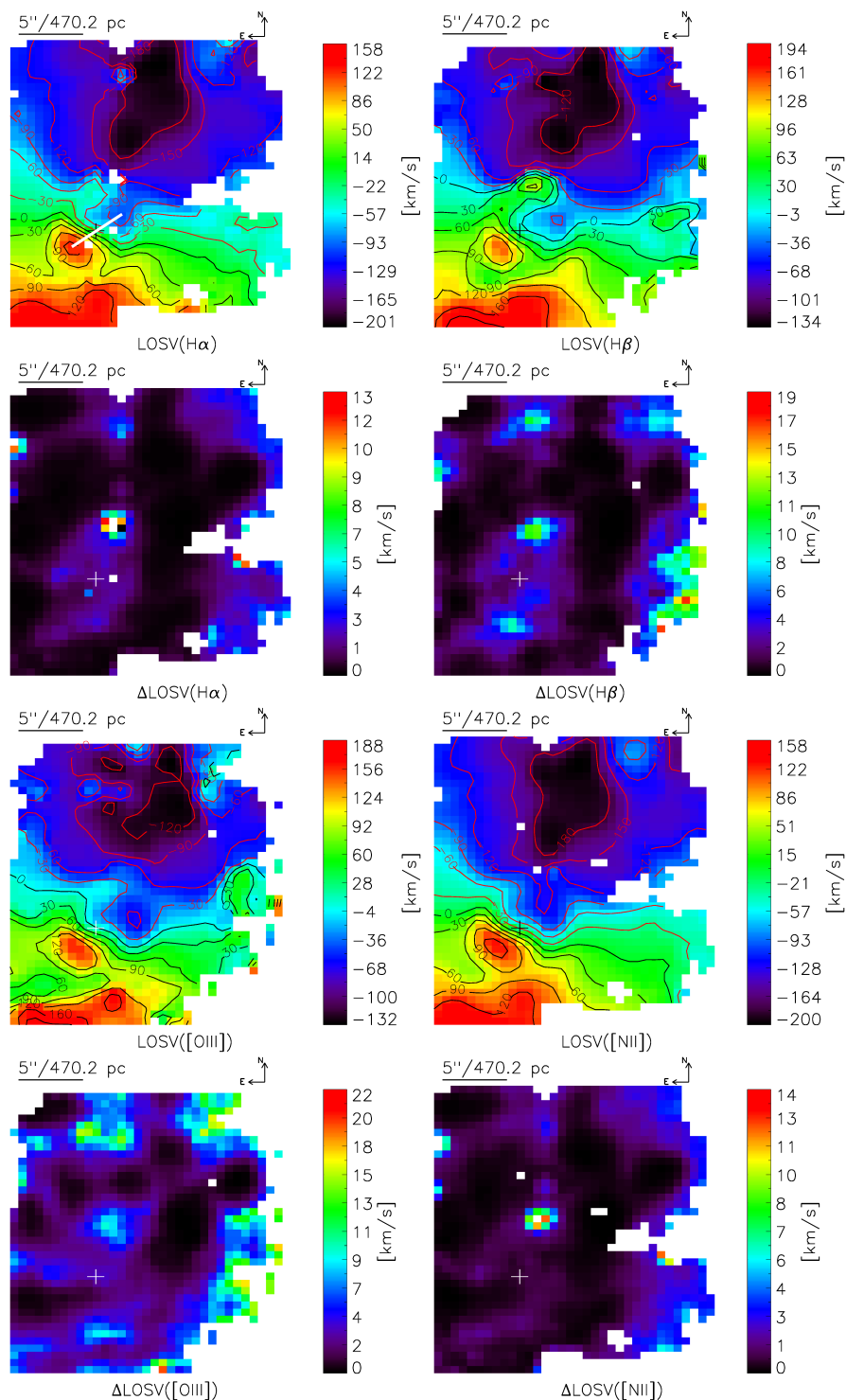


Figure 3.5: The LOS V maps of the $H\alpha$, $H\beta$, $[O\text{ III}]$, and the $[N\text{ II}]$ gas emission and their respective error maps. Blue colours represent gas approaching the observer, red colors describe receding velocities. The isovelocity contour lines are accordingly coloured and denote areas of -180 to 180 km s^{-1} in steps of 30 km s^{-1} . The cross marks the position of the stellar continuum peak. The white bar in the $H\alpha$ LOS V map denotes the P.A. of the circumnuclear disk ($\approx 125^\circ$).

3. NGC 3626

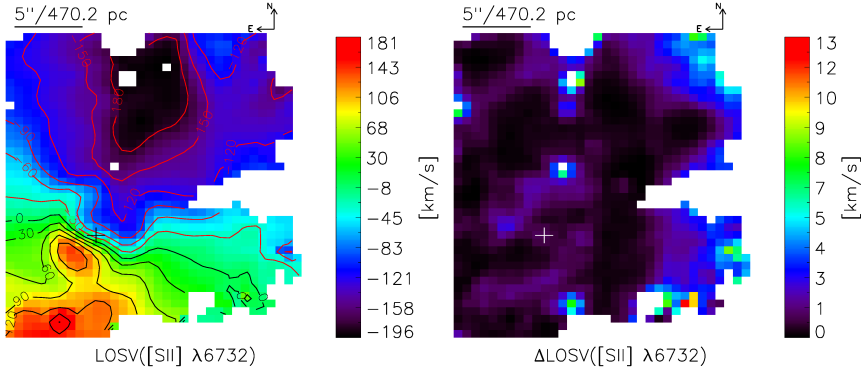


Figure 3.6: The same as in Fig. 4.4 but for the [S II] LOSV.

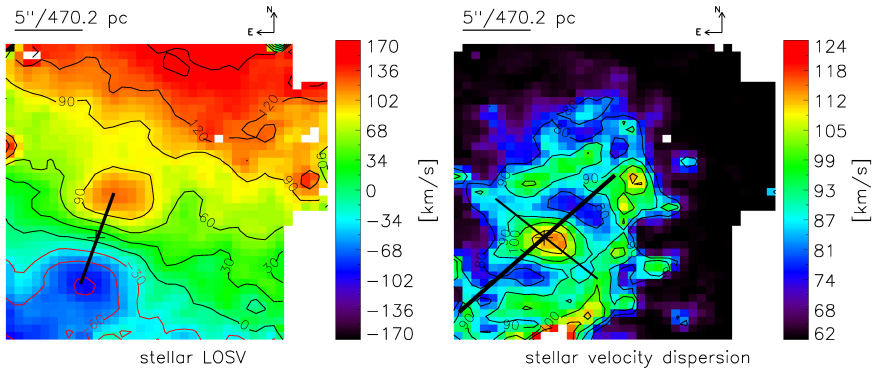


Figure 3.7: The LOSV map and the LOSV dispersion map of the stellar emission as produced by STARLIGHT. The contours are the same as in 4.4. The thick black line in the left panel represents the kinematical major axis of the circumnuclear stellar disk (P.A. $\approx 163^\circ$). In the right panel the thick (thin) line denote the major (minor) axis of the dispersion ring with a P.A. of $\approx 142^\circ$ ($\approx 52^\circ$).

from half of the distance between maximum to minimum velocity. The continuum peak is located on the kinematic major axis of the gas (P.A. $\approx 125^\circ$) within the spatial resolution. Garcia-Burillo et al. (1998) also find a nuclear disk from radio measurements (beam size: $3''.6 \times 2''.9$). They report it to have a radius of $R = 12'' - 15''$, significantly larger than I find in the ionised gas. Further, they observe strong deviations from circular motion, which I can confirm for the ionised gas from the kink in the isovelocity contours at the galaxy's centre. The *stellar* LOSV map (left panel of Fig. 3.7), a side product of the STARLIGHT code, shows evidence for the existence of stellar counterparts to the respective gaseous disks. An inner stellar disk has been identified as well by Sil'chenko et al. (2010) from isophotal analysis. The inner stellar disk is larger

($R \approx 4.3''$) than the gas disk I report here, and its major axis is P.A. $\approx 165^\circ$. Furthermore, the VIMOS data confirms [Sil'chenko et al. \(2010\)](#) who also find the ionised gas disks counterrotating w.r.t. the stellar disks. The gas LOSV increases in the area north of the centre, in which the gaussian fits are only of medium quality. The maximal H α LOSV values of $\sim 130 \text{ km s}^{-1}$ in the centre are lower than those reported for molecular ^{12}CO (240 km s^{-1} [Garcia-Burillo et al. \(1998\)](#)), but are in agreement with the measurements of H α in the inner $5''$ by [Haynes et al. \(2000\)](#).

The maps of LOSV dispersion described in the following are corrected for instrumental resolution. In all maps (Figs. 3.8 and 3.9) the maximum values spatially coincide with the galaxy centre and appear elongated from east to west. I notice that the central high σ area coincides with a steep velocity gradient. Therefore, beam smearing might be an issue and the observed dispersion does possibly not represent the intrinsic order of the observed gas motion. The only exception is H β . There σ peaks on the low-fitting quality area due to the double-peaked emission lines, which reduces the contrast in the centre. If we excluded the northern region, the σ peak in H β is also found at the centre's location. Generally, the northern region appears in all maps. South of the centre, a strong peak can be seen in [O III], and at least somewhat increased dispersion in all other maps.

Gas dispersion values higher than 60 km s^{-1} fill the area within the ring of gas emission. The ring itself can be identified by dispersions well below, typical for H II regions. In larger distance to the centre the gas LOSV dispersion seems to increase again.

Also the stellar LOSV dispersion σ_* (see right panel of Fig. 3.7) peaks in the centre and there it has an elongated morphology. The ring, identified in gas emission and in gas LOSV dispersion, can also be found by its increased σ_* . The elongated structure does not fill the ring and has a P.A. approximately perpendicular to the ring's P.A. and the P.A. of the elongated structure of the gas emission.

3.3.3 Excitation

Diagnostic diagrams ([Baldwin et al., 1981](#); [Veilleux & Osterbrock, 1987](#)) are effective tools to determine the ionisation mechanisms at work and to conclude on the dominant ionisation sources. In Fig. 3.10 I present the classical diagnostic diagrams for all spatial

3. NGC 3626

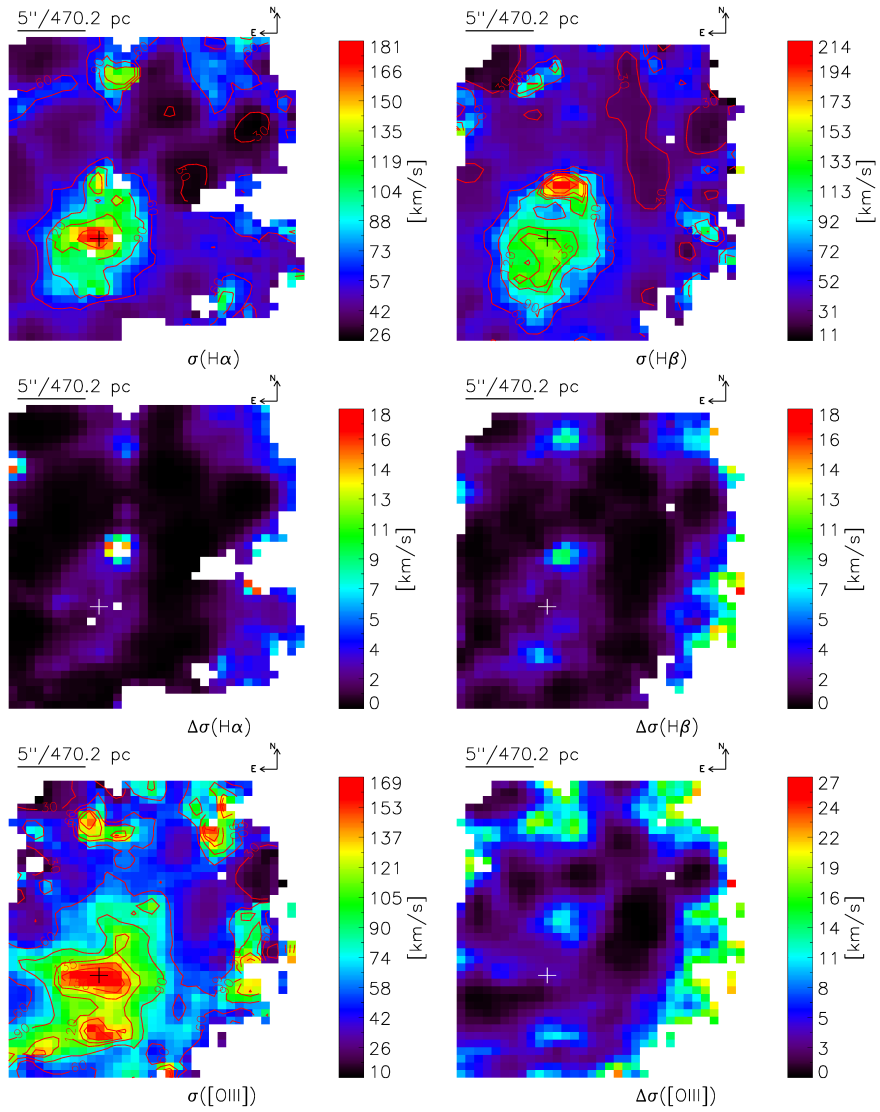


Figure 3.8: The LOSV dispersion σ of H α , H β , and [O III] λ 5008 with their respective relative error maps. The maps are corrected for instrumental resolution.

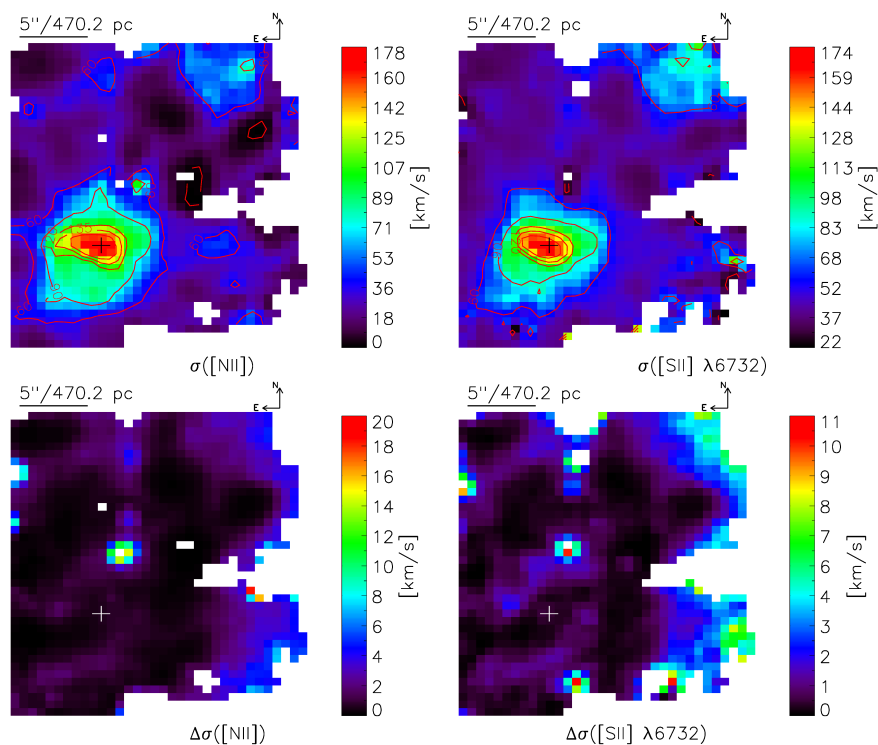


Figure 3.9: The LOSV dispersion σ of [N II] $\lambda 6585$ and [S II] $\lambda 6732$ in the upper row, and their respective error maps in the bottom row. The maps are corrected for instrumental resolution.

pixels within the VIMOS FOV of our observations for which all required emission lines could be measured.

The $\log([\text{O III}] \lambda 5008/\text{H}\beta)$ vs. $\log([\text{N II}] \lambda 6585)/\text{H}\alpha$ diagram (left panel of Fig. 3.10) is characterised by a sequence of spaxels stretching from the SF region of the graph over the composite to the AGN region. There are two peculiar issues in this plot. Firstly, all $\log([\text{O III}]/\text{H}\beta)$ are found to be < 0.2 in the Seyfert region. Secondly, despite the ring of increased Balmer emission (see first row of Fig. 3.3) only a small number of spectra are actually classed as starforming.

In all logarithmic emission line ratio maps in Fig. 3.11 the highest values are found in an elongated structure centred on the nucleus. The spectra of this area are classed to be of LINER-like nature, consistent with earlier findings (Ho et al., 1997). Also in these plots the lack of SF classed regions manifests itself, though one can clearly identify the ring by its decreased emission line ratios. Only areas close to the dust lane

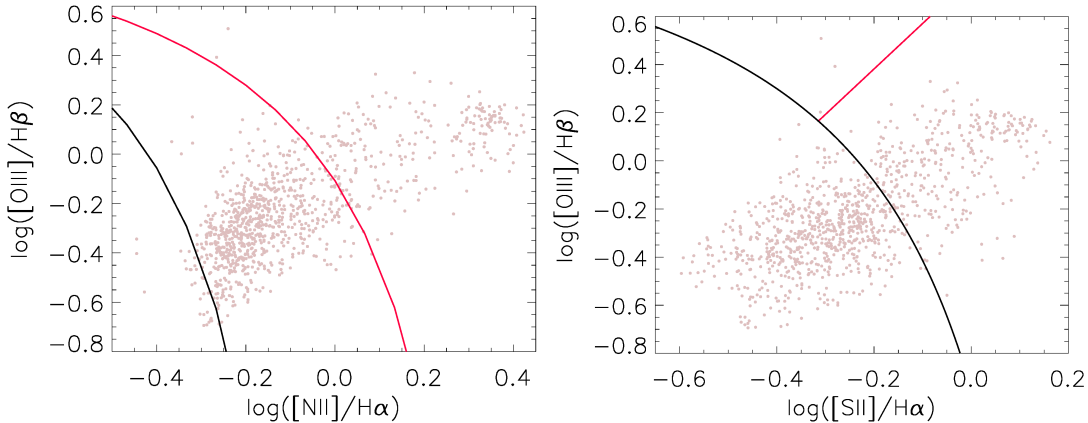


Figure 3.10: Diagnostics diagrams: The grey dots mark the positions in the diagnostic diagrams of spaxels for which all necessary line measurements are available. Left: $\log([\text{O III}] \lambda 5008/\text{H}\beta)$ vs. $\log([\text{N II}] \lambda 6585)/\text{H}\alpha$ with the extreme starburst line of [Kewley et al. \(2001\)](#) overplotted in red, and the pure star-formation line of [Kauffmann et al. \(2003\)](#) in black. Right: $\log([\text{O III}] \lambda 5008/\text{H}\beta)$ vs. $\log([\text{S II}] \lambda\lambda 6718 + 6732)/\text{H}\alpha$ with the LINER-Seyfert demarcation line of [Kewley et al. \(2006\)](#) in red and the extreme starburst line in black.

west of the nucleus are clear detections of SF-regions. Due to the spatial resolution and contrast for weak H II regions the composite classed emission of the surroundings could be mixed in. All areas not encircled by a contour line in the upper row of Fig. 3.11 are composite regions which, however, does not rule out the presence of SF. I also note the $\log([\text{O III}]/\text{H}\beta)$ ratio to peak off-core at the southeastern end of the elongation, at a distance of $5''.5$ of the centre.

3.4 Discussion

3.4.1 Stellar and Gas Disks

In the data I find several reasons to believe that at least parts of the galaxy’s stellar population are closely linked to the central gas emission.

First, the comparison of the contour lines of the stellar continuum flux with the emission of the ionised gas shows the reason for the change of the emission P.A. with distance to the nucleus. In the central $\sim 5''$ the P.A. of the gas is dominated by the bar- or spiral-like structure. Since the gas’ P.A. in the centre is approximately the same as in the stellar continuum emission, I conclude that there is a substantial stellar

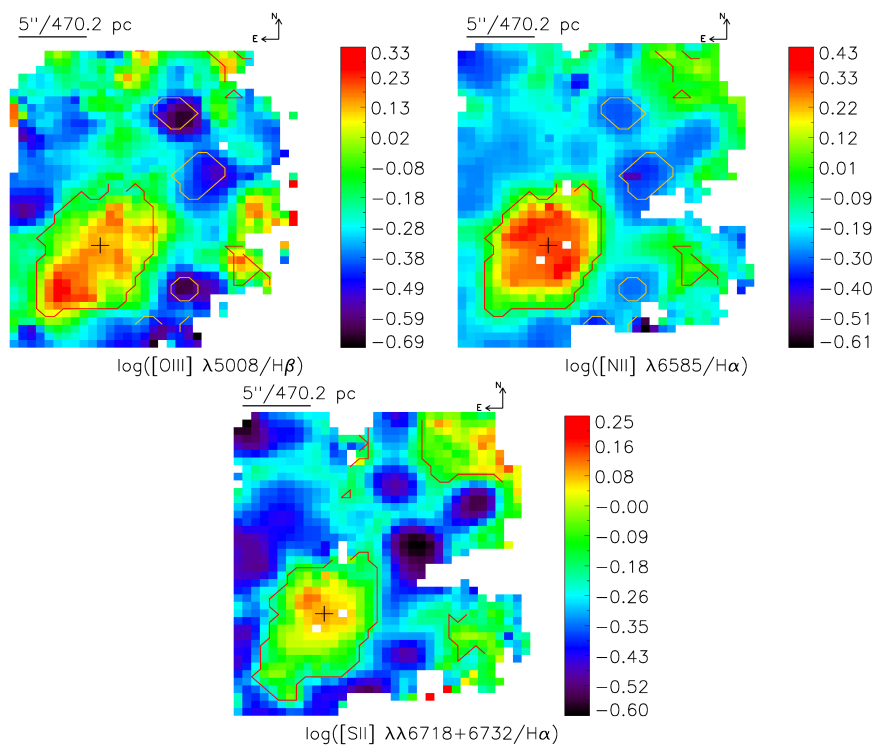


Figure 3.11: Logarithmic emission line ratio maps overplotted with classification contours. Left and centre: Areas enclosed by red (yellow) contours are classified to be in the Seyfert (starburst) region of the $\log([\text{O III}] \lambda 5008/\text{H}\beta)$ diagram. Other regions are have composite-type line ratios. Right: Areas within the red contour lines are identified to have LINER-like emission line ratio according to the $\log([\text{S II}] \lambda\lambda 6718 + 6732)/\text{H}\alpha$ diagram.

population associated with the bar structure. The P.A. of the continuum emission is approximately the same as for the gas velocity field. Though the gaseous morphology suggests a bar or spiral-like feature, in principal the observer could be deceived by a projection effect and possibly one observes an edge-on gaseous disk instead. Further outwards, yet inside the SF-ring, the emission P.A. begins to follow solely the stellar continuum.

Second, a connection between the gas distribution and the stellar kinematics is evident if I plot the Balmer emission line intensity contours over the stellar LOSV dispersion σ_* , as presented in Fig. 3.12. The σ_* distribution resembles a ring spatially aligned with the ring formed by the Balmer emission, having a P.A. of roughly 142° . Sil'chenko et al. (2010) have observed a similar structure for their $[\text{O III}]$ data. The σ_* map shows also an elongation along the minor axis of the ring ($\text{P.A.}_{\text{minor}} \approx 52^\circ$). From

3. NGC 3626

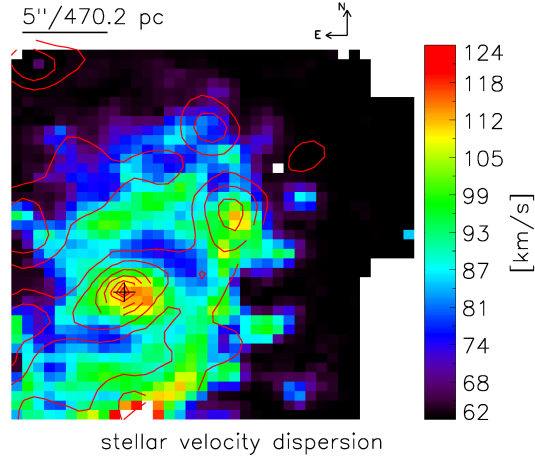


Figure 3.12: Stellar LOSV dispersion with superimposed contours of H α emission at 10, 20, 40, 60, 80, 90, and 95 % of the peak intensity.

the data it is not clear whether the stellar dispersion really resembles a ring or rather a spiral structure. Increased σ_* observe [Sil'chenko et al. \(2010\)](#) as well but not ring shaped. In their maps the northern part is weakly visible with a prominent increase of σ_* northwest of the nucleus. They speculate this to be the low density tail of the remnants of the merged dwarf galaxy. If we expand this argument to our observations then the complete ring of increased σ_* consists of low density remnants of the donor galaxy.

Counterrotating gas is frequently found in the centre of galaxies which have undergone a merger or a close encounter (e.g. [Bremer et al., 2013](#)). NGC 3626 has been suspected to be the result of a minor merger event before (see Sec. 3.1). This hints on a common extragalactic origin of the counter-rotating nuclear gas disk and the stellar population associated with it. The donor galaxy merged into NGC 3626 and left its stellar population with its own σ_* in the ring around the nucleus. If the stars have not dispersed into the already existing stellar population yet, then the LOSV difference of the two populations would result in increased LOSV dispersions ([Sil'chenko et al., 2010](#)). The difficulties I encountered during the synthesis of the stellar population could be explained by this as well. However, since we see a central stellar disk of which only the edges coincide spatially with the σ_* ring, the increased dispersion might just delineate the kinematically decoupled core (KDC). Then the central stellar disk might be composed of NGC 3626's own stellar population, or the donated and the original

population have assumed common kinematics. In this case the ring should mark the inner Lindblad resonance (ILR). To enable matter to fall further inward, bars or spirals are commonly invoked. A bar-like feature we can also see in the σ_{star} map but it is not clear whether this is the signature of a stellar bar. Usually bars are characterised by ordered motion (low dispersion).

Analogously, the ‘donated’ gas is still moving in a disk/ring around the nucleus and is forming actively stars. The accumulation of the gas in a ring is also often associated with the presence of a bar. Signs of a bar have been detected by [Laurikainen et al. \(2005\)](#) and also [Garcia-Burillo et al. \(1998\)](#) suspected the presence of a spiral density feature. In the here presented gas emission line maps the elongated structure from southeast to northwest suggests the presence of a nuclear bar or a spiral. The bar could also be interpreted as an edge-on observed gas disk. That would support the scenario of [Sil’chenko et al. \(2010\)](#) who suggest the presence of an inner polar gas ring at $R \lesssim 4''$.

The circumnuclear gas disk is smaller than the circumnuclear stellar disk and both differ in their P.A. as well. Possibly, both are not directly associated with each other.

3.4.2 The ‘Bad-Fit’ Region

A region $\sim 4''.3$ to the north of the centre attracts the attention. All gas flux error maps show increased uncertainties and the gas LOSV maps display increased values as well (see Figs. 3.3 and 4.4). In principal, an increased velocity can be the result of a badly fitted Gaussian. Indeed, the manual inspection of the spectra in this region shows strong asymmetries in the emission line shapes. Partially they are even double-peaked. This explains its high $H\beta$ LOSV dispersion (and its according uncertainties) as well. However, in the emission line maps this region remains unsuspecting. It is also noteworthy that the P.A. from the centre of the galaxy to this region is $\sim 345^\circ$, similar to the P.A. of the circumnuclear stellar disk ($165^\circ/345^\circ$). The region could be extended. In this case it would be located approximately symmetric to the high dispersion region $4''.5$ south of the nucleus. Possibly the increased dispersion values are evidence for the presence of a second gas component counterrotating w.r.t. the main component. [Sil’chenko et al. \(2010\)](#) reported colors for this region that are bluer than for in its vicinity, pointing on the presence of distinct stellar population (see also [Haynes et al., 2000](#)). In this case the subtraction of the stellar continuum might be inaccurate as well.

3. NGC 3626

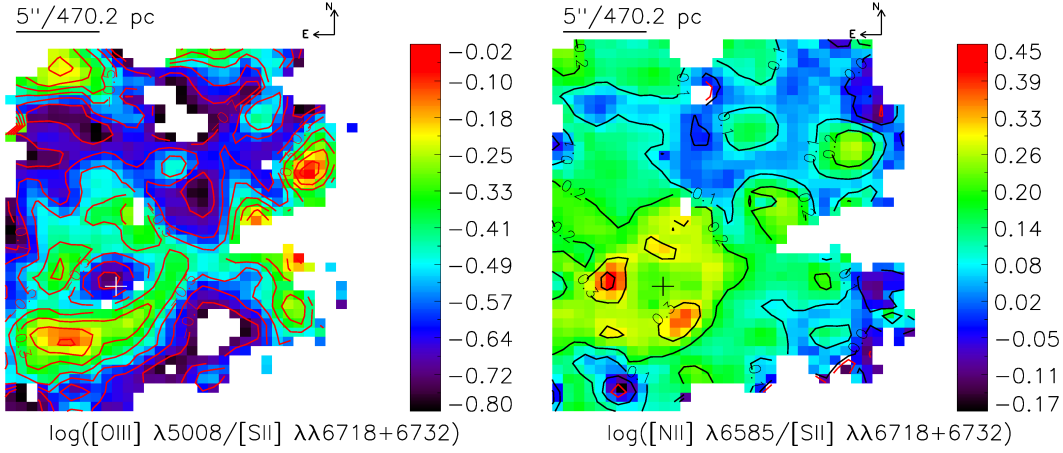


Figure 3.13: Maps of emission line ratios. Left: $\log([\text{O III}] \lambda 5008/\text{H}\beta)$. Right: $\log([\text{N II}] \lambda 6585)/\text{H}\alpha$

Part of this could be the necessity to divide the observed spectra to perform a satisfying fit of the stellar population. Be reminded that for each part of the spectrum I received different stellar LOSV and LOSV dispersions, which might reflect that different stellar populations are dominant in the different parts of the spectra. The stellar population fit should then be refined by applying the method outlined by [Coccatto et al. \(2014\)](#) who developed a method to dissect kinematically different stellar populations. Potentially, this region could be the dense remnant of the donor galaxy, maybe even its nucleus. Further examination is necessary and a multicomponent gaussian fit to the gas emission will help to shed light on this issue. This is beyond the scope of this thesis.

3.4.3 LINER-like Emission

The emission line maps in Fig. 3.3 are extended. The emission line ratio maps and their contours in Fig. 3.11 show clearly the LINER-like emission dominating the central region delineated by the ring of SF. Though extended emission line morphologies can in principal also come from a point source like an AGN, one has to consider the presence of distributed ionisation sources. Analogously to Sec. 2.4.5 and [Bremer et al. \(2013\)](#), I examine the the extinction corrected emission line ratios sensitive to the ionisation parameter (Fig. 3.13) and the equivalent width of $\text{H}\alpha$ ($\text{EWH}\alpha$).

The emission line ratios have their local minimum at the approximate position of the nucleus and increase outwards until they reach their maximum in an oval structure.

Since the ionisation parameter is a function of the gas density (approximated by the electron density), which in turn is a power-law of the stellar density ($n_e \propto \rho_*^{1/2}$) in giant ellipticals, (Yan & Blanton, 2012), an increasing ionisation parameter requires the density to decrease with distance, or to be flat. Figure 3.14 shows, that this is the case. A measurement of the electron density along the P.A. of the weakest decrease yields roughly a relation between distance and density of about $n_e \propto r^{-1}$. In other directions n_e falls off stronger. Combining these information, the ionisation parameter must increase with distance. This supports the scenario in which the dominant ionisation mechanism is not photoionisation by an AGN but is rather due to distributed ionisation sources (Yan & Blanton, 2012).

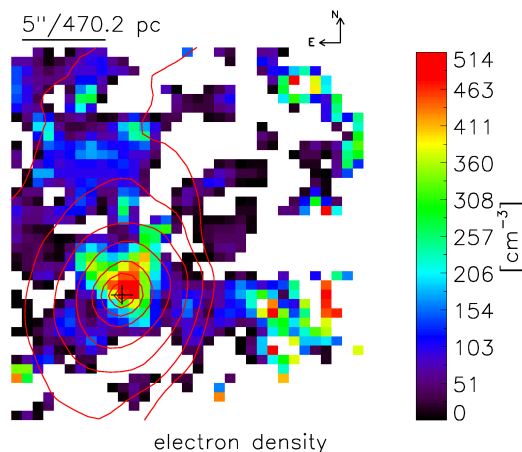


Figure 3.14: The electron density map with the same superimposed continuum contours as in Fig. 3.3.

Now, with the AGN as the dominant ionisation source being ruled out (though not dismissing the presence of a weak AGN), I can test whether the area within the SF-ring is ionised by an old and hot stellar population, namely p-AGB stars. I proceed in the same way as in Sec. 2.4.5 and examine $\text{EWH}\alpha$ (Fig. 3.15). Within the SF-ring the $\text{EWH}\alpha$ is clearly below the threshold value of 3, which identifies the galaxy to evolve passively and, in combination with the LINER-like classification, the dominant ionisation source to be p-AGB stars. However, the contribution by X-ray emitting gas and diffuse ionised gas has still to be evaluated. It is important to keep in mind that the ionisation parameter of p-AGB stars is considered to be too low and that the evolved stellar populations are poorly understood. As expected, the equivalent width

3. NGC 3626

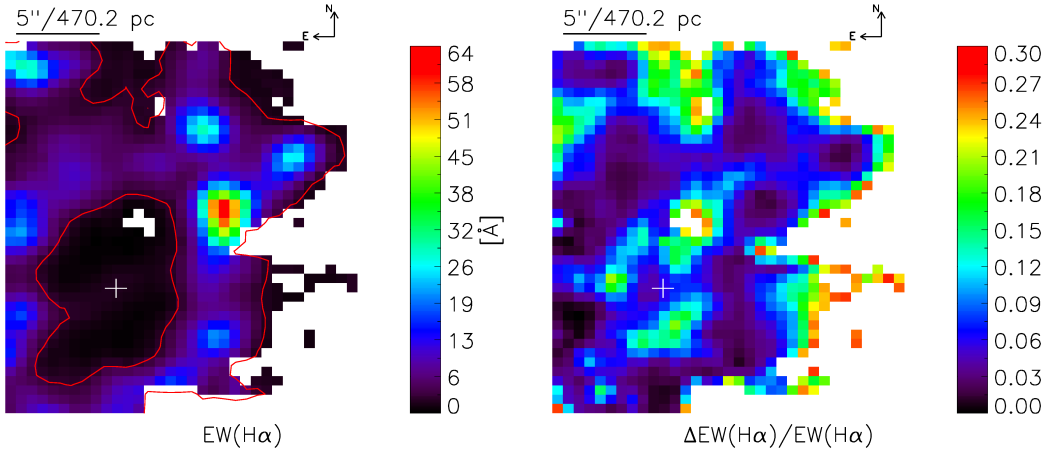


Figure 3.15: Equivalent width of $H\alpha$ (left) and its corresponding relative error map. Both maps are clipped such that the maximum relative error displayed is 0.3. The contour line delineates the area in which $EW_{H\alpha} \leq 3$.

increases strongly in the SF-ring. There are hints on the $EW_{H\alpha}$ to decrease again below 3 outside the SF-ring close to the northern and western edge of the FOV. This possibly marks the outer extension of the SF-ring and hints to the continued ionisation mostly by p-AGB stars. In this case the SF-ring would span the distance range of $5'' \lesssim r \lesssim 16''$.

In principal the LINER-like emission line ratios could also be the result of shocked gas. Slow shocks (Rich et al., 2011) require dispersions of 100 to 200 km s^{-1} , which are given for the central area inside of the SF-ring. Rich et al. (2011) show that a bimodal number distribution of the gas dispersion values can indicate the presence of shocks but this is here not the case. Furthermore, in the very centre the LOSV map is characterised by steep velocity gradients. In this case it is likely that the spatial resolution is insufficient and the emission lines are artificially broadened. Anyhow, the increase of gas dispersion towards the centre is generally expected since the temperatures are high and gas motion is stronger influenced by nuclear outflows and central SF.

3.5 Conclusions

I have studied optical IFS data focused on the central $22''.5 \times 26''.3$ of NGC 3626. I find two corotating stellar and two corotating gaseous disks, where the gas disks are

counter-rotating w.r.t. the stellar disks. All disks have different P.A.s. The orientation of the circumnuclear gas disk differs from the circumnuclear *stellar* one and also their extension is not the same. A ring of SF with $5'' \lesssim r \lesssim 16''$ can be observed in Balmer emission lines and in emission line ratio maps. Further, I find regions, which can be identified by increased gas dispersion values, and/or increased emission line ratios north, northeast, and south of the nucleus, located within the area delineated by the SF-ring. The here used single component gaussian fits to the emission lines are due to the partially asymmetric or even double-peaked line structures. This supports the observations by Haynes et al. (2000), who interpreted it as a second gas component having the opposite sense of rotation w.r.t. the first gas component. However, I agree with Sil'chenko et al. (2010) who argue that both components cannot be coplanar because the gas components form a collisional system. Consequently they must have different inclinations to remain intact. The opposite rotation of the component cannot be confirmed because of the inadequacy of a single component Gaussian fit. A more thorough assessment of this issue is necessary but is not part of this work.

The spectra of the complete area within the SF-ring are classed as LINER-like in terms of diagnostic diagrams and the ionisation is probably caused predominantly by p-AGB stars. In distances to the nucleus outwards of the SF-ring I see indications that p-AGB stars are responsible for the gas ionisation. However, this transition from SF to LINER-like region is close to the border of the FOV.

Since I see the possibility for the presence of two kinematically different stellar populations superimposed on each other, the densest part of the donor galaxy can potentially still exist. From Lick index analysis Sil'chenko et al. (2010) speculated the remnant of the core of the donor galaxy to be located in a region $\sim 5''$ northeast of the nucleus of NGC 3626. An area northwest with increased stellar LOSV dispersion they interpreted as the low density tails. According to the VIMOS σ_* map the low density tail forms almost a complete ring, located at the inner edge of the SF-ring. Interestingly, the σ_* ring is interrupted where they find a local peak in $H\beta$ absorption-line index in direct vicinity to the bluest area in their (B-V) color map.

3. NGC 3626

The SF-ring in the galaxy, possibly surrounded by gas ionised by p-AGB stars (within the FOV), is likely the result of the merger due to the interaction of the existing gas with the infalling and counterrotating gas of the donor. The rejuvenation of early-type galaxies from matter ejected by p-AGB stars is a possible scenario as well (Temi et al., 2009) but appears unlikely in the light of the merger. The bar-like feature in the centre could point to a mechanisms that removes angular momentum from the gas in the SF-ring enabling it to move inwards and eventually to feed the central SMBH. However, in the kinematical maps I do not see any hint on the presence of a bar. The gas LOSV map in the central few arcseconds are rather consistent with a disk seen edge-on. This would support the idea of Sil'chenko et al. (2010) that a polar disk might be present. The literature shows NGC 3626 (Sec. 3.1) as a nice example for minor mergers and their impact on gas and stellar kinematics, and its influence on the stellar population. Here, like in most mergers, it likely triggered a phase of star formation after the gaseous and the stellar content of the dwarf galaxy has been transported towards the central region by gravitational torques (Garcia-Burillo et al., 1998).

The work on the VIMOS data of NGC 3626 is not concluded yet. The hints on the presence of a second stellar population, that is kinematically distinct from the other, are strong. E.g. Coccato et al. (2014) show for their objects how the stellar continuum can be fit while the different populations are disentangled. Succeeding in doing so harbours exciting new possibilities. The spatial distribution of the potentially donated stars could give insight into the trajectory of the dwarf galaxy during the merger. Its stellar kinematics can show us their current interaction with the gravitational potential of the acceptor galaxy's nucleus as well as with the ionised gas. In Sec. 3.4.1 I already show some stellar features that are linked to the gas or vice versa.

The ionised gas emission lines has been fitted only with a single component gaussian. However, I see clear indications for line asymmetries, which either indicate the presence of outflows or multiple gas components. Here again, we likely observe components of the donator and the acceptor galaxy which provides us with a wealth of information that might help us to understand better the nature of mergers.

4

NGC 3627

4.1 Introduction

Interactions can be an effective mean to remove angular momentum and to provide the central area of a galaxy with gas. Therefore, it is straight forward to have a look at groups of galaxies, which have a comparably high probability of mutual influence. In this section I examine NGC 3627 which is such a group galaxy. The work I present in this chapter, is preliminary and poses the actual status of the ongoing analysis of the data.

The Leo Triplet, consisting of the galaxies NGC 3623, NGC3627, and NGC 3628, has been extensively studied for the well known interactions between its group members. Especially the observed tail and the bridge extending from NGC 3628 and the distortion in NGC 3627, visible in HI, are impressive (de Mello et al., 2012; Haynes et al., 1979) and might be a result of an encounter of NGC 3627 with NGC 3628. An optical counterpart of this feature has been reported by Kormendy & Bahcall (1974). Also model calculations by (Rots, 1978) support the interaction scenario of these two galaxies about 800 Myrs in the past. Further evidence for the interaction has been found by Soida et al. (2001) in their polarised radio measurements who mention a much steeper emission gradient on one side of NGC 3627 compared to the opposite side, and the compression of the ISM in the western side. Another evidence of interaction are the indications of synchronous evolution of both galaxies, which likely triggered a starburst phase (Duan, 2006). Most authors focused on the more obvious interaction

4. NGC 3627

between NGC 3627 and NGC 3628 but [Duan \(2006\)](#) found also evidence for NGC 3623 influencing NGC 3627 and vice versa. [Weżgowiec et al. \(2012\)](#) report the necessity of a more recent event than the encounter with one of the other galaxies in the Leo Triplet, and suggested a collision with a dwarf galaxy. Then the debris of this collision, possibly the nucleus, shows itself in the ^{12}CO LOSV map ([Reuter et al., 1996](#)).

The overall optical morphology of NGC 3627 is classed as SAB(s)b ([de Vaucouleurs et al., 1991](#)), a late-type spiral, with an inclination of $52^\circ\text{--}65^\circ$ and a P.A. of 175° (e.g. [Casasola et al., 2011](#); [Mazzalay et al., 2013](#); [Watanabe et al., 2011](#)). Its two spiral arms are asymmetric w.r.t. the major axis in IR, FUV, and ^{12}CO ([Casasola et al., 2011](#)), another indication for interactions with other galaxies. In the following I focus on the central $24''.4 \times 27''.0$ of NGC 3627. The spiral arms emerge at the end of a stellar bar and extend from $r \sim 9''\text{--}16''$. The bar has an orientation of P.A. = -21° , derived by [Casasola et al. \(2011\)](#) from 2 Micron All Sky Survey (2MASS) data. From this they conclude on the CO gas leading the stellar bar. The ends of the bar are locations of intense star formation ([Smith et al., 1994](#)). A small stellar bar ($r \sim 0.2\text{kpc}$), nested in the former one and offset by 45° , has been reported by [Haan et al. \(2009\)](#). The CO gas forms a bar-like structure with radius of $\sim 9''$ and a P.A. = $14^\circ \pm 2^\circ$ (see also [Watanabe et al., 2011](#), and references therein). This structure is located with in the inner elongated ring observed in the FUV by GALEX and in HI and which is reported to coincide with the ultraharmonic resonance ([Chemin et al., 2003](#); [Haan et al., 2009](#)). Inside this ring no or only little UV emission is detected. From NIR IFU observations with SINFONI [Mazzalay et al. \(2013\)](#) conclude on a possible box/peanut structure of the bar (boxy isophotes and slightly offset spurs in the outer part of the bar), which has vertically buckled. Generally, their NIR H_2 emission follows the CO distribution from [Casasola et al. \(2011\)](#) very well on larger scales. They also observe the bar-like structure with $r \sim 9''$ with P.A. $\simeq 14 - 15^\circ$, which is clearly different from the stellar bar P.A. = 161° . [Dumas et al. \(2007\)](#) find the ionised gas in this area to be tilted in opposite direction: P.A. = 152° . In their H_2 data, [Mazzalay et al. \(2013\)](#) can resolve the [Casasola et al. \(2011\)](#) bar-like structure into an elongated nuclear structure and two 'hot-spots' $6.5''$ northeast and $4.5''$ southwest from the center with P.A. $\simeq 17^\circ$, where the P.A. changes from $\sim 10 - 15^\circ$. at $\approx 8''$ to $\sim 0^\circ$ for $R < 3''$. Rounder isophotes in the central $5''$ are considered as evidence for the central component being more axissymmetric, e.g. (pseudo-)bulge. Circumnuclear dust lanes are oriented along

the elongated nuclear structure, which find Casasola et al. (2011) in the FIR to be warmer than around the bar. They ascribe it to recent SF in the bar. It is also this dust band, located 3'' northeast of the nucleus, from which they conclude the eastern side of the galaxy to be the near side (see also Duan, 2006). They also find an increase in dust emission at the location of the nucleus and the end of the bar, co-located with the ^{12}CO peaks and speculate on the presence of strongly obscured SF regions.

Another set of FIR observations, complemented by [N II] and $\text{H}\alpha$ data, was acquired by Smith et al. (1994). They noticed that the FIR emission does not follow $\text{H}\alpha$. Different reasons, like high extinction in the center obscuring the SF or AGN dust heating were examined but considered as unlikely compared to the dust heating by an old stellar population. Also Chemin et al. (2003) observed an offset of a few arcsec between the locations of $\text{H}\alpha$ and CO maxima. The extinctions effect of dust is estimated to be $\sim 2^{\text{mag}}$ and of importance in nucleus, bulge and the ends of the bar (e.g. Mazzalay et al., 2013; Smith et al., 1994, see also).

The kinematic properties of NGC 3627 are quite diverse. On one hand the isoveLOCITY contours in H_2 show spikes northeast and southwest of the center. Using hydrodynamical models, Mazzalay et al. (2013) interpret this as the signature of shocked gas streaming down the stellar bar and invoke the oval flow of gas along the major axis (P.A.= 0°) of the H_2 emission in the inner 2''. They further conclude that the found angular displacement angle between the major axis of the stellar bar and the major axis of the oval flow results in strong torques being exerted on the H_2 gas. Gas inflow towards the center is a possible consequence. This is in agreement with Casasola et al. (2011) who find negative torques, say torques promoting gas inflow. An inflow is a non-circular motion and they find evidence that this is induced by the 18'' bar and the spiral in their rotation curves. They suggest that the fast rotating bar is too young to create an ILR which would stop the inflow of gas and rather distributes it in a circumnuclear ring. This gas inside the corotation of the primary bar is evidence for a so-called 'smoking gun' of inner gas inflow. Chemin et al. (2003) argue the non-circular motion not only to be due to the bar but also to be a result of the interaction with NGC 3628 (see also Afanasiev & Sil'chenko, 2005). Instead of an inflow, Haan et al. (2009) find the outflow of gas from the central disk to a distance of 0.6kpc accumulating in

4. NGC 3627

the ultraharmonic resonance at 0.45kpc.

In contrast to the gas, the LOSV map of the stellar component shows a regular rotation pattern with a kinematical major axis different from that of the gas. Afanasiev & Sil'chenko (2005) conclude on the presence of a circumnuclear ($r < 5''$) stellar disk or an oblate bulge. Dumas et al. (2007) note a slight variation in the area closer than $3''$ from the nucleus.

Starformation is definitively present, as expected for a late-type spiral galaxy. To which extend it takes place in NGC 3627 is not so clear. Casasola et al. (2011) find a low nuclear SFR while Warren et al. (2010) conclude on 'intense starformation' (see also Dahlem et al., 1996; Duan, 2006). Stars are also formed in the ends of the bar and along the spiral arm. Since dust plays a major role in the observations of this galaxy, it could add some uncertainty to the measurements. A nuclear SF event was brief and about 1 Gyr in the past (Afanasiev & Sil'chenko, 2005). The SF is reported as not to be dominant (Casasola et al., 2011) over the photoionisation by the LINER/Seyfert 2 AGN (Dahari, 1985; Ho et al., 1997; Keel, 1983b,c; Smith et al., 1994). It is one of the aims of this work to estimate how much the nuclear SF influences the classification of the central photoionising source.

The stellar population of NGC 3627 is of the same age in disk and bulge (Duan, 2006), and is estimated to be of intermediate age ($T \approx 3 - 5\text{Gyr}$, with $Z = Z_{\odot}$). In contrast, the nucleus is very young with $T \approx 1\text{Gyr}$ assuming $Z = Z_{\odot}$ (Afanasiev & Sil'chenko, 2005).

4.2 Observations and Data Reduction

The here presented data was observed in 4 different nights between 18 December 2004 and 17 February 2005 with the Visible Multi-Object Spectrograph (VIMOS; Le Fèvre et al. (2003)) at ESO's Very Large Telescope (VLT) unit *Melipal* in Paranal, Chile. Only the blue grating in high-resolution mode was used, covering the spectral range from 4120 to 6217 Å with a sampling of 0.54 Å per spectral bin. The spatial sampling is $0''.66$ per spatial pixel ('spaxel') and the FOV comprises an area of $27'' \times 27''$ with 40×40 spaxels. Three images per night were recorded, where the second exposure was

dedicated sky emission measurements. In total, 8 exposures targeted on NGC 3627 were obtained with an integration time of 830 s for each exposure. The data is seeing limited with the lowest DIMM seeing of $0''.79$. In any other respect, the observational data of NGC 3626 was treated as described in Sec. 3.2. The final FOV is $24''.4 \times 27''.0$ with the FWHM of the PSF of $\approx 2''.3$. The final spectra range from $4320 - 5150 \text{ \AA}$ and have an instrumental resolution of $\sigma = 42.9 \text{ km s}^{-1}$.

The fit of the stellar continuum to the galaxy spectra was performed as described in Sec. 3.2. Spectra to which the fit's absolute deviation was higher than 2.5% were disregarded for the scientific analysis. This threshold offered the best compromise between data quality and size of the FOV. In Fig. 4.1 I present the results of exemplary fits.

The emission line fitting procedures distinguishes itself in only one detail. The fit of both [O III] emission lines was additionally constrained to have a constant spectral difference between them.

4.3 Results

4.3.1 Morphology

In the left panel of Fig. 4.2 the SDSS i-band continuum image shows a large scale view on NGC 3627. Most noticeable are the asymmetry of the spiral arms and their dust lanes, both emerging from the northern and southern tip of the bar. The continuum emission in the VIMOS FOV (right panel of Fig. 4.2) is characterised by its apparently elliptical shape. The P.A. of the isophotes is $\sim 161^\circ$ at $r \approx 8''$ in agreement with the values for the stellar bar found by Casasola et al. (2011); Mazzalay et al. (2013). The P.A. changes to 138° at $r \approx 3''$ from the continuum peak. The ellipticity of the isophotes decreases with distance to the nucleus as well until it becomes almost circular in the center.

4.3.2 Emission

In Fig. 4.3 I present the gas emission line maps with the superposed continuum isophotes, and their respective error maps. The [O III] emission peaks slightly off-

4. NGC 3627

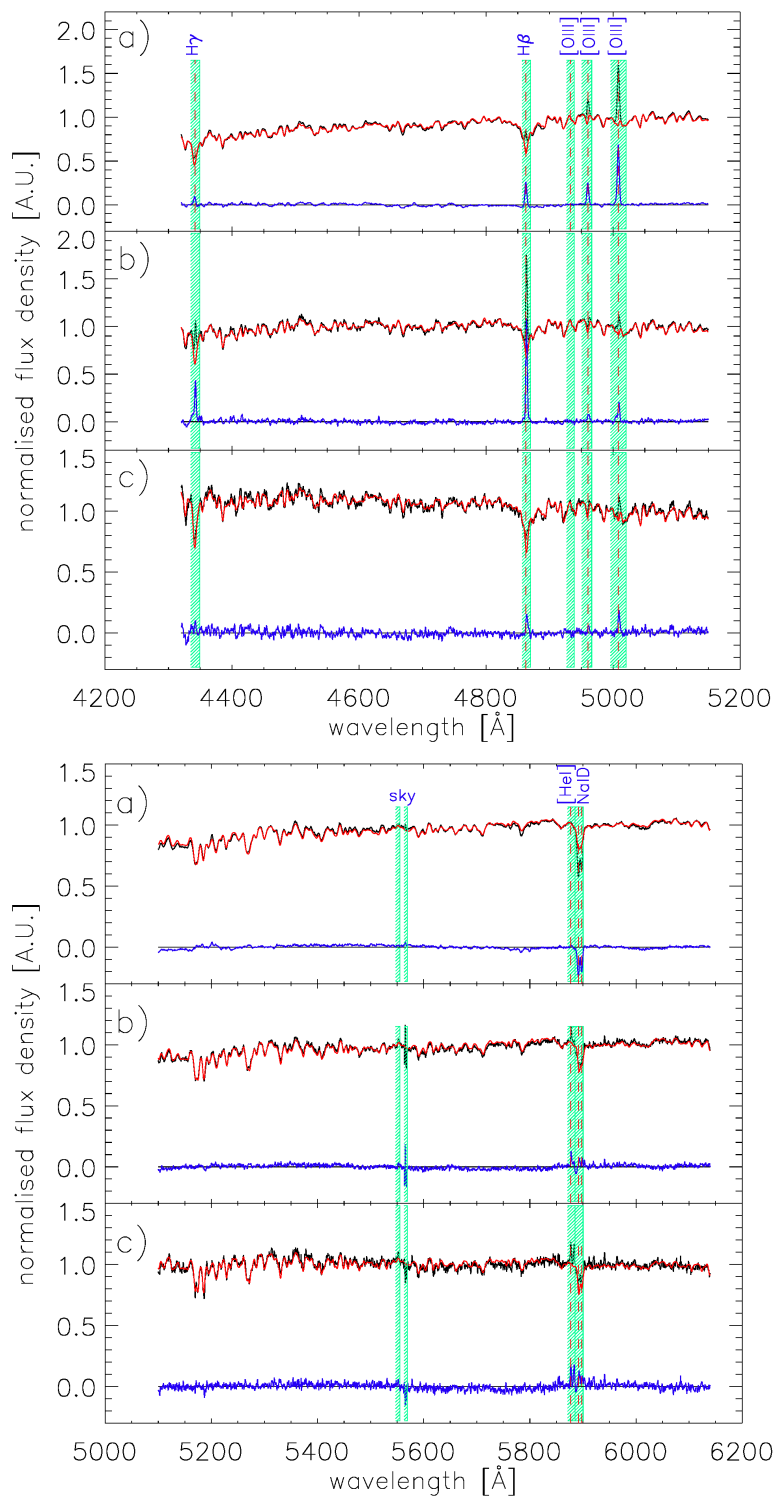


Figure 4.1: Fits with STARLIGHT of the stellar continuum in the galaxy core (a), a SF region (b), and a spaxel with low S/N (c). The galaxy spectrum is plotted in black, the fit in red and the residual in blue. Areas marked with the green background were masked out and were not taken into account by the fitting algorithm.

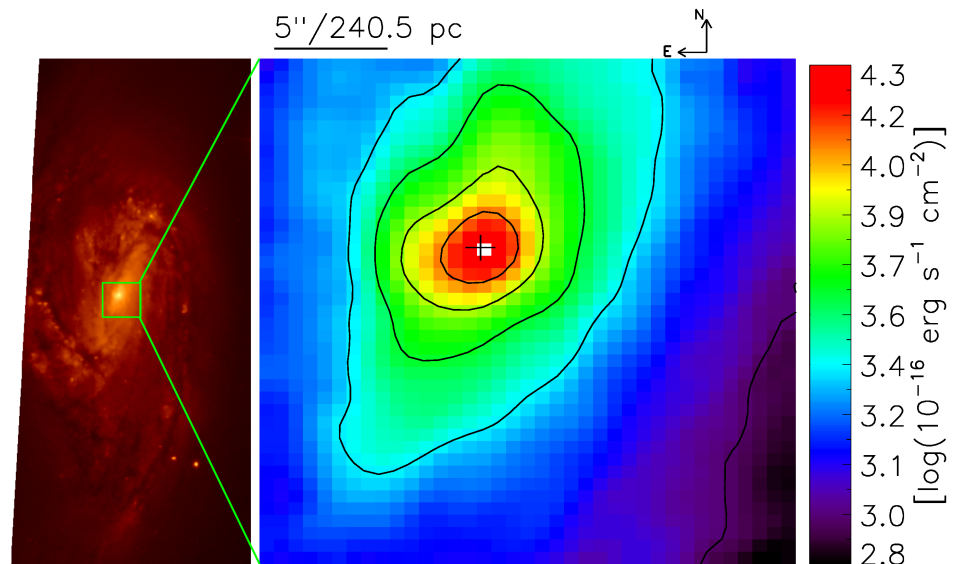


Figure 4.2: Left: SDSS i-band image of NGC 3627 in logarithmic color scale. Right: VIMOS continuum image of NGC 3627 from 6000 to 6100Å zoomed in on the central $24.3'' \times 27''$, also in logarithmic color scale. The contours represent 40, 50, 60, 80, 90 and 95% of the maximum logarithmic flux density. The continuum peak is marked with a black cross.

core (defined as the maximum continuum emission) and shows some weak extensions along the stellar bar. The Balmer emission shows the same behaviour, but the $H\beta$ map displays an extension to the southwest. As a result, the $H\beta$ follows nicely the inner isophotes of the continuum emission. As in the [O III] map, the weak emission follows the stellar bar. Furthermore, there is a region of increased Balmer emission $\sim 13''$ south of the center, which is most likely a SF-region.

4.3.3 Kinematics

The LOSV maps of the ionised gas (Fig. 4.4) is very irregular. The kinematic maps present themselves as patchy with a number of kinks. However, the large scale rotation is visible with the approaching part in the north and the receding gas in the south of the nucleus. The isovelocity contours form an s-shape, as often observed in gas and stars under the influence of a bar. This s-shape, though somewhat shallower, is also visible in the *stellar* LOSV map (Fig. 4.6, see also Dumas et al. (2007)). In [O III] the s-shape is stronger compared to $H\beta$, resulting in a deep wedge of negative velocities

4. NGC 3627

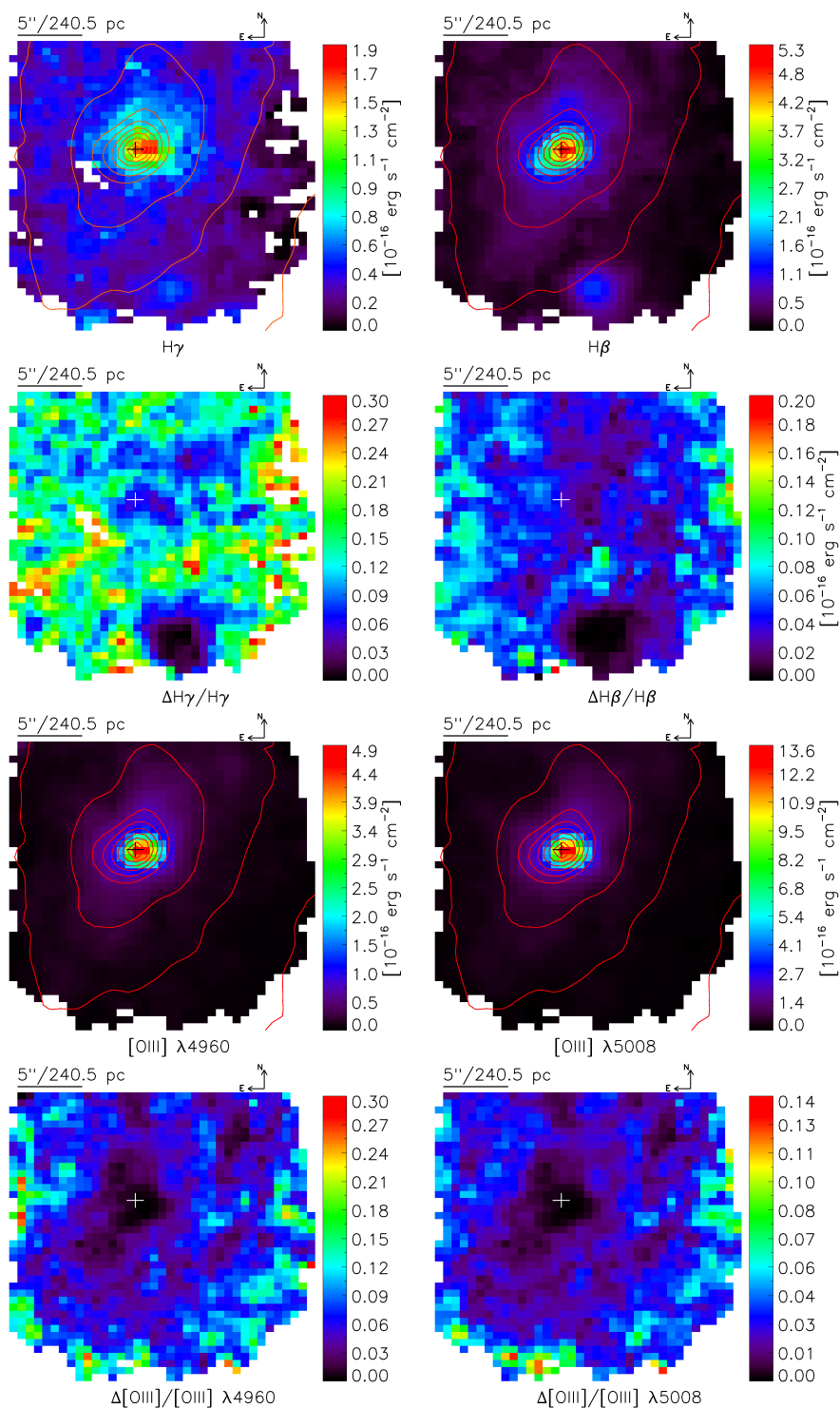


Figure 4.3: In row 1 and 3 the emission line flux maps of the indicated species are displayed. The distribution of the continuum flux is superimposed with red contours for 3, 5, 10, 20, 40, 50, 60, 70, 80, 90, and 95 % of the continuum peak emission. In row 2 and 4 the respective relative error maps are shown.

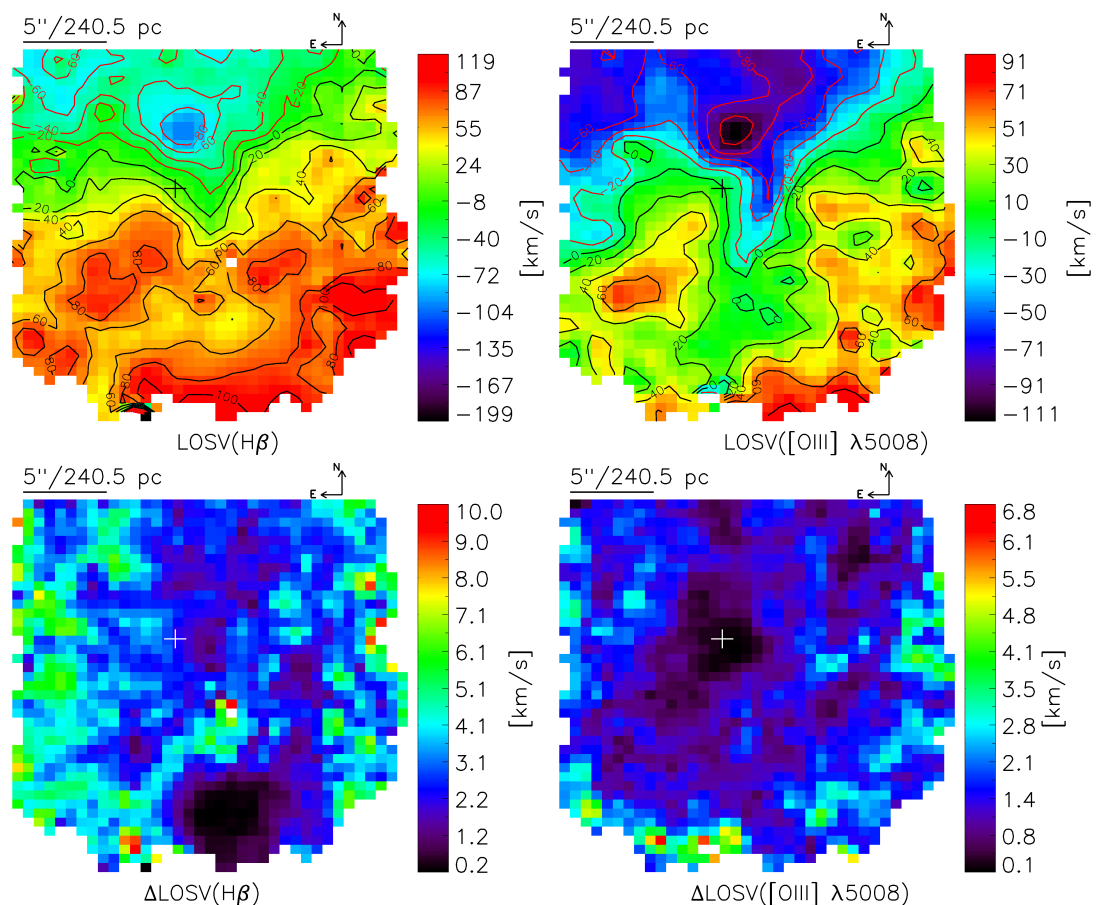


Figure 4.4: The LOSV maps of the $H\beta$ and $[O\text{ III}]\lambda 5008$ gas emission and their respective error maps. Blue colours represent gas approaching the observer, red colors describe receding velocities. The isovelocity contour lines are red colored for approaching velocities, blue for receding velocities in steps of 20 km s^{-1} . The cross marks the position of the stellar continuum peak.

reaching into the area south-east of the nucleus. Further, I note local velocity extrema $\approx 4''$ north and south of the nucleus to which I find a counterpart in the stellar LOSV map (left panel of Fig. 4.6). I found these features as well in the $[O\text{ III}]\lambda 5008$ and the stellar LOSV maps from [Dumas et al. \(2007\)](#).

The $H\beta$ LOSV dispersion map in the left panel of Fig. 4.5 show a region of low values in an elliptical region with its center displaced to the east from the continuum peak. This area is delineated by a scattered ring of increased dispersion with the largest fragment (and also with the highest values) located west of the nucleus. This high

4. NGC 3627

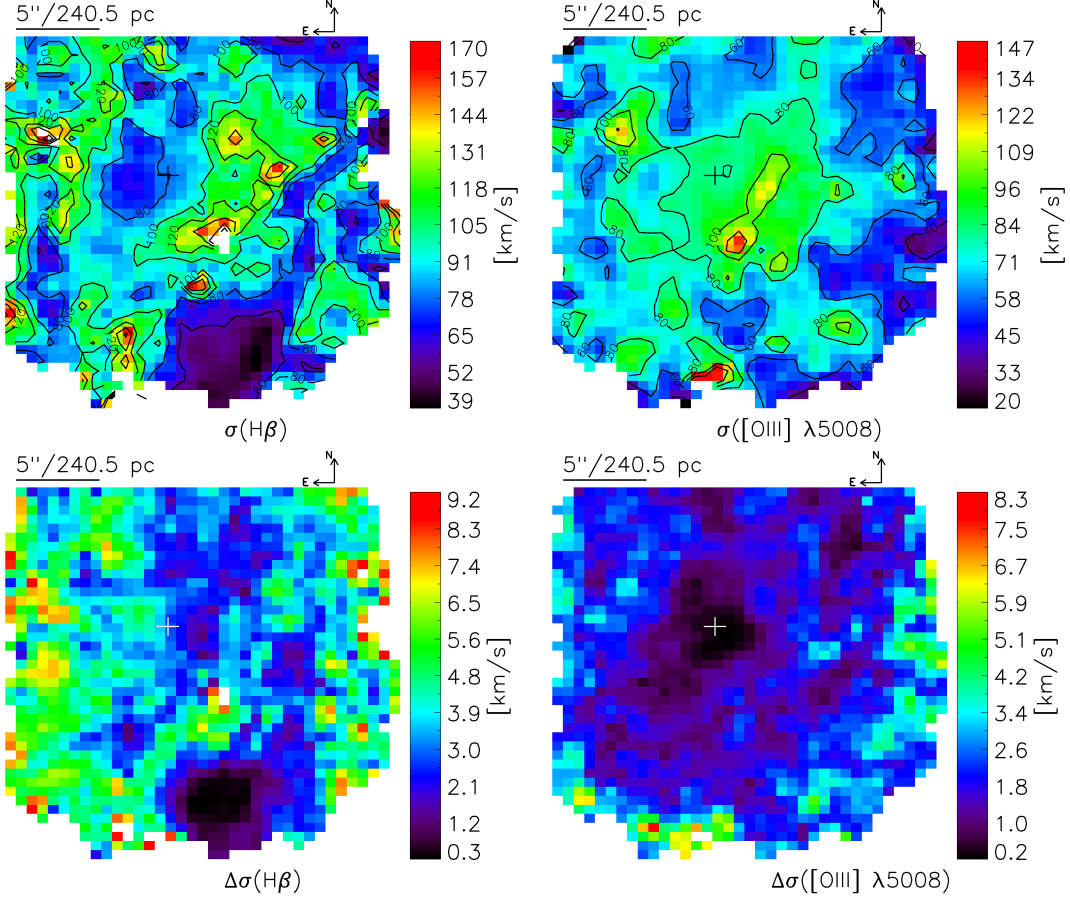


Figure 4.5: The LOSV dispersion σ of H β and [O III] $\lambda 5008$, and their respective relative error maps. The maps are corrected for instrumental resolution.

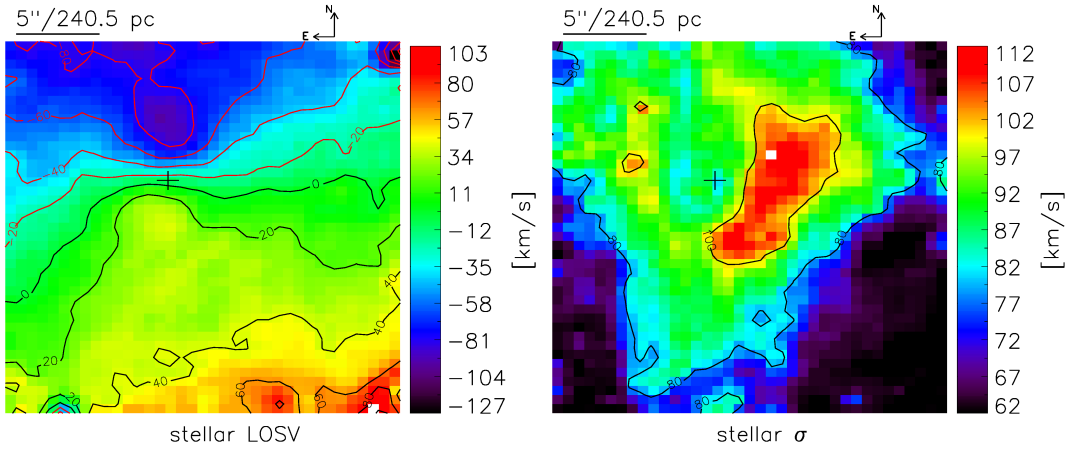


Figure 4.6: The LOSV (left) and the LOSV dispersion (right) map of the stellar emission as produced by STARLIGHT. The contours are the same as in 4.4.

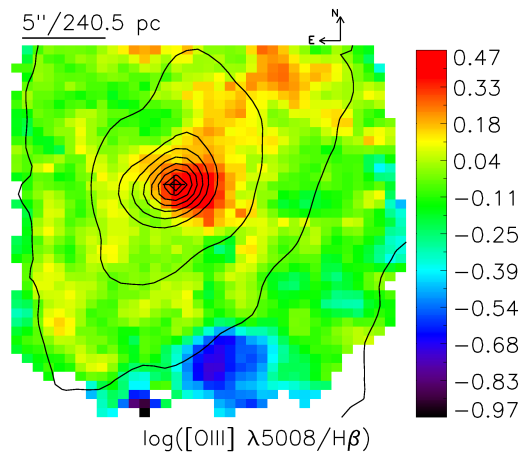


Figure 4.7: Logarithmic emission line ratio map $\log([\text{O III}] \lambda 5008/\text{H}\beta)$ overplotted with stellar continuum contours.

dispersion fragment can also be seen in $[\text{O III}]$ where it coincides with the afore described wedge in the LOSV field. The wedge is characterised by a strong velocity gradient and therefore, beam smearing could play a role. Interestingly, the high dispersion fragment has a very prominent counterpart in the *stellar* LOSV dispersion (right panel of Fig. 4.6). Since the *stellar* LOSV field does not show strong gradients in this area I interpret the observed dispersion as intrinsic. Consequently, also the gas dispersion might be real and not the result of an instrumental effect.

A stellar counterpart for the high LOSV dispersion ring in the gas is visible as well but I cannot recognise it in the gas map from [Dumas et al. \(2007\)](#), possibly their chosen velocity range does not allow for the necessary contrast. For completeness, I find very low LOSV dispersion values in $\text{H}\beta$ in the region diagnosed afore with increased $\text{H}\beta$ emission $\sim 13''$ south of the center.

4.3.4 Excitation

To analyse the dominant excitation mechanisms I present in Fig. 4.7 the $\log([\text{O III}] \lambda 5008/\text{H}\beta)$ map. It is largely dominated by the $[\text{O III}]$ emission and peaks slightly off-core south-west of the center. I note an extension of the peak region to the south-west, not following the continuum isophotes. Increased values are also stretching out to the north-west out to $r \sim 10''$ with a P.A. of 324° , a value similar to the P.A. of the inner continuum isophotes. Very low line ratios can be found $\sim 13''$ south of the center.

4.4 Discussion

The analysis of the VIMOS data of NGC 3627 is not complete yet. Therefore, all conclusions drawn in the following are preliminary.

4.4.1 Discussion and Interpretation

The elongation of the brightness distribution in the continuum image confirms the detection of a stellar bar with $P.A._{major} \approx 161^\circ$. Since the isophotes become increasingly circular with decreasing distance to the center ($r < 5''$) it is likely that an axisymmetric component is dominating the nuclear continuum emission. This is in agreement with the H_2 observations by [Mazzalay et al. \(2013\)](#) (see also [Afanasiev & Sil'chenko, 2005](#)).

The change of the stellar isophotal P.A. of the inner $8''$ w.r.t. to more distant isophotes might indicate another bar-like stellar distribution or elliptical orbits of the stars. This change can be seen in former publications (e.g. [Afanasiev & Sil'chenko, 2005](#)). The P.A. assumes a value of $\sim 138^\circ$ and coincides with the central distribution of the ionised gas. This means that in this region the gas might be associated to the stars or is ionised by them. However, the distribution of the low emission part of the ionised gas follows the large scale stellar bar.

The peaks of the ionised gas emission are located slightly off-core, about $1''$ to the west. This might be the result of extinction effects, which are reported to be up to 2^{mag} in the nuclear region ([Casasola et al., 2011](#); [Mazzalay et al., 2013](#); [Smith et al., 1994](#)).

The kinematics of the ionised gas is very diverse. It shows s-shaped isovelocity contours in the central region which could be due to the kinematic impact of the stellar bar on the gas ([Athanassoula, 1992](#); [Friedli & Martinet, 1993](#); [Shlosman et al., 1989](#)). Non-circular motion is indicated by the fact that the zero-velocity contour line is not perpendicular to the kinematic P.A. of the ionised gas. Furthermore, we find strong spikes in the kinematic morphology which are thought to be due to shocks ([Mazzalay et al., 2013](#)). The molecular gas LOSV map of [Mazzalay et al. \(2013\)](#) is similar to the here presented LOSV map of ionised gas. They successfully modelled the LOSV field of NGC 3627 for molecular gas (H_2) as a combination of gas in an oval flow with shocks along the stellar bar. Further, they conclude on the presence of significant torques from

the stellar bar exerted on the gas. Torques are necessary to drive gas in- or outflows. [Haan et al. \(2009\)](#) find in their ^{12}CO observations from torque analysis a gas outflow from the central disk out to 0.5 kpc. In contrast, [Casasola et al. \(2011\)](#) derive from their torque analysis that CO gas is transported inwards, also because there has not been the time yet to form an ultraharmonic resonance which manifests itself as a ring. Though not visible in the maps by [Mazzalay et al. \(2013\)](#), in the here presented maps of LOSV dispersion of ionized gas I find a ring-shaped signature of increased values. Even stronger it is visible in the stellar LOSV dispersion map. Possibly NGC 3627 displays a so-called σ -drop, a decrease of stellar velocity dispersion in the nucleus ([Emsellem et al., 2001](#)). σ -drops are connected to dynamically cold structure (e.g. SF-regions, disks) in numerical simulations by [Wozniak et al. \(2003\)](#). A very young nuclear stellar population (1 Gyr) was found by [Afanasiev & Sil'chenko \(2005\)](#), in agreement with the simulations, which propose the kinematics to be dominated by young stars. In this case the ring is just the area where the kinematical influence of the young stars ceases.

I also note that the highest gas dispersion values coincide spatially with the deep wedge in the gas LOSV field. As [Mazzalay et al. \(2013\)](#) pointed out, shocks might explain this. For shocks one could expect a correlation of the gas dispersion with the $\log([\text{O III}] \lambda 5008/\text{H}\beta)$ ratio. I do not see this correlation in the data. Possibly beam smearing is responsible for the increased gas dispersion.

The logarithmic emission line ratios are used to determine the dominant ionisation mechanism. To perform this task one requires two different line ratios. Unfortunately, the observations of NGC 3627 yield only the ratio of $\log([\text{O III}] \lambda 5008/\text{H}\beta)$ and the $[\text{N II}]$ map published by [Afanasiev & Sil'chenko \(2005\)](#) is given without flux values. NGC 3627 has been classed as a LINER/Seyfert 2 galaxy ([Ho et al., 1997](#)). The here measured emission line ratio for the core region is in agreement with this classification. Also its compactness does not contradict the presence of a low-luminosity AGN. The arm of increased line ratio values, expanding from the center to the northwest, is consistent with LINER-like emission as well. Since LINER-like emission can be due to different ionisation mechanisms (see Sec. 2.4), a more detailed analysis is necessary. This is not part of this work, but in the light of the models by [Mazzalay et al. \(2013\)](#) shocks appear to be the most likely explanation.

4.4.2 Outlook

What else could be done? The line ratio of $H\beta/H\gamma$ gives us the opportunity to calculate the extinction. As a next step, from the known extinction we can calculate the $H\alpha$ emission and consequently the SFR.

The creation of a map of weighted stellar ages might give us a hint on whether the ring of increased LOSV dispersions is associated with a particular stellar population. Probing the resolved stellar populations in the central region could help to distinguish possible remnants of a merger as discussed for 3626.

To evaluate whether an old stellar population has a significant part in the ionisation of the gas, the $EW_{H\alpha}$ needs to be measured. Since no direct measurement of the $H\alpha$ line is available, I can make use of the relation $EW_{H\beta} = 0.25 \times EW_{H\alpha}$ (Stasińska & Sodr , 2001).

NGC 3627 has shown the complexity of the kinematics that is possible due to the interaction with another galaxy. Even more, not only did NGC 3627 interact with NGC 3628, but it might have undergone a collision with a dwarf galaxy (Weżgowiec et al., 2012). However, in the here presented data I cannot find any direct evidence for this. Although the feeding mechanisms have been discussed in the previous section, the here listed steps could help to further the understanding of the feeding of the AGN.

5

Discussion and Conclusions

The aim of this work was to examine the mechanisms of feeding the AGN, its possible feedback, and the ionisation structure in galaxies that are classed as LLAGN. I performed this for three galaxies (NGC 5850, NGC 3626, and NGC 3627) part of the ‘extended’ NuGA sample using optical IFS data from the VIMOS IFU at the VLT.

5.1 Ionisation

One of the main topics of this work is that galaxies classed as LINERs are not always genuinely LINERs in the sense of the original definition (Heckman, 1980). Actually, a significant fraction of the LINERs would better be called ‘LINER-like’ since their dominant contribution to the ionisation of the gas does not originate from the nucleus. Different mechanism can be responsible (see Sec. 1.1.6.2). It is particularly the extendedness of the LINER-like ionised region that facilitated the idea of distributed ionisation sources to play an important role. Before, most LINER spectra could not be identified as extended because of the lack of spatial resolution and having only one or two slits positioned on the nucleus. The discovery of extended LINER-like emission was boosted with the advent of telescopes with sufficiently high spatial resolution and also with the commission of IFUs. IFUs combine the two crucial ingredients to identify extended LINER-like emission: imaging and spectroscopy. However, surveys like SDSS helped significantly to develop diagnostic tools that enable the astronomer to distinguish between a genuine and a ‘fake’ LINERs (e.g. Cid Fernandes et al., 2011).

5. DISCUSSION AND CONCLUSIONS

The analysis of NGC 5850 in this work is a prime example for the determination of the dominant ionisation mechanism in a galaxy formerly classed as LINER. Most likely, the ionisation of the interstellar gas is predominantly due to the radiation from p-AGB stars. The indications for the presence of an AGN are sparse. Except for some asymmetric emission lines, which could hint on the presence of an outflow, no signs of activity can be found. If the SMBH in the center of NGC 5850 is active, then it is only on a very low level.

Also in NGC 3626 I find an extended region of LINER-like emission which seems to be dominated by the ionisation by p-AGB stars. However, it still has to be checked whether there is additional radio and/or X-ray data which could confirm the presence of an AGN. Since NGC 3626 is classed as an early-type elliptical galaxy the stellar population is expected to be red and old without any significant star formation. Nevertheless, a star forming ring is detected that delineates the central area and its LINER-like ionisation pattern. It is possible that the mass lost by the old stars has gathered in the ring due to harmonic resonances, providing the material to form a new generation of stars (Temi et al., 2009). This is a process called the ‘rejuvenation’ of the galaxy.

In contrast to the former two galaxies, in NGC 3627 I could not determine the ionisation mechanism reliably because the observed spectra did not cover all of the necessary emission lines. NGC 3627 has been classed as Seyfert2/LINER galaxy (Holt et al., 1997) and the only emission line ratio available in the VIMOS data agrees with that. It would have been interesting to make a more accurate measurement of the emission line ratios and, consequently, of its ionisation class. The fact that NGC 3627 is so close to the LINER/Seyfert 2 demarcation makes it potentially interesting to examine the change of the ionisation profile in comparison to NGC 5850 and NGC 3626. However, the region of the ionised gas is dominated by a point-source like feature having the strongest and hardest radiation within the FOV. I also observe some extended features in the gas emission and, particularly, in the emission line ratio. They might be associated to the presence of a bar, shocks, or an outflow.

5.2 AGN-Feeding

Providing matter for the SMBH requires the matter to be transported to the immediate vicinity of the nucleus. Without matter the nucleus cannot become active. However,

the matter must lose almost all of its angular momentum ($\sim 99.9\%$) to be brought to the central ~ 10 pc. Several mechanisms have been proposed and observed (see Sec. 1). The galaxies examined in this work have been chosen for their proximity and low luminosity. As it turned out, they were all subject to more or less intensive interactions with other galaxies. In 2 out of 3 galaxies (NGC 5858 and NGC 3627) I find bars. To create bars gravitational instabilities are required. The interaction with another galaxy naturally provides them.

NGC 5850 possesses a nested bar feature, where matter is transported along the large scale (primary) bar further inward. The transport and the bar stop at the ultraharmonic resonance (Lindblad resonance) and the matter forms a ring. A smaller (secondary) bar inside the ring potentially takes over the transport of gas to the center. Within the ring I observe two gas disks, counterrotating w.r.t. the stellar disk. In other words, the core region is kinematically decoupled. This requires the spatial distribution of the gas to be initially lopsided. The high velocity encounter with the neighbouring galaxy NGC 5846, approximately $10'$ away (corresponding to ~ 98 kpc unprojected) could have caused this. I also find that the gas disk is inclined by 24° w.r.t. the stellar disk. Such perturbations are likely removing angular momentum leading to the inflow of the gas.

NGC 3626 shows a number of peculiarities. It possesses two gas disks, one on large scale and one in the circumnuclear region ($R \lesssim 3''.1$). The data also show two stellar disks in a similar arrangement with the nuclear disk having an extent of $R \approx 4.3''$. The gas disks are counterrotating w.r.t. to the stellar disks. The circumnuclear gas disk is not aligned along the P.A. of the circumnuclear stellar disk. NGC 3626 is suspected to have undergone a minor merger, i.e. it has swallowed a dwarf galaxy. Evidence for this comes from indications for the presence of a distinct stellar population $\sim 4''.3$ north of the nucleus, but this option has to be explored further. Also the SF-ring could originate from the gas of the devoured dwarf galaxy. The P.A. of the isophotes of the stellar continuum turns with decreasing distance to the center and the ionised gas is extended composing a bar-like or a spiral feature that connects the nucleus with the SF-ring. The feeding of the SMBH along this feature appears feasible. In the overall picture the nucleus might be fed with the remnants of the merged dwarf galaxy.

The most complicated kinematics is observed in NGC 3627. I find indications for oval streaming of gas and stars together with shocks along the stellar bar, which were

5. DISCUSSION AND CONCLUSIONS

also reported and modeled by other scientists (e.g. [Mazzalay et al., 2013](#)). I observe a ring of increased stellar LOSV dispersion which finds its counterpart in the ionised gas. Most prominent is a large area of increased stellar LOSV dispersion which coincides with a deep wedge in the LOSV field of the gas. In the literature the LOSV wedge has been explained by shocks ([Mazzalay et al., 2013](#)). However, the ring structure reminds of NGC 3626 where the gas might come from a merger event. NGC 3627 is reported to be subject of a recent minor merger as well ([Weżgowiec et al., 2012](#)), which offers the potential observation of the remnants, but I do not find any clear indication for this. The analysis on this topic has to be continued. The observed oval flows in combination with shocks exert significant torques on the gas possibly resulting in an inflow, as reported by [Casasola et al. \(2011\)](#).

The here examined galaxies were not selected for this feature but they all show signs of interaction. Although three galaxies are not a statistically representative sample, it nevertheless emphasises the importance of mergers and encounters in the context of feeding central SMBHs. This is supported by the life time of merger, which are about 10^8 to 10^9 years [Chatterjee \(1987\)](#). That means that the merging of galaxies is an ongoing process and should have occurred even more frequently at higher redshift, where the galaxies were closer to each other.

The fact that I observe non-circular gas motion (presumably inflowing gas) without any notable activity of the nucleus might indicate three issues: First, it is not transported yet to the nucleus and is stuck in an area which is not resolved by the data. Second, the amount of matter is not sufficient to trigger notable activity. Third, the accretion of matter on the SMBH does not ‘ignite’ immediately the nuclear activity. In either case, deeper and more resolved data is necessary. In the context of the AGN paradigm and the role of LINERs within it, this work shows the importance of carefully distinguishing between the different ionisation mechanisms.

Bibliography

- Afanasiev, V. L. & Sil'chenko, O. K. 2005, *A&A*, 429, 825
[107](#), [108](#), [116](#), [117](#)
- Algorry, D. G., Navarro, J. F., Abadi, M. G., et al. 2014, *MNRAS*, 437, 3596 [80](#)
- Allen, D. A. 1976, *MNRAS*, 174, 29P [32](#)
- Antonucci, R. R. J. & Miller, J. S. 1985, *ApJ*, 297, 621 [10](#)
- Arribas, S., Colina, L., & Clements, D. 2001, *ApJ*, 560, 160
[67](#), [69](#)
- Asplund, M., Grevesse, N., Sauval, A. J., & Scott, P. 2009, *ARA&A*, 47, 481 [64](#)
- Athanassoula, E. 1992, *MNRAS*, 259, 345 [116](#)
- Baganoff, F. K., Bautz, M. W., Brandt, W. N., et al. 2001, *Nature*, 413, 45 [3](#)
- Baganoff, F. K., Bautz, M. W., Ricker, G. R., et al. 2002, in *Bulletin of the American Astronomical Society*, Vol. 34, *Bulletin of the American Astronomical Society*, 1153 [3](#)
- Baganoff, F. K., Maeda, Y., Morris, M., et al. 2003, *ApJ*, 591, 891 [3](#)
- Baldwin, J. A., Phillips, M. M., & Terlevich, R. 1981, *PASP*, 93, 5 [37](#), [93](#)
- Bélangier, G., Terrier, R., de Jager, O. C., Goldwurm, A., & Melia, F. 2006, *Journal of Physics Conference Series*, 54, 420 [3](#)
- Berentzen, I., Shlosman, I., & Jogee, S. 2006, *ApJ*, 637, 582
[83](#)
- Binette, L., Magris, C. G., Stasińska, G., & Bruzual, A. G. 1994, *A&A*, 292, 13 [15](#), [19](#), [41](#), [42](#)
- Blanc, G. A., Heiderman, A., Gebhardt, K., Evans, II, N. J., & Adams, J. 2009, *ApJ*, 704, 842 [63](#)
- Bouchet, P., Lequeux, J., Maurice, E., Prevot, L., & Prevot-Burnichon, M. L. 1985, *A&A*, 149, 330 [32](#)
- Bremer, M., Scharwächter, J., Eckart, A., et al. 2013, *A&A*, 558, A34 [79](#), [98](#), [100](#)
- Bremer, M., Witzel, G., Eckart, A., et al. 2011, *A&A*, 532, A26 [3](#)
- Bruzual, G. & Charlot, S. 2003, *MNRAS*, 344, 1000 [46](#)
- Buchholz, R. M., Witzel, G., Schödel, R., et al. 2011, *A&A*, 534, A117 [3](#)
- Burtscher, L., Meisenheimer, K., Tristram, K. R. W., et al. 2013, *A&A*, 558, A149 [12](#)
- Buta, R. & Crocker, D. A. 1993, *AJ*, 105, 1344 [42](#)
- Buta, R., van Driel, W., Braine, J., et al. 1995, *ApJ*, 450, 593
[79](#)
- Calzetti, D. 1997, *AJ*, 113, 162 [32](#), [49](#)
- Calzetti, D. 2012, *ArXiv e-prints* [62](#), [63](#)
- Calzetti, D., Armus, L., Bohlin, R. C., et al. 2000, *ApJ*, 533, 682 [32](#)
- Cappellari, M., Emsellem, E., Krajnović, D., et al. 2011, *MNRAS*, 413, 813 [79](#)
- Cardelli, J. A., Clayton, G. C., & Mathis, J. S. 1989, *ApJ*, 345, 245 [32](#), [45](#)
- Carroll, B. W. & Ostlie, D. A. 2006, *An introduction to modern astrophysics and cosmology (Institute for Mathematics and Its Applications)* [5](#), [7](#), [8](#)
- Casasola, V., Hunt, L. K., Combes, F., García-Burillo, S., & Neri, R. 2011, *A&A*, 527, A92 [106](#), [107](#), [108](#), [109](#), [116](#), [117](#), [122](#)
- Chatterjee, T. K. 1987, *Ap&SS*, 137, 267 [122](#)
- Chemin, L., Cayatte, V., Balkowski, C., et al. 2003, *A&A*, 405, 89 [106](#), [107](#)
- Cid Fernandes, R., Mateus, A., Sodré, L., Stasińska, G., & Gomes, J. M. 2005, *MNRAS*, 358, 363 [46](#)
- Cid Fernandes, R., Schlickmann, M., Stasińska, G., et al. 2009, in *Astronomical Society of the Pacific Conference Series*, Vol. 408, *The Starburst-AGN Connection*, ed. W. Wang, Z. Yang, Z. Luo, & Z. Chen, 122 [15](#), [42](#)
- Cid Fernandes, R., Stasińska, G., Mateus, A., & Vale Asari, N. 2011, *MNRAS*, 413, 1687 [71](#), [119](#)
- Cid Fernandes, R., Stasińska, G., Vale Asari, N., et al. 2010, in *IAU Symposium*, Vol. 267, *IAU Symposium*, 65–72 [71](#)
- Ciri, R., Bettoni, D., & Galletta, G. 1995, *Nature*, 375, 661
[79](#), [80](#), [81](#), [82](#), [83](#)
- Coccatto, L., Morelli, L., Pizzella, A., et al. 2014, *ArXiv e-prints* [100](#), [104](#)
- Condon, J. J., Cotton, W. D., & Broderick, J. J. 2002, *AJ*, 124, 675 [67](#)
- Contini, M. 2011, *MNRAS*, 418, 1935 [3](#)
- Dahari, O. 1985, *ApJS*, 57, 643 [108](#)
- Dahlem, M., Heckman, T. M., Fabbiano, G., Lehnert, M. D., & Gilmore, D. 1996, *ApJ*, 461, 724 [108](#)
- de Lorenzo-Cáceres, A., Falcón-Barroso, J., & Vazdekis, A. 2013, *MNRAS*, 431, 2397 [64](#)

BIBLIOGRAPHY

- de Lorenzo-Cáceres, A., Falcón-Barroso, J., Vazdekis, A., & Martínez-Valpuesta, I. 2008, *ApJ*, 684, L83 [43](#), [53](#), [57](#), [78](#)
- de Mello, D. F., Urrutia-Viscarra, F., Mendes de Oliveira, C., et al. 2012, *MNRAS*, 426, 2441 [105](#)
- de Vaucouleurs, G., de Vaucouleurs, A., Corwin, Jr., H. G., et al. 1991, *Third Reference Catalogue of Bright Galaxies. Volume I: Explanations and references. Volume II: Data for galaxies between 0^h and 12^h . Volume III: Data for galaxies between 12^h and 24^h .* [80](#), [106](#)
- de Zeeuw, P. T., Bureau, M., Emsellem, E., et al. 2002, *MNRAS*, 329, 513 [2](#)
- Dodds-Eden, K., Porquet, D., Trap, G., et al. 2009, *ApJ*, 698, 676 [3](#)
- Dopita, M. A. & Sutherland, R. S. 1995, *ApJ*, 455, 468 [68](#)
- Dopita, M. A. & Sutherland, R. S. 1996, *ApJS*, 102, 161 [15](#), [42](#)
- Duan, Z. 2006, *AJ*, 132, 1581 [105](#), [106](#), [107](#), [108](#)
- Dudik, R. P., Satyapal, S., & Marcu, D. 2009, *ApJ*, 691, 1501 [18](#), [42](#)
- Dumas, G., Mundell, C. G., Emsellem, E., & Nagar, N. M. 2007, *MNRAS*, 379, 1249 [106](#), [108](#), [111](#), [113](#), [115](#)
- Eckart, A., Baganoff, F. K., Morris, M., et al. 2004, *A&A*, 427, 1 [3](#)
- Eckart, A., Baganoff, F. K., Morris, M. R., et al. 2009, *A&A*, 500, 935 [3](#)
- Eckart, A., Baganoff, F. K., Schödel, R., et al. 2006a, *A&A*, 450, 535 [3](#)
- Eckart, A., Baganoff, F. K., Zamaninasab, M., et al. 2008a, *A&A*, 479, 625 [3](#)
- Eckart, A., Britzen, S., Horrobin, M., et al. 2013a, *ArXiv e-prints* [3](#)
- Eckart, A., García-Marín, M., Vogel, S. N., et al. 2012a, *Journal of Physics Conference Series*, 372, 012022 [3](#)
- Eckart, A., García-Marín, M., Vogel, S. N., et al. 2012b, *A&A*, 537, A52 [3](#)
- Eckart, A. & Genzel, R. 1996, *Nature*, 383, 415 [3](#)
- Eckart, A., Genzel, R., Ott, T., & Schödel, R. 2002, *MNRAS*, 331, 917 [3](#)
- Eckart, A., Moulataka, J., Viehmann, T., et al. 2003, *Astronomische Nachrichten Supplement*, 324, 557 [3](#)
- Eckart, A., Mužić, K., Yazici, S., et al. 2013b, *A&A*, 551, A18 [3](#)
- Eckart, A., Schödel, R., García-Marín, M., et al. 2008b, *A&A*, 492, 337 [3](#)
- Eckart, A., Schödel, R., Meyer, L., et al. 2006b, *A&A*, 455, 1 [3](#)
- Eckart, A., Zamaninasab, M., Sabha, N., et al. 2011, in *Astronomical Society of the Pacific Conference Series*, Vol. 439, *The Galactic Center: a Window to the Nuclear Environment of Disk Galaxies*, ed. M. R. Morris, Q. D. Wang, & F. Yuan, 294 [3](#)
- Edln, B. 1966, *Metrologia*, 2, 71 [45](#)
- Eisenhauer, F., Genzel, R., Alexander, T., et al. 2005, *ApJ*, 628, 246 [3](#)
- Eisenhauer, F., Schödel, R., Genzel, R., et al. 2003, *ApJ*, 597, L121 [3](#)
- Elitzur, M. & Shlosman, I. 2006, *ApJ*, 648, L101 [17](#)
- Emsellem, E., Greusard, D., Combes, F., et al. 2001, *A&A*, 368, 52 [2](#), [117](#)
- Fabbiano, G., Elvis, M., Markoff, S., et al. 2003, *ApJ*, 588, 175 [19](#)
- Fabbiano, G., Kim, D.-W., & Trinchieri, G. 1992, *ApJS*, 80, 531 [43](#), [67](#)
- Fabian, A. C. 1994, *ARA&A*, 32, 277 [15](#), [41](#)
- Farage, C. L., McGregor, P. J., Dopita, M. A., & Bicknell, G. V. 2010, *ApJ*, 724, 267 [15](#), [42](#)
- Ferrarese, L. & Merritt, D. 2000, *ApJ*, 539, L9 [69](#)
- Filippenko, A. V. 1982, *PASP*, 94, 715 [45](#)
- Fitzpatrick, E. L. 1986, *AJ*, 92, 1068 [32](#)
- Fitzpatrick, E. L. & Massa, D. 1986, *ApJ*, 307, 286 [32](#)
- Flohic, H. M. L. G., Eracleous, M., Chartas, G., Shields, J. C., & Moran, E. C. 2006, *ApJ*, 647, 140 [16](#)
- Friedli, D. & Benz, W. 1993, *A&A*, 268, 65 [82](#)
- Friedli, D. & Martinet, L. 1993, *A&A*, 277, 27 [74](#), [116](#)
- Friedli, D., Wozniak, H., Rieke, M., Martinet, L., & Bratschi, P. 1996, *A&AS*, 118, 461 [42](#)
- García-Burillo, S., Combes, F., Schinnerer, E., Boone, F., & Hunt, L. K. 2005, *A&A*, 441, 1011 [74](#)
- García-Burillo, S., Sempere, M. J., & Bettoni, D. 1998, *ApJ*, 502, 235 [2](#), [79](#), [80](#), [81](#), [82](#), [83](#), [92](#), [93](#), [99](#), [104](#)
- García-Burillo, S., Sempere, M. J., Combes, F., Hunt, L. K., & Neri, R. 2000a, *A&A*, 363, 869 [2](#)
- García-Burillo, S., Sempere, M. J., Combes, F., Hunt, L. K., & Neri, R. 2000b, *A&A*, 363, 869 [76](#)
- García-Marín, M., Eckart, A., Weiss, A., et al. 2011a, *ApJ*, 738, 158 [3](#)
- García-Marín, M., Eckart, A., Weiss, A., et al. 2011b, in *Astronomical Society of the Pacific Conference Series*, Vol. 439, *The Galactic Center: a Window to the Nuclear Environment of Disk Galaxies*, ed. M. R. Morris, Q. D. Wang, & F. Yuan, 315 [3](#)
- Gebhardt, K., Bender, R., Bower, G., et al. 2000, *ApJ*, 539, L13 [69](#)

BIBLIOGRAPHY

- Genzel, R., Eckart, A., Ott, T., & Eisenhauer, F. 1997, MNRAS, 291, 219 [3](#)
- Genzel, R., Pichon, C., Eckart, A., Gerhard, O. E., & Ott, T. 2000, MNRAS, 317, 348 [3](#)
- Genzel, R., Schödel, R., Ott, T., et al. 2003, Nature, 425, 934 [3](#)
- Ghez, A. M., Duchêne, G., Matthews, K., et al. 2003, ApJ, 586, L127 [3](#)
- Ghez, A. M., Hornstein, S. D., Bouchez, A., et al. 2004a, in Bulletin of the American Astronomical Society, Vol. 36, Bulletin of the American Astronomical Society, 1384 [3](#)
- Ghez, A. M., Hornstein, S. D., Lu, J. R., et al. 2005, ApJ, 635, 1087 [3](#)
- Ghez, A. M., Klein, B. L., Morris, M., & Becklin, E. E. 1998, ApJ, 509, 678 [3](#)
- Ghez, A. M., Morris, M., Becklin, E. E., Tanner, A., & Kremenek, T. 2000, Nature, 407, 349 [3](#)
- Ghez, A. M., Salim, S., Weinberg, N. N., et al. 2008, ApJ, 689, 1044 [3](#)
- Ghez, A. M., Wright, S. A., Matthews, K., et al. 2004b, ApJ, 601, L159 [3](#)
- Gillessen, S., Eisenhauer, F., Trippe, S., et al. 2009, ApJ, 692, 1075 [3](#)
- Gillessen, S., Genzel, R., Fritz, T. K., et al. 2012, Nature, 481, 51 [3](#)
- Goldwurm, A., Brion, E., Goldoni, P., et al. 2003, ApJ, 584, 751 [3](#)
- González-Martín, O., Masegosa, J., Márquez, I., & Guainazzi, M. 2009, ApJ, 704, 1570 [18](#), [42](#)
- González-Martín, O., Masegosa, J., Márquez, I., Guerrero, M. A., & Dultzin-Hacyan, D. 2006, A&A, 460, 45 [16](#), [42](#)
- Graham, A. W., Onken, C. A., Athanassoula, E., & Combes, F. 2011, MNRAS, 412, 2211 [70](#)
- Gültekin, K., Richstone, D. O., Gebhardt, K., et al. 2009, ApJ, 698, 198 [69](#), [70](#)
- Haan, S., Schinnerer, E., Emsellem, E., et al. 2009, ApJ, 692, 1623 [106](#), [107](#), [117](#)
- Hanuschik, R. W. 2003, A&A, 407, 1157 [46](#)
- Haynes, M. P., Giovanelli, R., & Roberts, M. S. 1979, ApJ, 229, 83 [105](#)
- Haynes, M. P., Jore, K. P., Barrett, E. A., Broeils, A. H., & Murray, B. M. 2000, AJ, 120, 703 [79](#), [80](#), [81](#), [82](#), [84](#), [93](#), [99](#), [103](#)
- Heckman, T. & Best, P. 2014, ArXiv e-prints [1](#)
- Heckman, T. M. 1980, A&A, 87, 152 [13](#), [15](#), [41](#), [42](#), [43](#), [119](#)
- Heiles, C., Kulkarni, S., & Stark, A. A. 1981, ApJ, 247, L73 [65](#)
- Higdon, J. L., Buta, R. J., & Purcell, G. B. 1998, AJ, 115, 80 [43](#), [75](#), [76](#)
- Ho, L. C. 1999, ApJ, 510, 631 [16](#)
- Ho, L. C. 2008, ARA&A, 46, 475 [16](#), [18](#), [42](#), [67](#), [68](#), [70](#)
- Ho, L. C., Filippenko, A. V., & Sargent, W. L. W. 1996, ApJ, 462, 183 [14](#)
- Ho, L. C., Filippenko, A. V., & Sargent, W. L. W. 1997, ApJS, 112, 315 [13](#), [41](#), [82](#), [95](#), [108](#), [117](#), [120](#)
- Ho, L. C. & Ulvestad, J. S. 2001, ApJS, 133, 77 [16](#), [18](#)
- Hopkins, P. F. & Quataert, E. 2010, MNRAS, 407, 1529 [74](#)
- Hornstein, S. D., Matthews, K., Ghez, A. M., et al. 2007, ApJ, 667, 900 [3](#)
- Hummel, E., van der Hulst, J. M., Keel, W. C., & Kennicutt, Jr., R. C. 1987, A&AS, 70, 517 [67](#)
- Hunt, L. K., Combes, F., García-Burillo, S., et al. 2008, A&A, 482, 133 [74](#)
- Jore, K. P., Broeils, A. H., & Haynes, M. P. 1996, AJ, 112, 438 [82](#)
- Jullo, E., Christensen, L., Smette, A., et al. 2008, in 2007 ESO Instrument Calibration Workshop, ed. A. Kaufer & F. Kerber, 343 [44](#)
- Katkov, I., Sil'chenko, O., & Afanasiev, V. 2013, ArXiv e-prints [80](#)
- Kauffmann, G., Heckman, T. M., Tremonti, C., et al. 2003, Monthly Notes of the Royal Astron. Soc., 346, 1055 [13](#), [37](#), [38](#), [59](#), [60](#), [61](#), [96](#)
- Keel, W. C. 1983a, ApJS, 52, 229 [43](#)
- Keel, W. C. 1983b, ApJ, 269, 466 [108](#)
- Keel, W. C. 1983c, ApJ, 268, 632 [108](#)
- Kehrig, C., Monreal-Ibero, A., Papaderos, P., et al. 2012, A&A, 540, A11 [15](#), [42](#)
- Kennicutt, Jr., R. C. 1998, ARA&A, 36, 189 [62](#), [63](#)
- Kewley, L. J., Dopita, M. A., Sutherland, R. S., Heisler, C. A., & Trevena, J. 2001, Astroph. J., 556, 121 [15](#), [37](#), [38](#), [42](#), [59](#), [60](#), [61](#), [96](#)
- Kewley, L. J., Groves, B., Kauffmann, G., & Heckman, T. 2006, Monthly Notes of the Royal Astron. Soc., 372, 961 [59](#), [60](#), [61](#), [96](#)
- Koratkar, A., Deustua, S. E., Heckman, T., et al. 1995, ApJ, 440, 132 [19](#)
- Kormendy, J. & Bahcall, J. N. 1974, AJ, 79, 671 [105](#)
- Kormendy, J. & Ho, L. C. 2013, ARA&A, 51, 511 [3](#)
- Koski, A. T. 1976, PhD thesis, California Univ., Santa Cruz. [10](#)

BIBLIOGRAPHY

- Krajnović, D., Emsellem, E., Cappellari, M., et al. 2011, *MNRAS*, 414, 2923 [80](#)
- Kroupa, P. 2001, *MNRAS*, 322, 231 [63](#)
- Lagerholm, C., Kuntschner, H., Cappellari, M., et al. 2012, *A&A*, 541, A82 [44](#)
- Laine, S., Shlosman, I., Knapen, J. H., & Peletier, R. F. 2002, *ApJ*, 567, 97 [43](#)
- Laor, A. 2003, *ApJ*, 590, 86 [17](#)
- Laurikainen, E., Salo, H., & Buta, R. 2005, *MNRAS*, 362, 1319 [99](#)
- Le Fèvre, O., Saisse, M., Mancini, D., et al. 2003, in *Society of Photo-Optical Instrumentation Engineers (SPIE) Conference Series*, Vol. 4841, *Society of Photo-Optical Instrumentation Engineers (SPIE) Conference Series*, ed. M. Iye & A. F. M. Moorwood, 1670–1681 [44](#), [84](#), [108](#)
- Leon, S., Combes, F., & Friedli, D. 2000, in *Astronomical Society of the Pacific Conference Series*, Vol. 197, *Dynamics of Galaxies: from the Early Universe to the Present*, ed. F. Combes, G. A. Mamon, & V. Charmandaris, 61 [65](#), [76](#), [77](#)
- Leroy, A. K., Bigiel, F., de Blok, W. J. G., et al. 2012, *AJ*, 144, 3 [62](#)
- Lípari, S., Mediavilla, E., García-Lorenzo, B., et al. 2004, *MNRAS*, 355, 641 [15](#), [42](#)
- Lourenço, S., Aguerri, J. A. L., Vazdekis, A., Beckman, J. E., & Peletier, R. F. 2003, *Ap&SS*, 284, 925 [43](#), [49](#), [50](#), [51](#)
- Maiolino, R., Nagao, T., Grazian, A., et al. 2008, *A&A*, 488, 463 [63](#), [64](#)
- Maoz, D., Filippenko, A. V., Ho, L. C., et al. 1996, *ApJS*, 107, 215 [14](#)
- Maoz, D., Koratkar, A., Shields, J. C., et al. 1998, *AJ*, 116, 55 [14](#), [41](#)
- Marrone, D. P., Baganoff, F. K., Morris, M. R., et al. 2008, *ApJ*, 682, 373 [3](#)
- Martin, C. L. 2005, *ApJ*, 621, 227 [70](#)
- Masegosa, J., Márquez, I., Ramirez, A., & González-Martín, O. 2011, *A&A*, 527, A23 [70](#)
- Mazzalay, X., Maciejewski, W., Erwin, P., et al. 2013, *ArXiv e-prints* [106](#), [107](#), [109](#), [116](#), [117](#), [122](#)
- Merrifield, M. R. & Kuijken, K. 1994, *ApJ*, 432, 575 [79](#)
- Moiseev, A. V., Valdés, J. R., & Chavushyan, V. H. 2004, *A&A*, 421, 433 [43](#), [53](#), [70](#), [76](#)
- Monreal-Ibero, A., Arribas, S., Colina, L., et al. 2010, *A&A*, 517, A28 [15](#), [42](#)
- Morton, D. C. 1991, *ApJS*, 77, 119 [45](#)
- Murray, N. & Chiang, J. 1997, *ApJ*, 474, 91 [17](#)
- Nagar, N. M., Falcke, H., & Wilson, A. S. 2005, *A&A*, 435, 521 [16](#), [42](#), [67](#)
- Nandra, K., George, I. M., Mushotzky, R. F., Turner, T. J., & Yaqoob, T. 1997, *ApJ*, 477, 602 [14](#)
- Netzer, H. 2009, *MNRAS*, 399, 1907 [68](#)
- Nicastro, F. 2000, *ApJ*, 530, L65 [17](#)
- Osterbrock, D. E. & Ferland, G. J. 2006, *Astrophysics of gaseous nebulae and active galactic nuclei* [6](#), [13](#), [22](#), [24](#), [25](#), [28](#), [34](#), [36](#), [49](#)
- Park, D., Kelly, B. C., Woo, J.-H., & Treu, T. 2012, *ApJS*, 203, 6 [70](#)
- Peterson, B. M. 1997, *An Introduction to Active Galactic Nuclei* [3](#), [4](#), [11](#)
- Pettini, M. & Pagel, B. E. J. 2004, *MNRAS*, 348, L59 [64](#)
- Phillips, M. M., Jenkins, C. R., Dopita, M. A., Sadler, E. M., & Binette, L. 1986, *AJ*, 91, 1062 [16](#)
- Pogge, R. W., Maoz, D., Ho, L. C., & Eracleous, M. 2000, *ApJ*, 532, 323 [14](#), [41](#)
- Porquet, D., Grosso, N., Predehl, P., et al. 2008, *A&A*, 488, 549 [3](#)
- Porquet, D., Predehl, P., Aschenbach, B., et al. 2003, *A&A*, 407, L17 [3](#)
- Predehl, P. & Schmitt, J. H. M. M. 1995, *A&A*, 293, 889 [65](#)
- Prevot, M. L., Lequeux, J., Prevot, L., Maurice, E., & Rocca-Volmerange, B. 1984, *A&A*, 132, 389 [32](#)
- Prieto, M., Gottesman, S. T., Aguerri, J.-A. L., & Varela, A.-M. 1997, *AJ*, 114, 1413 [42](#)
- Pringle, J. E. 1996, *MNRAS*, 281, 357 [2](#)
- Ptak, A., Yaqoob, T., Mushotzky, R., Serlemitsos, P., & Griffiths, R. 1998, *ApJ*, 501, L37 [15](#)
- Quataert, E., Di Matteo, T., Narayan, R., & Ho, L. C. 1999, *ApJ*, 525, L89 [19](#)
- Reeves, J. N. & Turner, M. J. L. 2000, *MNRAS*, 316, 234 [14](#)
- Reuter, H.-P., Sievers, A. W., Pohl, M., Lesch, H., & Wielebinski, R. 1996, *A&A*, 306, 721 [106](#)
- Rich, J. A., Dopita, M. A., Kewley, L. J., & Rupke, D. S. N. 2010, *ApJ*, 721, 505 [15](#), [42](#)
- Rich, J. A., Kewley, L. J., & Dopita, M. A. 2011, *ApJ*, 734, 87 [62](#), [75](#), [102](#)
- Rots, A. H. 1978, *AJ*, 83, 219 [105](#)
- Rupke, D. S., Veilleux, S., & Sanders, D. B. 2005, *ApJS*, 160, 87 [70](#)
- Sabha, N., Witzel, G., Eckart, A., et al. 2010, *A&A*, 512, A2 [3](#)
- Sabra, B. M., Shields, J. C., Ho, L. C., Barth, A. J., & Filippenko, A. V. 2003, *ApJ*, 584, 164 [14](#)

BIBLIOGRAPHY

- Sandage, A. & Tammann, G. A. 1987, A revised Shapley-Ames Catalog of bright galaxies [80](#)
- Sarzi, M., Shields, J. C., Schawinski, K., et al. 2010, MNRAS, 402, 2187 [15](#), [42](#)
- Scharwächter, J., Dopita, M. A., Zuther, J., et al. 2011, AJ, 142, 43 [62](#), [64](#)
- Schawinski, K., Thomas, D., Sarzi, M., et al. 2007, MNRAS, 382, 1415 [37](#), [38](#)
- Schawinski, K., Urry, C. M., Simmons, B. D., et al. 2014, MNRAS [1](#)
- Schinnerer, E., Eckart, A., & Tacconi, L. J. 2000a, ApJ, 533, 826 [2](#)
- Schinnerer, E., Eckart, A., Tacconi, L. J., Genzel, R., & Downes, D. 2000b, ApJ, 533, 850 [2](#)
- Schmidt, M. & Green, R. F. 1983, ApJ, 269, 352 [5](#)
- Schödel, R., Merritt, D., & Eckart, A. 2009, A&A, 502, 91 [3](#)
- Schödel, R., Ott, T., Genzel, R., et al. 2003, ApJ, 596, 1015 [3](#)
- Schödel, R., Ott, T., Genzel, R., et al. 2002, Nature, 419, 694 [3](#)
- Seaton, M. J. 1979, MNRAS, 187, 73P [32](#)
- Seyfert, C. K. 1943, ApJ, 97, 28 [5](#)
- Sharp, R. G. & Bland-Hawthorn, J. 2010, ApJ, 711, 818 [15](#), [42](#), [68](#)
- Shen, Y., Richards, G. T., Strauss, M. A., et al. 2011, ApJS, 194, 45 [67](#), [68](#)
- Shi, L., Gu, Q. S., & Peng, Z. X. 2006, A&A, 450, 15 [63](#)
- Shields, G. A. 1978, Nature, 272, 706 [14](#)
- Shields, J. C., Rix, H.-W., Sarzi, M., et al. 2007, ApJ, 654, 125 [73](#)
- Shlosman, I., Frank, J., & Begelman, M. C. 1989, Nature, 338, 45 [2](#), [74](#), [116](#)
- Shu, F. H., Tremaine, S., Adams, F. C., & Ruden, S. P. 1990, ApJ, 358, 495 [2](#)
- Shuder, J. M. 1981, ApJ, 244, 12 [10](#)
- Sil'chenko, O. K., Moiseev, A. V., & Shulga, A. P. 2010, AJ, 140, 1462 [80](#), [81](#), [82](#), [83](#), [84](#), [92](#), [93](#), [97](#), [98](#), [99](#), [103](#), [104](#)
- Smith, B. J., Harvey, P. M., Colome, C., et al. 1994, ApJ, 425, 91 [106](#), [107](#), [108](#), [116](#)
- Soida, M., Urbanik, M., Beck, R., Wielebinski, R., & Balkowski, C. 2001, A&A, 378, 40 [105](#)
- Stasińska, G. & Sodr e, Jr., L. 2001, A&A, 374, 919 [118](#)
- Stasińska, G., Vale Asari, N., Cid Fernandes, R., et al. 2008, MNRAS, 391, L29 [15](#), [42](#)
- Temi, P., Brighenti, F., & Mathews, W. G. 2009, ApJ, 695, 1 [104](#), [120](#)
- Terashima, Y., Ho, L. C., & Ptak, A. F. 2000, ApJ, 539, 161 [18](#)
- Terlevich, R. & Melnick, J. 1985, MNRAS, 213, 841 [15](#), [42](#)
- Trinchieri, G. & di Serego Alighieri, S. 1991, AJ, 101, 1647 [15](#), [42](#)
- Tristram, K. R. W., Schartmann, M., Burtscher, L., et al. 2012, Journal of Physics Conference Series, 372, 012035 [12](#)
- Tutukov, A. V. & Fedorova, A. V. 2006, Astronomy Reports, 50, 785 [84](#)
- Valencia-S, M., Bursa, M., Karssen, G., et al. 2012, Journal of Physics Conference Series, 372, 012073 [3](#)
- Valencia-S., M., Zuther, J., Eckart, A., et al. 2012, A&A, 544, A129 [63](#)
- Veilleux, S. & Osterbrock, D. E. 1987, ApJS, 63, 295 [37](#), [93](#)
- Veilleux, S. & Rupke, D. S. 2002, ApJ, 565, L63 [15](#), [42](#)
- Vitale, M., Mignoli, M., Cimatti, A., et al. 2013, A&A, 556, A11 [37](#)
- Voit, G. M. & Donahue, M. 1997, ApJ, 486, 242 [15](#), [41](#)
- Walsh, J. L., Barth, A. J., Ho, L. C., et al. 2008, AJ, 136, 1677 [68](#)
- Warren, B. E., Wilson, C. D., Israel, F. P., et al. 2010, ApJ, 714, 571 [108](#)
- Watanabe, Y., Sorai, K., Kuno, N., & Habe, A. 2011, MNRAS, 411, 1409 [106](#)
- Weżgowiec, M., Soida, M., & Bomans, D. J. 2012, A&A, 544, A113 [106](#), [118](#), [122](#)
- Wisnioski, E., Glazebrook, K., Blake, C., et al. 2012, MNRAS, 422, 3339 [53](#)
- Witzel, G., Eckart, A., Bremer, M., et al. 2012, ApJS, 203, 18 [3](#)
- Wozniak, H., Combes, F., Emsellem, E., & Friedli, D. 2003, A&A, 409, 469 [117](#)
- Wozniak, H., Friedli, D., Martinet, L., Martin, P., & Bratschi, P. 1995, Astron. And Astroph., 111, 115 [42](#)
- Wrobel, J. M. 1991, AJ, 101, 127 [16](#)
- Yan, R. & Blanton, M. R. 2012, ApJ, 747, 61 [15](#), [42](#), [66](#), [71](#), [73](#), [74](#), [101](#)
- Yuan, F., Markoff, S., Falcke, H., & Biermann, P. L. 2002, A&A, 391, 139 [19](#)
- Yusef-Zadeh, F., Bushouse, H., Dowell, C. D., et al. 2006a, ApJ, 644, 198 [3](#)
- Yusef-Zadeh, F., Bushouse, H., Wardle, M., et al. 2009, ApJ, 706, 348 [3](#)
- Yusef-Zadeh, F., Roberts, D., Wardle, M., Heinke, C. O., & Bower, G. C. 2006b, ApJ, 650, 189 [3](#)
- Yusef-Zadeh, F., Wardle, M., Cotton, W. D., Heinke, C. O., & Roberts, D. A. 2007, ApJ, 668, L47 [3](#)
- Yusef-Zadeh, F., Wardle, M., Heinke, C., et al. 2008, ApJ, 682, 361 [3](#)

Acknowledgements

There are many persons in my life who have supported me in writing this thesis. They have done so either recently or they did it in the distant past, even before knowing what I was about to do after leaving school. All the encouragement I received enabled me to pursue my goals and resulted in that document you are now holding in your hands.

First of all, I would like to thank Prof. Dr. Andreas Eckart. He gave me the opportunity to work on a fascinating topic with fascinating data. His supervision ensured that I did not lose track and stimulated me as well.

Of course, I am very grateful to Julia Scharwächter, who introduced me to the exciting world of AGN and IFS. I really appreciate all her efforts to make my publications readable, to answer my (sometimes stupid) questions, and to discuss my ‘wild’ theories. Beyond working issues: I thank her for our nice excursions in Australia and for borrowing me the binoculars: Finally I saw the Milky Way with different eyes.

My gratitude goes also to Prof. Dr. Françoise Combes and Prof. Dr. Santiago García-Burillo for their support on the topic of gas kinematics and for proposal writing.

Macarena García-Marín and Mónica Valencia-S. are more than my ‘walking astronomy compendiums’. They are constant sources of solace, support and good mood.

My former office mate Gunther Witzel, who taught me to see some things just a bit more relaxed.

Definitively, I also want to thank Senol, Silvia, Nadeen, Banafsheh, Gerold, Yasir, Mónica, Maca and all the others of the aegroup. You all contribute to a unique working environment that made it easy to spend time in the office. I am sure, I will never ever find anything similar elsewhere. Even more, some of you became part of my private life and I am happy to call you my friends.

Joseph, who was the first idol I had, and who taught me the value of knowledge and education when I was still a small kid.

Sandra, for shielding me against the world's everyday nuisances.

I thank my lovely new parents, Tina and Giorgio, for hosting me in their little paradise where I replenished my energy. Grazie mille per le vacanze, i cibi buonissimi e per vostra figlia. Non posso desiderare di piu. Avete contribuito moltissimo e benissimo al mio tesi.

Of course Thorsten, always a source of inspiration and the best friend I can imagine.

Most important, I am grateful to my family and my beloved one, Mariangela, who have supported me during very hard times with their commitment, patience and love. I will never forget it.

Finally and utmost, I thank my mother. It is futile to try finding words for something I cannot express. I guess, she knew anyhow.

This work is carried out within the Collaborative Research Council SFB 956, sub-project [A2], funded by the Deutsche Forschungsgemeinschaft (DFG).

M. B. is grateful for the travel support granted by the Group of Eight (Go8) of Australia and the German Academic Exchange Service (DAAD) (Go8 Australia-Germany Joint Research Co-operation Scheme).

This research has made use of the NASA/IPAC Extragalactic Database (NED) which is operated by the Jet Propulsion Laboratory, California Institute of Technology, under contract with the National Aeronautics and Space Administration.

Funding for the SDSS and SDSS-II has been provided by the Alfred P. Sloan Foundation, the Participating Institutions, the National Science Foundation, the U.S. Department of Energy, the National Aeronautics and Space Administration, the Japanese Monbukagakusho, the Max Planck Society, and the Higher Education Funding Council for England. The SDSS Web Site is <http://www.sdss.org/>. The SDSS is managed by the Astrophysical Research Consortium for the Participating Institutions. The Participating Institutions are the American Museum of Natural History, Astrophysical Institute Potsdam, University of Basel, University of Cambridge, Case Western Reserve University, University of Chicago, Drexel University, Fermilab, the Institute for Advanced Study, the Japan Participation Group, Johns Hopkins University, the Joint Institute for Nuclear Astrophysics, the Kavli Institute for Particle Astrophysics and Cosmology, the Korean Scientist Group, the Chinese Academy of Sciences (LAMOST), Los Alamos National Laboratory, the Max-Planck-Institute for Astronomy (MPIA), the Max-Planck-Institute for Astrophysics (MPA), New Mexico State University, Ohio State University, University of Pittsburgh, University of Portsmouth, Princeton University, the United States Naval Observatory, and the University of Washington.

Ich versichere, daß ich die von mir vorgelegte Dissertation selbständig angefertigt, die benutzten Quellen und Hilfsmittel vollständig angegeben und die Stellen der Arbeit – einschließlich Tabellen, Karten und Abbildungen –, die anderen Werken im Wortlaut oder dem Sinn nach entnommen sind, in jedem Einzelfall als Entlehnung kenntlich gemacht habe; daß diese Dissertation noch keiner anderen Fakultät oder Universität zur Prüfung vorgelegen hat; daß sie – abgesehen von unten angegebenen Teilpublikationen – noch nicht veröffentlicht worden ist sowie, daß ich eine solche Veröffentlichung vor Abschluß des Promotionsverfahrens nicht vornehmen werde. Die Bestimmungen dieser Promotionsordnung sind mir bekannt. Die von mir vorgelegte Dissertation ist von Prof. Dr. Andreas Eckart betreut worden.

Köln, 26.03.2014

Teilpublikationen

- **Bremer, M.**; Scharwächter, J.; Eckart, A.; Valencia-S., M.; Zuther, J.; Combes, F.; Garcia-Burillo, S.; Fischer, S. (2013) "*What produces the extended LINER-type emission in the NUGA galaxy NGC 5850?*" A&A, 558, 34B

- **Bremer, M.**; Scharwächter, J.; Eckart, A.; Zuther, J.; Fischer, S.; Valencia-S., M. (2012) "*Optical Integral Field Spectroscopy of NGC 5850*" JPhCS, 372

- **Bremer, M.**; Witzel, G.; Eckart, A.; Zamaninasab, M.; Buchholz, R.-M.; Schödel, R.; Straubmeier, C.; García-Marín, M.; Duschl, W. (2011) "*The near-infrared spectral index of Sagittarius A* derived from Ks- and H-band flare statistics*" A&A, 532, A26

Lebenslauf

Ausbildung

Name: Marcus Bremer
Anschrift: Grosser Griechenmarkt 11-13
50676 Köln
Telefon: +49-0221 2936338
Email: mbremer@ph1.uni-koeln.de
Geburtsort: Köln
Geburtsdatum: 22 Juli 1975

Ausbildung

Seit Mai 2010 Promotionstudent
I Physikalisches Institut der Universitaet zu Köln
Köln, Deutschland
2009-2010 Diplomand in Physik
I Physikalisches Institut der Universitaet zu Köln
Köln, Deutschland
2002-2009 Studium der Physik
I Physikalisches Institut der Universitaet zu Köln
Köln, Deutschland
1996-1999 Studium der Informatik
Fachhochschule der Wirtschaft
Paderborn, Deutschland

Berufliche Laufbahn

2000-2002 Unternehmensberater
KPMG Consulting GmbH
Frankfurt a. M., Deutschland

Köln, 2014